Analyzing Perturbations of Sleep-Wake Dynamics Using Bifurcation Theory and Circle Maps

by

Christina Athanasouli

A dissertation submitted in partial fulfillment
of the requirements for the degree of
Doctor of Philosophy
(Applied and Interdisciplinary Mathematics)
in The University of Michigan
2022

Doctoral Committee:

Professor Victoria Booth, Co-Chair
Professor Daniel Forger, Co-Chair
Professor Cecilia Diniz Behn, Colorado School of Mines
Professor Michal Zockowski

Christina Athanasouli

chrath@umich.edu

ORCID iD: 0000-0002-0942-6767

To my parents, Sotiris and Reveka

ACKNOWLEDGEMENTS

I am grateful to my advisor, Victoria Booth, for all her support throughout my years in graduate school. I appreciate all the helpful guidance, the time that she invested in me, her patience and excitement that kept me motivated, and her constant encouragement to pursue activities that improved me as a mathematician and an instructor. I could not have asked for a better advisor. She has provided me with a valuable repository of great academic, scientific and life advice and memories.

I also want to express my gratitude to Cecilia Diniz Behn for her mentorship and encouragement. It has been a pleasure to work with her on the projects presented in this dissertation, learn from her feedback and insights, and be introduced to her amazing group of students at the Colorado School of Mines.

I greatly appreciate all the helpful conversations with Daniel Forger throughout the years. I enjoyed his class on the mathematics of wearables, his teaching style and his perspectives on research in sleep and circadian rhythms.

I would also like to thank Michal Zochowski for giving me the opportunity to join his lab meetings and interact with his students. I have really enjoyed our journal club and learned a lot about neural networks. I truly appreciate all the support this last year of my PhD.

A special thanks to Charlie Doering for being excited and curious about my research. I am grateful that I had the opportunity to meet him, ask him questions about dynamical systems, and experience his enthusiasm about Applied Mathematics.

I would also like to thank Sofia Piltz for collaborating with me, providing valuable

feedback, encouraging me and teaching me about piecewise-smooth dynamical systems.

Moreover, I would like to thank Shelby Stowe for being a great collaborator and all the helpful discussions.

Thank you all for making me feel confident about my work.

I am grateful to my boyfriend, Joe Kraisler, for his constant emotional support. I want to thank him for talking about math and teaching with me, giving me good advice, and reminding me that there is more to life than work.

I could not have done this without my family's support, especially at times when it was hard being away from home. Finally, I want to thank all the wonderful people I met in Ann Arbor and East Lansing. Thank you for all the great memories, Robert, Christiana, Mitul, David, Alex H., Nawaz, Christos, Giannis, Alex G., Michalis, Giorgos.

TABLE OF CONTENTS

LIST OF FIGURES

Figure

LIST OF TABLES

Table

LIST OF APPENDICES

Appendix

ABSTRACT

Sleep patterns and timing can be influenced by gradual developmental changes or more acute perturbations such as sleep deprivation. In this thesis, we employ physiologically-based mathematical models of neural sleep-wake regulatory networks to analyze 1) biological factors that influence the developmentally-mediated transition from polyphasic to monophasic sleep, and 2) recovery responses to sleep deprivation.

In the first project, we utilize a sleep-wake flip-flop (SWFF) model to analyze how developmentally-mediated transitions in sleep-wake dynamics are affected by homeostatic and circadian modulation. Specifically, we show that varying the rates at which the homeostatic sleep drive evolves leads to the transition from polyphasic to monophasic sleep in a period adding bifurcation structure of the average number of sleeps per day. We numerically construct circle maps that capture sleep onset phases, and find that saddle-node and border collision bifurcations in these maps result in the gain or loss of stable solutions. Moreover, we show that imposing a steeper circadian temporal profile reduces the variability in sleep patterns and promotes the persistence of specific sleep behaviors during the polyphasic to monophasic transition.

In the second project, we consider a physiologically-based model that produces wake, rapid eye movement (REM) and non-REM (NREM) sleep states to investigate how NREM-REM cycling influences the types of sleep patterns obtained under a similar homeostatic variation. We conduct a computationally-based analysis, including numerical construction of sleep onset circle maps, and find a disrupted, non-monotonic period adding bifurcation structure in the average number of sleeps per day. Our analysis shows that NREM-REM cycling, resulting in more complex sleep onset map

structures in this three-state model, allows for both higher order cycles and bistability to occur. The structure of the circle map reflects variation in the number of REM bouts per sleep, and saddle-node, border collision and period-doubling bifurcations causing the transition to different sleep patterns, whose characteristics can be highly variable due to the homeostatic dynamics, ultradian dynamics of NREM-REM cycling and their interactions.

In the third project, we focus on the transition from napping (biphasic) to non-napping (monophasic) sleep behavior observed in early childhood (between ages of 2 and 5 years). Using the SWFF model, we set values for the parameters governing the evolution of the homeostatic sleep drive to data estimated in preschool children. We then identify other model parameters to generate the timing of experimentally measured sleep patterns in 2 and 5 year old children. We show that the homeostatic parameters and the sensitivity of the model to the sleep homeostat are sufficient for the generation of the transition from napping to non-napping sleep behaviors. We consider different variations of these parameters across development that lead to distinct sleep transition behaviors that may account for interindividual differences. Finally, we investigate the effect of forced light schedules that promote napping or maintain wakefulness during daytime on the transition from biphasic to consolidated sleep.

In the last project, we use the three-state model to show that sleep onset circle maps can be employed to predict recovery from acute sleep deprivation. We compare map predictions with experimental data and numerical simulations of the model when behaviorally-gated light schedules are incorporated. The map predictions reproduce trends in the durations of recovery sleep observed in both experimental data and simulations of sleep deprivation using the full model, thus validating its use as a predictive method.

CHAPTER I

Introduction

Although the ultimate function of sleep has not yet been determined, numerous studies indicate the importance of sleep in maintaining good physical and mental health. For example, insufficient amount and poor quality of sleep can be linked to cardiovascular diseases [85], obesity and stress. Regarding more neurological benefits, sleep supports learning and memory consolidation, restoration of the brain from metabolic waste and synaptic plasticity [65].

Such sleep-dependent brain tasks are especially significant during the first stages of life, when toddlers and children develop many important skills. Interestingly, this is also the part of one's life that exhibits the largest variability in the types of sleep patterns observed. In particular, during development humans transition from irregular to more regular polyphasic (multiple per day) sleep patterns and subsequently, to monophasic (one per day) sleep patterns, with high interindividual variability. However, most physiological processes governing the regulation of human sleep stabilize within the first few months after birth and are conserved thereafter.

Motivated by this transition, we use mathematical modeling to investigate possible developmentally-mediated mechanisms that may produce the transition from polyphasic to monophasic sleep patterns. Our physiologically-based models are ordinary differential equation (ODE)-based systems representing the network of brain regions

promoting states of wake and sleep. Dynamics of model solutions resemble those of coupled oscillator systems, since sleep-wake patterns exhibit daily periodic rhythms. We draw on various mathematical techniques to analyze model behavior and reduce dynamics to one-dimensional circle maps. Transitions in sleep patterns are elicited as bifurcations of these maps.

Circle maps have long been employed to study various biological systems consisting of coupled oscillators in which one oscillator drives another [6, 67, 42]. In addition, there exists a vast literature on the analysis of functions of the circle to itself describing circle maps (e.g., [92, 70, 94, 30, 72]). As reduced models for coupled oscillator systems, these results provide a powerful framework for understanding the dynamics of relative frequencies of coupled oscillators, including identifying types of phase-locked or entrained solutions [82, 96, 13], bifurcations between these solutions [119, 147] and chaotic dynamics [69, 79, 168]. Circle maps can be explicitly formulated for some model systems, such as threshold systems [67, 119, 31, 42, 72] or integrate-and-fire models [6, 14].

However, using circle maps to understand solutions and their bifurcations in high-dimensional, differential equations-based, coupled oscillator models of biological processes is generally difficult since explicit computation of an underlying circle map is not straightforward. In this thesis, we conduct numerical computation of circle maps to investigate responses of solutions of sleep-wake regulatory network models to parameter variations or external inputs.

This dissertation is organized as follows: in the remaining parts of Chapter I we review principles of sleep-wake physiology and bifurcations of dynamical systems. In Chapter II we describe the sleep-wake models and mathematical methods utilized in our work. Chapters III and IV discuss analyses of the bifurcations generating transitions in sleep patterns in two sleep-wake network models, and Chapter V presents data-driven modeling of sleep behavior in early childhood. In Chapter VI, we employ circle maps

to predict responses to sleep deprivation. Finally, Chapter VII includes an overview of our results and avenues for future work.

1.1 Sleep-wake physiology

1.1.1 Vigilance states and measurement methods

Sleep is composed of two main stages, Rapid Eye Movement (REM) and non-REM (NREM) sleep. During the course of a sleep period, an alternation between REM and NREM sleep occurs [34]. One of the key methods for discerning the different vigilance states is the electroencephalogram (EEG) which provides measurements of electrical activity of the brain. EEG signals measured during wakefulness, REM and NREM sleep are distinct, with more asynchronous, high frequency and low amplitude signals occurring during wakefulness. In particular, activity in the alpha, beta and gamma frequency bands (8-14 Hz, 14-30 Hz, 30-100 Hz, respectively) are observed, with the higher frequencies taking place during high alertness periods. Healthy mature individuals enter a sleep episode through NREM sleep that is itself divided in three stages, namely N1, N2, N3 [34]. Once again, these states can be classified based on the frequency bands observed in EEG signals. During N1 individuals feel drowsy and their muscle movement starts decreasing. During N2 individuals transition to light sleep displaying minimal muscle and eye movement. In this stage, EEG activity is in the theta band (4-7 Hz) and may exhibit spindles or K-complexes. Finally, N3 is called slow wave sleep (SWS) and high amplitude, low frequency activity or "waves" in the theta band (0.5-4 Hz) are prominent. REM sleep is strongly associated with the occurrence of dreaming [7]. The electrical activity observed during the REM state is more similar to the irregular, low amplitude, high frequency patterns observed during wake periods [7]. Therefore, REM sleep is sometimes also called paradoxical sleep.

Other ways to discern sleep stages include the electrocardiogram (ECG), elec-

tromyogram (EMG) and electrooculogram (EOG) that output measurements of heart rate, muscle and eye movement, respectively. These tend to decrease as individuals transition to deep sleep, but eye movement can be high during REM sleep. The EEG, ECG, EMG and EOG (polysomnography) are the most accurate tools for capturing characteristics of sleep and wake, but can only be performed in labs and sleep clinics. However, actigraphy is an alternative method employed in many sleep research studies [22]. Participants wear watch-like devices that measure their movements which are, subsequently, translated into information regarding sleep-wake regulation. Since actigraphy is less accurate than polysomnography executed in labs, many participants may also keep sleep diaries to inform their sleep assessment. In more recent years, the need to understand and improve one's sleep habits has become more important in daily life. Therefore, the production of various types of commercial wearables and mobile applications that keep track of sleep schedules, assess individuals' sleep habits and possibly make predictions has dramatically increased [160, 111]. These wearable devices take into account heart rate and movement measurements (i.e. steps) that provide quantitative sleep data. Many of these systems depend on mathematical models to make predictions. Mathematical models can be conceptual or more physiologically-based and their construction requires a good understanding of the biological mechanisms of sleep-wake regulation.

1.1.2 Neurobiology

The different vigilance states are driven by neuronal populations in various regions of the brain (Figure 1.1). The brainstem and hypothalamus house key wake-promoting regions containing monoaminergic neurons. These include noradrenergic neurons of the locus coeruleus (LC), serotonergic neurons of the dorsal (DR) and median raphe nuclei, dopaminergic neurons of the ventral tegmental area (VTA), and histaminergic neurons of the tuberomammillary nucleus (TMN). Wake-promoting signals also arise from

cholinergic regions, including the pedunculopontine (PPT) and laterodorsal tegmental nuclei (LDT) and basal forebrain (BF) [141]. Neurons in these regions project to higher areas of the brain through ascending pathways to promote wakefulness during their high firing periods.

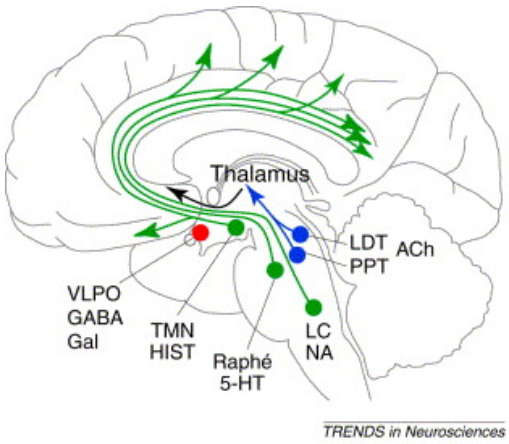

Figure 1.1: Regions of the brain involved in sleep-wake regulation. Reprinted from [139] with permission from Elsevier and Copyright Clearance Center.

Neurons in the ventrolateral (VLPO) and median preoptic nuclei (MnPO) express gamma-Aminobutyric acid (GABA) and inhibit the arousal-promoting areas mentioned above to contribute to the induction of NREM sleep. These regions are innervated by wake-promoting areas and expression of wake-associated neurotransmitters suppresses the activity of the VLPO neurons [141, 139]. The mechanisms regulating REM sleep are not fully understood yet. One of the early hypotheses suggests that REM is controlled by the reciprocal interaction between REM sleep-promoting, cholinergic neurons in the LDT/PPT and REM sleep-suppressing, monoaminergic neurons [81, 141]. More recently, glutamatergic neurons in the sublaterodorsal tegmental nucleus (SLD) of the pons have been shown to play an important role in promoting the transition to REM sleep. Additionally, neurons in the ventrolateral periaqueductal gray matter (vlPAG) and the adjacent lateral pontine tegmentum (LPT) are silent during REM sleep and active during NREM sleep and wake. The neurons in the SLD and vlPAG/LPT suppress the activity of one another. Hence, a mutually inhibitory circuit between

these groups of neurons is an alternative proposed mechanism for REM sleep regulation [103, 141].

1.1.3 Circadian rhythm

Transitions between sleep and wake states are driven by two main processes, the circadian ($\sim$ 24h) rhythm and the homeostatic sleep drive [26, 37, 51]. The role of the circadian rhythm, our internal biological clock, is to synchronize the functions of the body to external environmental cues, the primary one being the 24 h light/dark cycle. The process of synchronization of the autonomous oscillator with an external timing cue is called entrainment. In mammals, such as humans, circadian modulation of sleep-wake behavior, hormonal and body temperature fluctuations, and other physiological functions, is controlled by the suprachiasmatic nucleus of the hypothalamus (SCN). The SCN receives light input through the retina [116]. Studies suggest that the neural activity in the SCN is high during the light period, and the circadian clock promotes wake during the day and sleep during the night [109, 37] by indirectly projecting to the wake- and sleep-promoting regions of the brain.

Core body temperature and the hormone, melatonin, are two important markers of the endogenous circadian clock [19]. Melatonin is produced in the pineal gland during the night and can be suppressed by exposure to light. Core body temperature levels are lowest, whereas melatonin levels are highest, during the night sleep [141, 143]. For healthy individuals, the onset of melatonin occurs close to sunset and is known as dim-light melatonin onset, DLMO. Its offset occurs before wake time and after sunrise. Constant routine protocol studies suggest that the core body temperature temporal profile may be influenced by sleep and posture. In contrast, the melatonin temporal profile shows less variability under baseline and constant routine conditions. It is important to note that the amplitude of the melatonin secretion profile decreases with increased age. Melatonin measured in human saliva is closely correlated with

melatonin found in the blood and therefore, allows the evaluation of circadian timing via a short, noninvasive collection method [159].

1.1.4 Sleep homeostasis

The timing and duration of sleep is highly dependent on the history of prior awakening. The duration and intensity of sleep may be affected following sleep deprivation [27]. Hence, sleep is homeostatically regulated. During wakefulness our irresistible urge to fall asleep increases, and it decreases during sleep. The established marker of sleep homeostasis is slow wave activity (SWA) [61]. In particular, SWA corresponds to the EEG power in the delta band (0.5-4.5 Hz) during NREM sleep, and provides a quantitative measure of the amplitude and incidence of sleep slow waves [61]. SWA declines in the course of sleep, increases after a waking period, and is higher after sleep deprivation, suggesting that it reflects the accumulation of sleep pressure during wake and its dissipation during sleep. One of the proposed mechanisms for the increase in SWA is the build up of adenosine, a molecular substance that has been shown to be suppressed by caffeine [5].

1.1.5 Sleep patterns across development

Sleep patterns exhibit large variability across the lifespan with the number, duration, timing and distribution of NREM and REM episodes changing with development. Specifically, infants manifest polyphasic (multiple per day) sleep patterns. In newborns, sleep episodes, constituting about 70% of a day, are scattered across the 24 hours. Newborn infants enter sleep through REM. REM sleep predominates, with the NREM stages emerging over the first 2 to 6 months of life. The NREM-REM alternation lasts about 50-60 minutes. Circadian rhythms are also developed postnatally. In particular, the melatonin rhythm emerges after 9 weeks, while the core body temperature rhythm is prominent after 11 weeks [90]. Nighttime sleep is consolidated after about 6-9

months with naps still persisting across the day [165]. Most toddlers tend to have one nap after at an age of 15 months and that trend persists during the preschool years. The duration of REM sleep decreases, and SWS starts predominating. Many children start the transition towards monophasic sleep patterns at the age of 3, and by the age of 5 years the majority has dropped the afternoon nap.

The percentage of time spent in SWS is largest in early childhood, but starts decreasing during adolescence and across the lifespan. In adolescents, sleep need does not decrease, but sleep duration does [87]. Adolescents exhibit a delay in their circadian phase, that leads to them tending to fall asleep later and wake up later (at least on the weekends) [87]. Healthy young adults sleep about 8 hours a day, and NREM sleep and REM sleep alternate throughout the night every 90 minutes. REM sleep is 20% to 25% of total sleep and occurs in about 4 to 6 bouts. The duration of REM bouts becomes longer as the sleep episode progresses [34]. Aging is associated with a phase advance that leads to older adults experiencing sleepiness earlier and waking up earlier. Additionally, sleep fragmentation is more common in older adults, the total sleep time is decreased, and a decline in SWS and REM sleep is observed [112].

1.2 Mathematical models of sleep-wake regulation

In the 1980s, Borbèly et al. proposed a conceptual model, the Two Process Model, involving the interaction of the homeostatic sleep drive (Process S) and the circadian drive (Process C), to capture properties regarding sleep-wake regulation [26]. As mentioned earlier, SWA represents the principal marker of Process S during sleep, whereas theta activity in waking is a marker of its increasing portion. Core body temperature and melatonin rhythms are the established markers for Process C. According to the Two Process Model, Process S oscillates between two threshold curves dictated by the circadian process (Figure 1.2). As Process S increases, and

therefore, sleep debt builds up, it approaches the upper circadian threshold. Once it intersects the upper threshold curve, sleep is initiated and Process S starts dissipating exponentially. A wake onset occurs when Process S intersects the lower threshold curve at the correct timing. The model predictions are in agreement with data regarding multiple studies, such as sleep deprivation experiments and sleep duration under shiftwork [28].

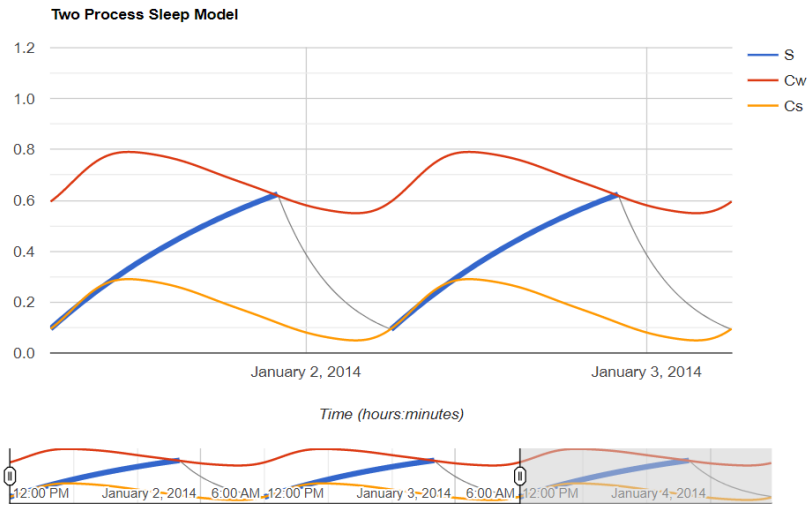

Figure 1.2: An illustration of the Two Process Model using the simulator found in http://twoprocessmodel.math.lsa.umich.edu/. As Process S (blue curve) increases, and therefore, sleep debt builds up, it approaches the upper circadian threshold (red curve denoted as C_w). Once it intersects the upper threshold curve, sleep is initiated and Process S starts dissipating exponentially. A wake onset occurs when Process S intersects the lower threshold curve (yellow curve denoted as C_s).

The deeper understanding of the anatomy and physiology underlying sleep–wake control has motivated the construction of network models with more physiological basis. These models utilize various formalisms inspired by mathematical neuroscience, since they include the interactions of neuronal populations that promote wake and sleep states, as well as the effect of the circadian rhythm and homeostatic sleep drive on the transitions between states [152, 17, 134, 100, 125, 71, 53]. In this thesis, we employ variations of a previously-developed model of sleep-wake regulation [71]. In the model, the activity of each postsynaptic cell group is captured by its associated

mean firing rate as determined by projections from presynaptic populations. The model network consists of wake-, NREM- and REM-promoting populations as well as an SCN population to incorporate the circadian rhythm. Mutual inhibition between the wake- and NREM-promoting neuronal populations represents the idea of a flip-flop switch structure that regulates sleep-wake transitions [139]. Accordingly, in the model, when the activity level of the wake- (NREM-) promoting population is high, it inhibits the NREM- (wake-) promoting neurons and maintains its state. Transitions between these states are fast and driven by the circadian and homeostatic processes. The model representation for REM sleep regulation is based on the reciprocal interaction hypothesis, which is reflected in an inhibitory projection from the wake population to the REM sleep population and an excitatory projection from the REM sleep to the wake population. A more detailed description of the model and its possible variations is given in Chapter II.

1.3 Mathematical tools and techniques

The mathematical models for sleep-wake regulation that we utilize are piecewise-smooth dynamical systems. In this section, we review definitions, tools and techniques from the theory of smooth and nonsmooth dynamical systems and maps that we employ in the chapters of this thesis mainly drawn from [45].

1.3.1 Piecewise-smooth systems

1.3.1.1 Flows

Definition 1.1. A *piecewise-smooth flow* is given by a finite set of ODEs $\dot{x} = F_i(x, \mu)$, for $\mu \in \mathbb{R}^m$, $x \in S_i$, where $\bigcup_i S_i = D \subset \mathbb{R}^n$ and each S_i has a non-empty interior. The intersection $\Sigma_{ij} := \overline{S_i} \cap \overline{S_j}$ is either an $\mathbb{R}^{n-1}$-dimensional manifold included in the boundaries ∂S_j and ∂S_i, or is the empty set. Each vector field F_i is smooth in both

the state x and the parameter μ, and defines a smooth flow $\Phi_i(x,t)$ within any open set $U \supset S_i$. In particular, each flow Φ_i is well defined on both sides of the boundary ∂S_j.

The intersection, Σ_{ij}, is called a *discontinuity set*, *discontinuity boundary*, or *switching manifold*. A schematic of a piecewise-smooth flow is shown in Figure 1.3.

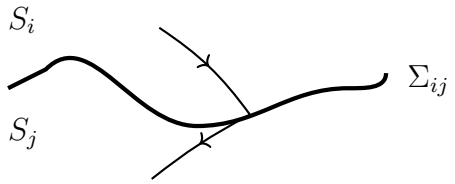

Figure 1.3: Schematic of trajectories of a piecewise-smooth flow.

Definition 1.2. The *degree of smoothness* at a point x_0 in a switching set Σ_{ij} of a piecewise-smooth ODE is the highest order r such that the Taylor series expansions of $\Phi_i(x_0,t)$ and $\Phi_j(x_0,t)$ with respect to t, evaluated at $t=0$, agree up to terms of $O(t^{r-1})$. That is, the first non-zero partial derivative with respect to t of the difference $[\Phi_i(x_0,t) - \Phi_j(x_0,t)]\Big|_{t=0}$ is of order r.

The mathematical models we encounter fall under a specific category of nonsmooth dynamical systems, namely Filippov systems. Filippov systems exhibit a jump in the derivative on the switching manifold. Formally, let

$$\dot{x} = \begin{cases} F_1(x), & x \in \Sigma^+ \\ F_2(x), & x \in \Sigma^- \end{cases} \tag{1.1}$$

be a piecewise-smooth system for $x \in D = \bigcup_{j\in\{+,-\}} \Sigma^j$ with one switching boundary Σ defined by the equation $H(x) = 0$. The vector field F_1 is defined for points $x \in \Sigma^+ := \{x \mid H(x) > 0\}$ and generates a flow $\Phi_1(x,t)$. Similarly, the vector field F_2 is defined for points $x \in \Sigma^- := \{x \mid H(x) < 0\}$ and generates a flow $\Phi_2(x,t)$.

We have that $\left.\dfrac{\partial \Phi_i(x,t)}{\partial t}\right|_{t=0} = F_i(x)$. The ODE system is a *Filippov system*, if $F_1(x) \neq F_2(x)$ for a point $x_0 \in \Sigma$, and thus, the first derivatives of the corresponding flows differ at x_0.

Flows generated by system 1.1 may slide along the switching manifold $H(x)$, and sliding dynamics should be taken into account when constructing solutions.

Definition 1.3. The *sliding region* of the discontinuity set of a system of the form 1.1 is given by that portion of the boundary of $H(x)$ for which $(H_x F_1) \cdot (H_x F_2) < 0$. That is, $H_x F_1$ (the component of F_1 normal to H) has the opposite sign to $H_x F_2$. Thus, the boundary is simultaneously attracting (or repelling) from both sides.

One of the methods used to define the flow along the switching boundary Σ, is *Filippov's convex method* that represents the sliding vector field as a convex combination of the two vector fields $F_{12} = (1-\alpha)F_1 + \alpha F_2$ with $0 \leq \alpha \leq 1$, where $\alpha(x) = \dfrac{H_x F_1}{H_x(F_1 - F_2)}$. The sliding vector field represents the tangent vector of the flow, and $\alpha(x)$ is chosen so that the sliding vector field is orthogonal to the normal of the boundary Σ, H_x, and therefore, tangent to the switching boundary itself.

1.3.1.2 Maps

Definition 1.4. A *piecewise-smooth map* is described by a finite set of smooth maps $x \mapsto F_i(x,\mu)$, for $\mu \in \mathbb{R}^m$, $x \in S_i$, where $\bigcup_i S_i = D \subset \mathbb{R}^n$ and each S_i has a non-empty interior. The intersection Σ_{ij} between the closure (set plus its boundary) of the sets S_i and S_j (that is, $\Sigma_{ij} := \overline{S_i} \cap \overline{S_j}$) is either an $\mathbb{R}^{n-1}$-dimensional manifold included in the boundaries ∂S_j and ∂S_i, or is the empty set. Each function F_i is smooth in both the state x and the parameter μ for any open subset U of S_i.

As before, the intersection, Σ_{ij}, is called a *discontinuity boundary* or *border*. A schematic of a piecewise-smooth map is shown in Figure 1.4.

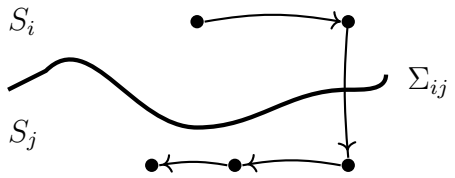

Figure 1.4: Schematic of trajectories of a piecewise-smooth map.

Definition 1.5. The *order of singularity* of a point $x_0 \in \Sigma_{ij}$ of a continuous piecewise-smooth map is the order of the first non-zero term in the formal power-series expansion of $F_1(x) - F_2(x)$ about $x = x_0$.

1.3.2 Poincaré and circle maps

Poincaré maps

In dynamical systems that generate periodic or quasi-periodic solutions, a useful tool to capture the evolution of the dynamics and reducing the dimensionality of the system is to define a *Poincaré map*.

Definition 1.6. Let $\dot{x} = f(x)$, with $x \in \mathbb{R}^n$, be a smooth dynamical system with phase space M that generates a flow $\Phi(x, t)$. In addition, let S be a $n-1$ dimensional section of the vector field, called a *Poincaré section*, such that the flow crosses it transversally. Assume that there exists $U \subset S$, such that the flow from any point in U eventually returns to a point in S. Then $\Pi : U \to S$ is called a *Poincaré map* and associates points in U with their points of first return on S. More specifically, for $x \in U$, $\Pi(x) = \Phi(x, \tau(x))$, where $\tau(x)$ is the minimal positive time such that $\Phi(x, t) \in S$.

A fixed point of the map corresponds to a closed orbit of the ODE system, and the stability of the orbit can be determined by analyzing the stability of the fixed point of the map. Poincaré maps can also be defined for piecewise-smooth systems.

Circle maps

The sleep-wake regulation models we consider have dynamics that are similar to a system of coupled oscillators. Circle maps, maps whose domain D is the unit circle $\mathbb{S}^1$, are employed in the study of coupled oscillators to analyze how the timing of one oscillator compares to the timing of the other. In systems of two coupled oscillators, timing between the oscillators can exhibit phase-locking, and therefore, the frequency ratio between the two oscillators is a fixed rational number. That ratio corresponds to the *rotation number*.

More formally, let $g : \mathbb{S}^1 \to \mathbb{S}^1$ be a circle map of degree 1, and $G : \mathbb{R} \to \mathbb{R}$ be its corresponding lift. That is $G(x+1) = G(x) + 1$ and there exists a homeomorphism $\pi : \mathbb{R} \to \mathbb{S}^1$ such that $\pi \circ G = g \circ \pi$. Then, the rotation number, ρ, associated to the circle map is defined as $\rho(x, G) = \lim_{n\to\infty} \dfrac{G^n(x) - x}{n}$.

For monotonic and continuous circle maps or homeomorphisms of the circle the rotation number is unique and independent of the point x [135]. Uniqueness of the rotation number has been proved for monotonic piecewise-smooth maps under certain conditions [75].

1.3.3 Bifurcations

In this section, we review bifurcations of smooth and nonsmooth maps that will be of interest in Chapters III-V. The main theorems are drawn from [77] (smooth maps) and [45, 11] (nonsmooth maps).

A bifurcation occurs when under smooth variation of parameters, there is a qualitative change in the behavior of the system. An example is a change in the stability of fixed points of the system.

Let $x \mapsto f(x, \mu)$ with $x \in \mathbb{R}^n$ be a map that depends smoothly on the parameter μ. Suppose that at $\mu = 0$ the system has a fixed point, $x_0 = 0$. To study changes in the stability of a fixed point, we can linearize the system about the fixed point and compute

eigenvalues of the Jacobian matrix, $\mathbf{J}\left(\mathbf{J}_{ij} = \dfrac{\partial f_i}{\partial x_j}\right)$. A bifurcation will occur when for some eigenvalue, λ_i, of the Jacobian evaluated at the fixed point and appropriate parameter value, $|\lambda_i| = 1$. We are interested in bifurcations of one-dimensional maps ($n = 1$). In one dimension, computing the eigenvalue of the linearized system about the fixed point is equivalent to determining the slope of the (smooth) map curve at that point. Therefore, a bifurcation occurs when the magnitude of the slope of the map at the fixed point becomes equal to 1.

Below we provide criteria for the occurrence of a saddle-node and a period-doubling bifurcation. Moreover, we illustrate these bifurcations using the logistic map, i.e $x_{n+1} = \mu x_n(1 - x_n)$, $\mu \in \mathbb{R}$ (Figure 1.5).

1.3.3.1 Saddle-node bifurcation

Intuitively, a *saddle-node* bifurcation occurs when a stable and an unstable fixed point of the map collide under parameter variation, forming a single fixed point. Further change in the parameter value leads to the disappearance of that fixed point. This bifurcation scenario is illustrated for the logistic map in Figure 1.5A.

Theorem 1.7. Suppose that $x \mapsto f(x, \mu)$, for $x, \mu \in \mathbb{R}$ is a map such that $f_x(0, 0) = 1$ (this is the bifurcation condition). Then, if the following conditions hold,

1. $\dfrac{1}{2} f_{xx}(0, 0) \neq 0$
2. $f_\mu(0, 0) \neq 0$

the map is topologically conjugate to the one-parameter family $y \mapsto \sigma + y + \beta y^2$ (with respect to the parameter σ) at the origin, where $\sigma = \pm 1$ (determined by the sign of the quantity in the first condition). This family of maps is called the normal form of a saddle-node bifurcation. For $\sigma\beta > 0$, there are no fixed points. For $\sigma\beta < 0$, there are two fixed points, and at $\beta = 0$, there is a fixed point at $y_0 = 0$ with eigenvalue 1.

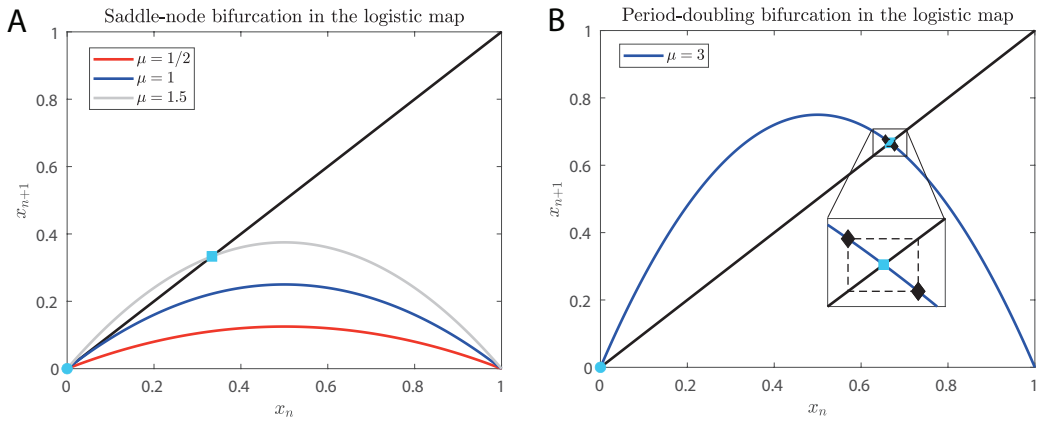

Figure 1.5: Saddle-node and period-doubling bifurcations in the logistic map. A. Saddle-node bifurcation in the logistic map. At $\mu = 0$ the map (red curve) has one stable fixed point at $x = 0$ (light blue circle). At $\mu = 1$ the slope of the map (blue curve) at $x = 0$ is equal to 1 and a saddle-node bifurcation occurs. At $\mu = 1.5$ the map (gray curve) has two fixed points. The fixed point $x = 0$ is now unstable, and a new stable fixed point exists at $x = 1/3$ (light blue square). B. Period-doubling bifurcation in the logistic map for $\mu = 3$. The map has two unstable fixed points at $x = 0$ (light blue circle) and $x = 2/3$ (light blue square). The slope of the map at $x = 2/3$ is -1. The stable solution (shown in the inset) is a period-2 cycle oscillating around $x = 2/3$ indicated by black diamonds.

1.3.3.2 Period-doubling bifurcation

A *period-doubling* bifurcation occurs when under parameter variation the eigenvalue of a fixed point of the map becomes -1 and leads to the emergence of a period-2 orbit or cycle. This bifurcation scenario is illustrated for the logistic map in Figure 1.5B.

Theorem 1.8. Suppose that $x \mapsto f(x, \mu)$, for $x, \mu \in \mathbb{R}$ is a map such that $f(x_0, \mu_0) = x_0$ (fixed point at x_0) and $f_x(x_0, \mu_0) = -1$ (this is the bifurcation condition). Then, if the following conditions hold,

1. $\left(\dfrac{\partial f}{\partial \mu}\dfrac{\partial^2 f}{\partial x^2} + 2\dfrac{\partial^2 f}{\partial x \partial \mu}\right) = \dfrac{\partial f}{\partial \mu}\dfrac{\partial^2 f}{\partial x^2} - \left(\dfrac{\partial f}{\partial x} - 1\right)\dfrac{\partial^2 f}{\partial x \partial \mu} \neq 0$ at (x_0, μ_0)

2. $a = \dfrac{1}{2}\left(\dfrac{\partial^2 f}{\partial x^2}\right)^2 + \dfrac{1}{3}\dfrac{\partial^3 f}{\partial x^3} \neq 0$ at (x_0, μ_0)

Then there is a smooth curve of fixed points, passing through (x_0, μ_0), the stability of which changes at (x_0, μ_0). There is also a smooth curve γ passing through (x_0, μ_0) so

that $\gamma - \{(x_0, \mu_0)\}$ is a union of hyperbolic period 2 orbits. The curve γ has quadratic tangency with the line $\mathbb{R} \times \{\mu_0\}$ at (x_0, μ_0). If a (in condition 2) is positive, the orbits are stable, while if a is negative they are unstable.

1.3.3.3 Border collision bifurcation

In piecewise-smooth maps, qualitative properties of fixed points may change due to either smooth or border-induced bifurcations, called *border collisions*.

We consider the case of a one-dimensional piecewise-smooth map with a single border Σ that can be described by the equation $H(x) = 0$. Let

$$x \mapsto \begin{cases} F_1(x, \mu), & x \in \Sigma^+ \\ F_2(x, \mu), & x \in \Sigma^- \end{cases} \tag{1.2}$$

be a piecewise-smooth system for $x \in D = \bigcup_{j \in \{+,-\}} \Sigma^j$, where $\Sigma^+ := \{x \mid H(x) > 0\}$ and $\Sigma^- := \{x \mid H(x) < 0\}$.

Definition 1.9. We say that a point x_0 is an *admissible (actual) fixed point* of the map 1.2, if for $i = 1$ or $i = 2$, $x_0 = F_i(x_0, \mu)$ and $x_0 \in S_j$ with $j = i$. We say instead that $x = \tilde{x}$ is a *virtual fixed point* of the map 1.2, if $\tilde{x} = F_i(\tilde{x}, \mu)$ and $\tilde{x} \in S_j$ with $i \neq j$.

Definition 1.10. Let $F_1(x)$ have a fixed point $x_1^* \in \Sigma^+$ for $\mu \in (\mu^* - \epsilon, \mu^*)$, for some $\epsilon > 0$, i.e. x_1^* is an actual fixed point of the map 1.2. Suppose that x_1^* is on the boundary Σ at $\mu = \mu^*$, and $x_1^*(\mu) \in S_2$ for $\mu \in (\mu^*, \mu^* + \epsilon)$, i.e., x_1^* becomes a virtual fixed point of the map 1.2. Then, at $\mu = \mu^*$, the fixed point x_1^* undergoes a border collision. We say that a border collision bifurcation occurs if a border collision leads to a qualitative change of the dynamics.

An example of border collision bifurcations is given in the following section (Figure 1.6), in which we describe bifurcation scenarios in a piecewise-linear map with a single

boundary defined by $H(x) = x$.

1.3.3.4 Period-adding bifurcation

To more easily describe and understand the period-adding bifurcation, we consider a one-dimensional discontinuous map described by linear equations. The map is given by

$$x \mapsto \begin{cases} \nu_1 x + \mu, & x \leq 0 \\ \nu_2 x + (\mu + \ell), & x > 0\,. \end{cases} \tag{1.3}$$

We describe the case of $\ell = -1$, and $0 < \nu_1, \nu_2 < 1$ that corresponds to the *period-adding bifurcation* scenario. Figures 1.6 and 1.7 illustrate this scenario for $\nu_1 = 1/2$ and $\nu_2 = 1/3$.

Here, the fixed points from each piece of the map are $x_1^* = \dfrac{\mu}{1-\nu_1}$ and $x_2^* = \dfrac{\mu - 1}{1-\nu_2}$. If $\mu < 0$, then x_1^* is the only admissible stable fixed point, while when $\mu > 1$, x_2^* is the only admissible stable fixed point. The fixed points, x_1^* and x_2^*, are lost through a border collision bifurcation at $\mu = 0$ and $\mu = 1$, respectively (Figure 1.6). For $\mu \in (0, 1)$, there exist periodic orbits, but no fixed points. In a period-adding bifurcation, the sequence of periodic orbits that exist as μ varies in $(0, 1)$ has a specific structure.

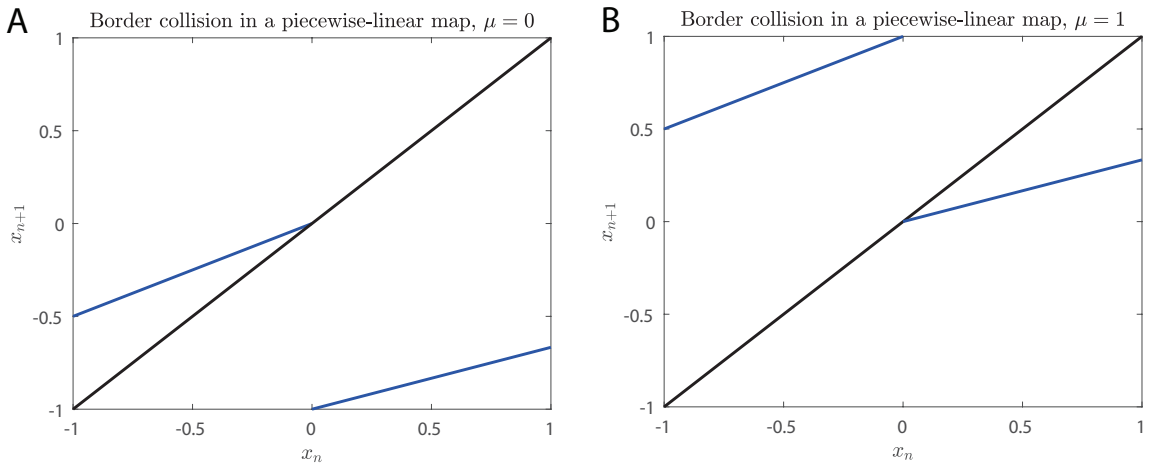

Figure 1.6: Border collision bifurcations in the piecewise-linear map for $\nu_1 = 1/2$, $\nu_2 = 1/3$. A. At $\mu = 0$ the left branch of the piecewise-linear map intersects the diagonal $x_{n+1} = x_n$ leading to the loss of the associated fixed point. B. At $\mu = 1$ the right branch of the piecewise-linear map intersects the diagonal $x_{n+1} = x_n$ leading to the loss of the associated fixed point.

Let $\mathscr{O}$ be an orbit of the map, namely a sequence of points $x_1 x_2 \dots x_k$ such that $x_{j+1} = f(x_j)$, for $1 \leq j \leq k-1$, and $x_1 = f(x_k)$. Then, for x_j in the orbit $\mathscr{O}$, we assign the symbol $\mathcal{L}$, if $x_j \in \Sigma^- = \{x \leq 0\}$, and the symbol $\mathcal{R}$ if $x_j \in \Sigma^+ = \{x > 0\}$. If the following conditions hold,

$$0 < \frac{\ell}{\mu} + \frac{1 - \nu_1^k}{\nu_1^{k-1} - \nu_1^k} \tag{1.4}$$

$$\nu_2 < -\left(\frac{\ell}{\mu} + \frac{1 - \nu_1^{k-1}}{\nu_1^{k-2} - \nu_1^{k-1}}\right) \tag{1.5}$$

an orbit of the form $\mathcal{L}^{k-1}\mathcal{R}$ exists. Namely, the orbit visits Σ^- $k-1$ times, and Σ^+ once during its periodic cycle. The orbit is stable if $-1 < \nu_2 \nu_1^{k-1} < 1$, which always holds since $0 < \nu_1, \nu_2 < 1$.

To obtain the conditions above, we note that if $x_1 x_2 \dots x_k$ is the orbit of the form

$\mathcal{L}^{k-1}\mathcal{R}$, with $x_1 \in \Sigma^+$ and $x_j \in \Sigma^-$ for $j = 2, \ldots, k$, we have:

$$x_2 = \nu_2 x_1 + (\mu + \ell) \tag{1.6}$$

$$x_j = \nu_1 x_{j-1} + \mu\,, j = 3, \ldots, k \tag{1.7}$$

$$x_1 = \nu_1 x_k + \mu \ \text{(by periodicity)} \tag{1.8}$$

By iterating forward we get

$$x_k = \nu_1^{k-2} x_2 + (\nu_1^{k-3} + \cdots + \nu_1 + 1)\mu. \tag{1.9}$$

Then substituting equations 1.6 and 1.8 we obtain an equation involving x_1

$$\begin{aligned}
\frac{1}{\nu_1}(x_1 - \mu) &= \nu_1^{k-2}[\nu_2 x_1 + (\mu + \ell)] + (\nu_1^{k-3} + \cdots + \nu_1 + 1)\mu \\
x_1 - \nu_1^{k-1}\nu_2 x_1 &= \nu_1^{k-1}\ell + \nu_1^{k-1}\mu + \nu_1^{k-2}\mu + \cdots + \mu \\
(1 - \nu_1^{k-1}\nu_2)x_1 &= \mu\left(\nu_1^{k-1}\frac{\ell}{\mu} + \frac{1 - \nu_1^k}{1 - \nu_1}\right) \\
(1 - \nu_1^{k-1}\nu_2)x_1 &= \mu\nu_1^{k-1}\left(\frac{\ell}{\mu} + \frac{1 - \nu_1^k}{\nu_1^{k-1} - \nu_1^k}\right)
\end{aligned}$$

Since $\mu > 0$ and $0 < \nu_1, \nu_2 < 1$ and $x_1 > 0$, we obtain condition 1.4.

Next, we substitute equations 1.6 and 1.8 we obtain an equation involving x_k

$$\begin{aligned}
x_k &= [\nu_2(\nu_1 x_k + \mu) + (\mu + \ell)]\nu_1^{k-2} + (\nu_1^{k-3} + \cdots + \nu_1 + 1)\mu \\
(1 - \nu_2\nu_1^{k-1})x_k &= \nu_2\nu_1^{k-2}\mu + \nu_1^{k-2}\ell + (\nu_1^{k-2} + \cdots + \nu_1 + 1)\mu \\
(1 - \nu_2\nu_1^{k-1})x_k &= \mu\left(\nu_2\nu_1^{k-2} + \nu_1^{k-2}\frac{\ell}{\mu} + \frac{1 - \nu_1^{k-1}}{1 - \nu_1}\right) \\
(1 - \nu_2\nu_1^{k-1})x_k &= \mu\nu_1^{k-2}\left(\nu_2 + \frac{\ell}{\mu} + \frac{1 - \nu_1^{k-1}}{\nu_1^{k-2} - \nu_1^{k-1}}\right)
\end{aligned}$$

Since $\mu > 0$ and $0 < \nu_1, \nu_2 < 1$ and $x_k < 0$, we obtain condition 1.5.

In the period-adding bifurcation, for μ close to 0, there are highly periodic orbits

of the form $\mathcal{L}^{k-1}\mathcal{R}$. As $\mu \to 0^+$ and $k \to \infty$ (see condition 1.4), a homoclinic orbit is observed, which connects periodic points on Σ^- with a fixed point on the boundary (i.e. $x = 0$).

Similar results can be obtained for orbits of the form $\mathcal{L}\mathcal{R}^{k-1}$. As $\mu \to 1^-$ and $k \to \infty$, another homoclinic orbit is observed, which connects periodic points on Σ^+ with a fixed point on the boundary (i.e. $x = 0$).

Interestingly, between orbits of period k and $k+1$ of the form $\mathcal{L}^{k-1}\mathcal{R}$ and $\mathcal{L}^k\mathcal{R}$, respectively, $\left(\text{that is for } \dfrac{1}{\nu_2 + \frac{1-\nu_1^k}{\nu_1^{k-1}-\nu_1^k}} < \mu < \dfrac{1}{\frac{1-\nu_1^k}{\nu_1^{k-1}-\nu_1^k}}\right)$ we find orbits constructed by concatenating their neighboring patterns. For example, a possible pattern of period $2k+1$ is $\mathcal{L}^{k-1}\mathcal{R}\mathcal{L}^k\mathcal{R}$ (see Figure 1.7). More generally, orbits of the form $\{\mathcal{L}^{k-1}\mathcal{R}\}^m\{\mathcal{L}^k\mathcal{R}\}^n$ are obtained.

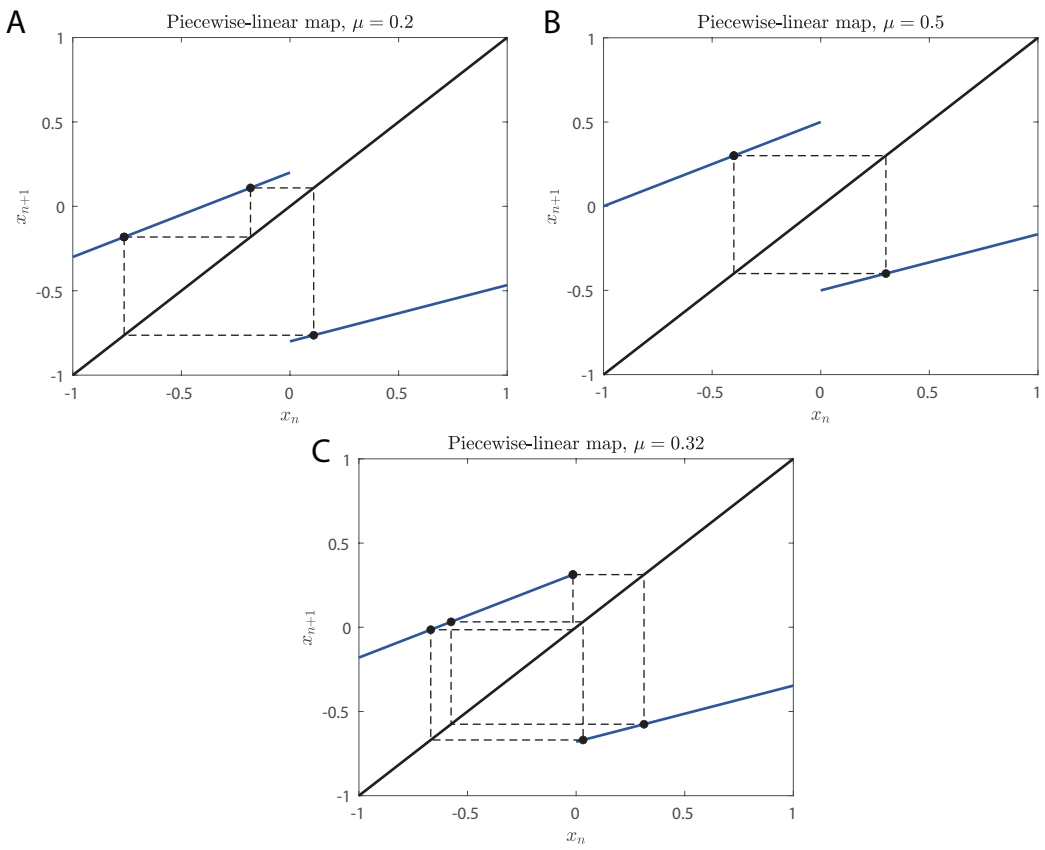

Figure 1.7: Higher order periodic solutions in the piecewise-linear map for $\nu_1 = 1/2$, $\nu_2 = 1/3$ and various values of μ. A: At $\mu = 0.2$ the orbit alternates between three values, two on the left branch and one on the right branch. The corresponding symbol of the orbit is $\mathcal{L}^2\mathcal{R}$. B: At $\mu = 0.5$ the orbit alternates between two values, one on the left branch and one on the right branch. The corresponding symbol of the orbit is $\mathcal{L}\mathcal{R}$. C. At $\mu = 0.32$ the orbit is a concatenation of the orbits at $\mu = 0.2$ and $\mu = 0.5$. Therefore, its corresponding symbol is $\mathcal{L}^2\mathcal{R}\mathcal{L}\mathcal{R}$.

An alternative way of describing the sequence of stable orbits obtained in a period-adding bifurcation is by the rotation number ρ defined as the number of symbols $\mathcal{R}$ over the total period of the orbit. For example, the orbit $\mathcal{L}^{k-1}\mathcal{R}$ has $\rho = 1/k$, while the orbit $\mathcal{L}^k\mathcal{R}$ has $\rho = 1/(k+1)$. Therefore, the concatenated orbit $\mathcal{L}^{k-1}\mathcal{R}\mathcal{L}^k\mathcal{R}$ has $\rho = 2/(2k+1)$. The orbits obtained as μ varies have rotation numbers that are elements of the *Farey sequence* and obey the Farey addition. According to the Farey addition, if $\rho_1 = r_1/k_1$, $\rho_2 = r_2/k_2$ correspond to the rotation numbers of two orbits, then an intermediate orbit obtained by concatenation has rotation number

$\rho = (r_1 + r_2)/(k_1 + k_2)$. In the example shown in Figure 1.7 ($\nu_1 = 1/2$, $\nu_2 = 1/3$), at $\mu = 0.2$, 0.32 and 0.5, the rotation numbers of the orbits are 1/3, 2/5, and 1/2, respectively. Note that 2/5 = (1+1)/(3+2). As μ increases, the rotation number ρ increases monotonically from 0 to 1 and is rational almost everywhere. The resulting graph of ρ as a function of μ is a Cantor function or a Devil's staircase.

CHAPTER II

Mathematical Models and Methods

In this chapter, we introduce the physiologically-based mathematical models [71] employed in this dissertation. The models incorporate interactions between neuronal populations that promote sleep and wake states, as well as the effects of the circadian and homeostatic sleep drives on the populations. We implement models that generate either two vigilance states (wake and sleep) or three vigilance states (wake, NREM, REM sleep). First, we introduce the two-state model, called the sleep-wake flip-flop (SWFF) model and analyze its dynamics using the techniques that were formally introduced in Chapter I. Then, we introduce the three-state model and perform a similar analysis.

2.1 Sleep-Wake Flip-Flop (SWFF) model

2.1.1 Model equations

The sleep-wake flip-flop (SWFF) model includes two neuronal populations that govern the transitions between the states of wake and sleep: a wake-promoting (W) and a sleep-promoting (S) population are coupled by mutual inhibition, and their interaction is modulated by homeostatic sleep and circadian drives. Representative wake-promoting monoaminergic populations include the locus coeruleus (LC) and the

dorsal raphe (DR); NREM sleep-promoting populations include GABAergic, sleep-active neurons of the ventrolateral preoptic nucleus (VLPO). In our SWFF model, the circadian input is mediated by a third neuronal population representing the suprachiasmatic nucleus (SCN), a group of cells in the hypothalamus that acts as the circadian pacemaker and displays a 24-hour variation in neural firing. For humans under typical conditions, the circadian rhythm and the sleep-wake cycle are entrained with lower SCN firing rates during sleep in the night and higher SCN firing rates during wake in daytime.

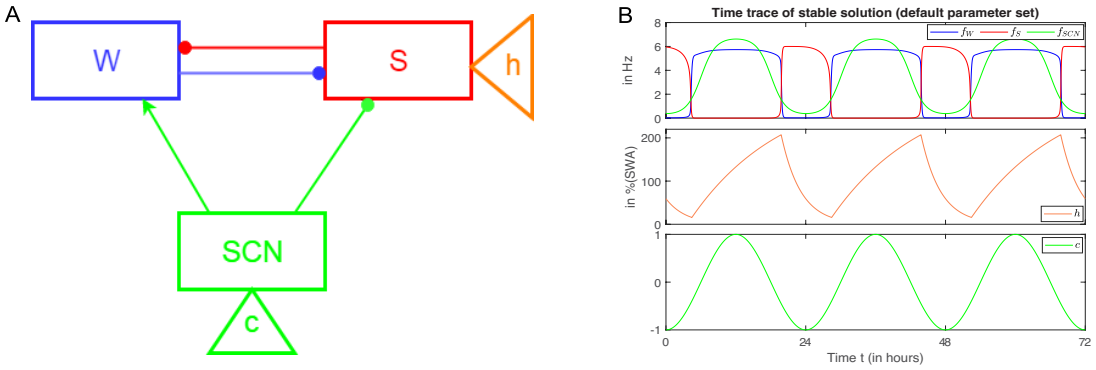

Figure 2.1: A SWFF model for sleep-wake regulation. A: Schematic of the model network summarizing interactions among the wake-promoting (W), sleep-promoting (S) and suprachiasmatic nucleus (SCN) neuronal populations with circles denoting inhibitory and arrows denoting excitatory synaptic connections. The homeostatic sleep drive (h) modulates activity of the sleep-promoting population and the circadian drive (c) modulates activity of both the sleep- and wake-promoting populations through SCN. B: Time traces of the stable solution of the model for the default parameter set that resembles stereotypical adult human sleep. The firing rates for wake- (f_W, blue), sleep- (f_S, red) promoting and SCN (f_{SCN}, green) populations are shown in the top panel. The middle and bottom panels include the profiles of the homeostatic sleep drive (h) and the circadian drive (c), respectively.

We use a firing rate formalism to model the neuronal population activity. Instead of tracking the spiking of single neurons, standard firing rate models describe the averaged behavior of spike rates of neuronal populations (f_W, f_S, f_{SCN}) [163, 41]. In particular, the mean postsynaptic firing rates are driven by the weighted mean firing rates of the presynaptic populations.

Neuronal populations

The equations for the neuronal populations are as follows:

$$\frac{df_W}{dt} = \frac{(W_\infty(g_{scnw}f_{SCN} - g_{sw}f_S) - f_W)}{\tau_W}\,, \tag{2.1}$$

$$\frac{df_S}{dt} = \frac{(S_\infty(-g_{ws}f_W - g_{scns}f_{SCN}) - f_S)}{\tau_S}\,, \tag{2.2}$$

$$\frac{df_{SCN}}{dt} = \frac{(SCN_\infty(c(t)) - f_{SCN})}{\tau_{SCN}}\,. \tag{2.3}$$

The postsynaptic firing rates, $f_X(t)$ (in Hz), saturate to their steady state firing rate response functions $X_\infty(\cdot)$ with time constants τ_X for $X = W, S, SCN$. The steady state firing rate functions, $X_\infty(\cdot)$, have a sigmoidal profile that has been utilized in many firing rate models [163, 25, 125, 41]:

$$W_\infty(x) = W_{max} \cdot 0.5 \cdot \left(1 + \tanh\left(\frac{x - \beta_W}{\alpha_W}\right)\right), \tag{2.4}$$

$$S_\infty(x) = S_{max} \cdot 0.5 \cdot \left(1 + \tanh\left(\frac{x - \beta_S(h)}{\alpha_S}\right)\right), \tag{2.5}$$

$$SCN_\infty(x) = SCN_{max} \cdot 0.5 \cdot \left(1 + \frac{\tanh\left(\frac{1}{0.7}\right)}{\tanh\left(\frac{1}{\alpha_{SCN}}\right)} \tanh\left(\frac{x - \beta_{SCN}}{\alpha_{SCN}}\right)\right). \tag{2.6}$$

Homeostatic sleep drive

The homeostatic sleep drive (h) regulates sleep propensity and is based on experimentally observed variation in the power of slow wave (0.75 - 4.5 Hz) fluctuations in electroencephalogram (EEG) recordings during sleep [136, 39, 29, 26]. The levels of the homeostatic sleep drive increase exponentially with the time constant τ_{hw} while in wake and decrease exponentially with the time constant τ_{hs} during sleep according to

$$\frac{dh}{dt} = \frac{\mathscr{H}(f_W - \theta_W) \cdot (h_{max} - h)}{\tau_{hw}} + \frac{\mathscr{H}(\theta_W - f_W) \cdot (h_{min} - h)}{\tau_{hs}}\,, \tag{2.7}$$

where $\mathscr{H}$ represents a Heaviside function and h is in units of percent slow wave activity (SWA) power. The time constants τ_{hw} and τ_{hs} are set to experimentally estimated values for typical adult human sleep behavior [136]. The sleep drive h modulates the activity of the sleep-promoting population through the h-dependent activation threshold $\beta_S(h)$ as follows:

$$\beta_S(h) = k_2 \cdot h + k_1 \,. \tag{2.8}$$

In this way as h increases during wake, the sleep promoting population will activate to inhibit the wake population and cause the transition to sleep. Conversely, as h decreases during sleep, the sleep population will inactivate and allow the wake population to activate. We define sleep onset to occur when f_W decreases through θ_W (and h starts to decrease) and wake onset to occur when f_W increases through θ_W (and h starts to increase).

Circadian drive

The input to the SCN population is the circadian drive $c(t)$ which induces a 24h periodic variation of f_{SCN}. We have employed various formulations for the circadian drive in different chapters of this thesis. In Chapter III, the input $c(t)$ is modeled by a simple sinusoidal function and is assumed to be entrained to the 24-hour day.

$$\frac{dc}{dt} = -\omega \sin\theta \,, \tag{2.9}$$

$$\frac{d\theta}{dt} = \omega, \text{ where } \omega = \frac{2\pi}{24} \,, \tag{2.10}$$

which for an initial condition $\Big(c(0), \theta(0)\Big) = \Big(\cos(-\phi\frac{2\pi}{24}), \phi\Big)$ gives the stable solution:

$$c(t) = \cos\left((t-\phi)\cdot\frac{2\pi}{24}\right). \tag{2.11}$$

In Chapter V, the circadian drive $c(t)$ is described by a human circadian clock model

developed by Forger and colleagues and based on a modified van der Pol oscillator [64]. This model involves a circadian drive variable $c(t)$ and a complementary variable $x_c(t)$ governed by the following equations:

$$\frac{dc}{dt} = \left(\frac{\pi}{720}\right)(x_c + B) \tag{2.12}$$

$$\frac{dx_c}{dt} = \left(\frac{\pi}{720}\right)\left[\mu\left(x_c - \frac{4x_c^3}{3}\right) - c\left[\left(\frac{24}{0.99669\tau_x}\right)^2 + kB\right]\right] \tag{2.13}$$

The term B represents light input to the model and involves a variable n that describes the fraction of saturated photoreceptors and is governed by $\frac{dn}{dt} = \alpha(1 - n) - \beta n$, where $\alpha = \alpha_0\left(\frac{I}{I_0}\right)^p$ and I is the light intensity in lux. The circadian drive variable $c(t)$ represents the phase of core body temperature and oscillates between approximately ± 1 with an intrinsic period $\tau_x = 24.2$ h. We assume the circadian oscillator is entrained to a 24 h environmental light schedule which is simulated by a 14:10 Light:Dark cycle with a light input of 500 lux during the light period and 0 lux during the dark period.

In the analysis and figures that follow in this section, we model the circadian drive using the first formulation, i.e. a sinusoidal function. We also summarize representative values of the model parameters employed in Chapter III, as well as in the generation of the time traces in Figure 2.1B.

Model parameters

We have chosen our default parameter set (see Table 2.1) to generate typical human sleep behavior similar to previous work [25]. In Figure 2.1B the time traces of the stable solution of the model are displayed. The wake and sleep durations, dictated by the time intervals when f_W is above or below the threshold value θ_W, respectively, are approximately 15.33 and 8.67 hours. As is typical for entrained adult human sleep,

wake onset occurs at the early rise of the circadian cycle, while sleep onset occurs as SCN activity approaches its minimum.

$W_{max} = 6$ Hz	$\tau_W = 0.1$ hr	$\alpha_W = 0.5$	$\beta_W = -0.37$
$S_{max} = 6$ Hz	$\tau_S = 0.1$ hr	$\alpha_S = 0.175$	
$SCN_{max} = 7$ Hz	$\tau_{SCN} = 0.05$ hr	$\alpha_{SCN} = 0.7$	$\beta_{SCN} = 0$
$g_{sw} = 0.3$	$g_{scnw} = 0.06$	$g_{ws} = 0.28$	$g_{scns} = 0.0825$
$h_{max} = 323.88$	$h_{min} = 0$	$\tau_{hw} = 15.78$ hr	$\tau_{hs} = 3.37$ hr
$k_1 = -0.1$	$k_2 = -0.006$	$\theta_W = 4$ Hz	

Table 2.1: Parameter values for the SWFF model. For $X = W, S, SCN$, α_X and β_X are in units of effective synaptic input. Additionally, for $Y = W, S$, g_{XY} (where $X \neq Y$) has units of (effective synaptic input / Hz). Units for h_{max} and h_{min} are percentage mean SWA. The parameters k_1 and k_2 are measured in effective synaptic input and effective synaptic input/(% mean SWA), respectively. The remaining units are included in the table.

2.1.2 Summary of the model dynamics

In this section, we analyze the model equations (Eq. 2.1-2.10) with the default parameter values (see Table 2.1) and introduce the relevant techniques employed to understand the model dynamics.

Piecewise smooth dynamical system

Switching in the homeostatic sleep drive from increasing during wake to decreasing during sleep introduces a discontinuity in the derivative of h. On either side of this discontinuity, model dynamics are smooth, but the presence of the discontinuity can influence model trajectories at the boundary of the smooth regions. In our system, the switching boundary is $\Gamma = \{f_W = \theta_W\}$, where $\theta_W = 4$ Hz, that separates the system into two smooth vector fields.

To formally define the model as a piecewise smooth system, let $\mathbf{X} = [f_W, f_S, f_{SCN}, h, c, \theta]$. Define $\Gamma^+ = \{f_W > \theta_W\}$ and $\Gamma^- = \{f_W < \theta_W\}$ as the regions on either side of Γ where $F_1(\mathbf{X})$, $F_2(\mathbf{X})$, respectively, are the corresponding vector fields dictating model dynamics. Then we can rewrite our model system as follows:

$$\frac{d\mathbf{X}}{dt} = \begin{cases} F_1(\mathbf{X}) & \mathbf{X} \in \Gamma^+ \\ F_2(\mathbf{X}) & \mathbf{X} \in \Gamma^- \end{cases}$$

On Γ^+, $\frac{dh}{dt} = \frac{h_{max} - h}{\tau_{hw}}$ and on Γ^-, $\frac{dh}{dt} = \frac{h_{min} - h}{\tau_{hs}}$, while the rest of the differential equations are defined as above. Since the vector fields are discontinuous across the switching boundary Γ, we have a Filippov system (see [45]).

As discussed in Section 2.1.2, in Filippov systems as model trajectories approach the switching boundary, they may move along or "slide" on the switching boundary depending on the directions of the vector fields on either side of the boundary. If this occurs, then sliding dynamics on the switching boundary have to be taken into account in the numerical simulations. Sliding along Γ never occurs in our system, because Γ is never simultaneously attracting (or repelling) for the flows in the vector fields on both sides [45]. To show this, for the sliding condition, let us consider $g(\mathbf{X}) = f_W - \theta_W = 0$ to define the boundary Γ. Then, $\nabla g = [1, 0, 0, 0, 0, 0]$ and on Γ:

$$\Big(\nabla g(\mathbf{X})^T \cdot F_1(\mathbf{X})\Big)\Big(\nabla g(\mathbf{X})^T \cdot F_2(\mathbf{X})\Big) =$$

$$\left(\frac{W_{max} \cdot 0.5 \cdot \left(1 + \tanh\left(\frac{g_{scnw} f_{SCN} - g_{sw} f_S - \beta_W}{\alpha_W}\right)\right) - f_W}{\tau_W}\right)^2 \geq 0 \qquad (2.14)$$

for $\mathbf{X} = [\theta_W, f_S, f_{SCN}, h, c, \theta]$.

Condition 2.14 implies that the directions of the vector fields at the switching boundary Γ are the same on either side. Thus, model trajectories cross Γ when transitioning from one vector field to the other and no sliding along Γ occurs. It is important to note that for all $\mathbf{X}$ on Γ where $\nabla g(\mathbf{X})^T \cdot F_1(\mathbf{X})$ is equal to zero, then $\nabla g(\mathbf{X})^T \cdot F_2(\mathbf{X})$ is also zero. Therefore, their product will remain positive even if both quantities change sign.

Fast and slow subsystems in the model

In our model, the homeostatic sleep drive h, the circadian input c, and the circadian phase θ vary more slowly compared to the firing rates f_W, f_S and f_{SCN}. Hence, there is a separation of time scales which allows us to divide our system into a fast and slow subsystem, consisting of neuronal firing rates (f_W, f_S, and f_{SCN}) and the variables h, c, and θ, respectively. Following a similar analysis as in [54, 25, 147], we define $\tau = \max\{\tau_W, \tau_S, \tau_{SCN}\} << \min\{\tau_{hw}, \tau_{hs}, 1/\omega\} = \chi$. These time scales introduce the parameter $\epsilon = \frac{\tau}{\chi}$, where ϵ has small magnitude. Moreover, $\min\{\tau_W, \tau_S, \tau_{SCN}\} = \mu\tau$ and $\max\{\tau_{hw}, \tau_{hs}, 1/\omega\} = \lambda\chi$, where $\lambda = O(1)$ and $\mu = O(1)$. Let us call $\tilde{t} = \frac{t}{\tau}$ the time variable of the fast subsystem and $T = \frac{t}{\chi}$ the time variable of the slow subsystem, such that $\frac{\tilde{t}}{T} = \frac{1}{\epsilon}$. Making the change of variables in Equations (2.1 – 2.7) and (2.9) leads to

$$\frac{d\mathbf{X_{fast}}}{d\tilde{t}} = \mathbf{M}(\mathbf{X_{fast}}, \mathbf{X_{slow}}) \tag{2.15}$$

$$\frac{d\mathbf{X_{slow}}}{d\tilde{t}} = \epsilon\mathbf{N}(\mathbf{X_{fast}}, \mathbf{X_{slow}}) \tag{2.16}$$

where $\mathbf{X_{fast}} = [f_W, f_S, f_{SCN}]$, $\mathbf{X_{slow}} = [h, c, \theta]$, $\mathbf{M}$ and $\mathbf{N}$ are mapped to $\mathbb{R}^3$. Coupling between $\mathbf{X_{fast}}$ and $\mathbf{X_{slow}}$ occurs due to the dependence of the steady state functions $S_\infty(\cdot)$ on h and $SCN_\infty(\cdot)$ on c. We note that the separation of time scales is valid in both vector fields on either side of the switching boundary Γ.

To analyze solution dynamics, we implement the fast-slow decomposition of our system by setting $\mathbf{X_{slow}} = \overline{\mathbf{X_{slow}}}$ to time-fixed parameters and considering equilibrium solutions of the fast subsystem $\left(\frac{d\mathbf{X_{fast}}}{d\tilde{t}} = 0\right)$. We represent the solutions of $\mathbf{M}(\mathbf{X_{fast}}, \overline{\mathbf{X_{slow}}}) = 0$ in terms of the firing rate, f_W, of the wake-promoting population. Specifically, setting c and θ constant and computing solutions with respect to the bifurcation parameter h yields a Z-shaped curve of steady states (Figure 2.2A). The upper and lower branches of the Z-curve represent stable steady states corresponding to the wake and sleep state, respectively. The middle branch represents an unstable

steady state that separates the basins of attraction of the stable steady states. Finally, the folds of each Z-curve are saddle-node bifurcation points where the unstable steady state collides with one of the stable steady states.

For different (fixed) values of c and θ, the Z-shape of the curve is preserved, but the locations of the saddle-node bifurcation points with respect to h change (Figure 2.2A). Thus, as the circadian drive c varies slowly, it affects the bifurcation structure of the fast subsystem. By definition, c varies periodically between -1 and 1, and θ is such that $c = \cos(-\frac{\pi}{12}\theta)$. Hence, a Z-shaped surface is defined between these two extremes of the circadian cycle for the steady state solutions of the fast subsystem as a function of h and c (Figure 2.2B).

When h, c and θ vary slowly, model trajectories traverse the upper plane of the Z-surface during wake and the lower plane during sleep. Transitions between states occur when the trajectory reaches the curve of saddle-node points on either plane and evolves to the other plane. Note that the switching boundary Γ lies between the upper (wake) and lower (sleep) planes of the Z-surface and trajectories cross it during the transition. At Γ crossing, h changes direction leading to trajectory flows that follow a hysteresis loop around the Z-shaped surface. In this way, sleep (wake) onset is initiated when the model trajectory passes over the upper (lower) curve of saddle-nodes.

Bifurcation diagrams were computed numerically using the software AUTO XP-PAUT [59], and the fast-slow Z-shaped surfaces were created using Mathematica.

Sleep onset circle map

To analyze model dynamics and predict solution trajectories, we compute circle maps for the circadian phases of successive sleep onsets as in previous work [25]. Specifically, we define a Poincaré section for sleep onset as the firing rate of the wake-promoting population, f_W, decreasing through the switching boundary $\Gamma =$

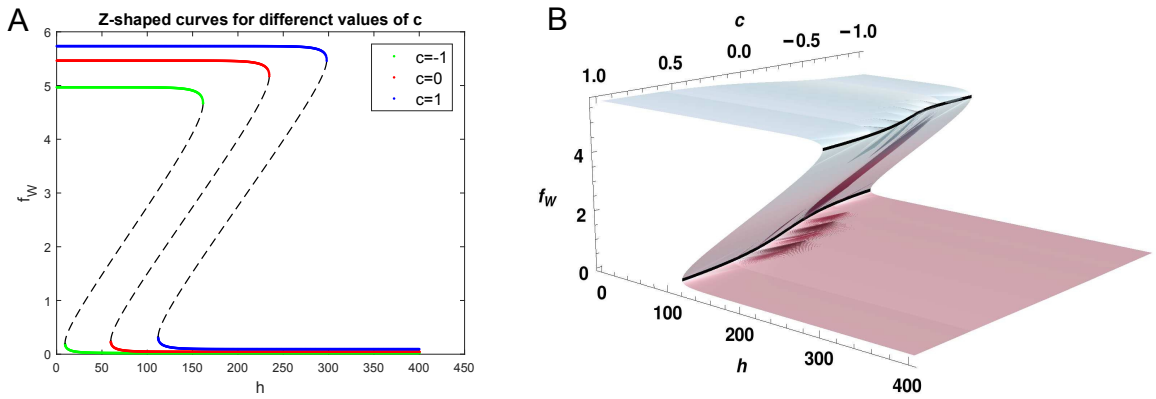

Figure 2.2: Fast-slow decomposition of the SWFF model A: Bifurcation diagrams of the steady state solutions of the fast subsystem (Eq 2.15) with respect to bifurcation parameter h in the $h - f_W$ plane for fixed values of c and θ: $c = -1, \theta = 12$ (green), $c = 0, \theta = 6$ (red) and $c = 1, \theta = 0$ (blue). The upper and lower branches (in green, red and blue) represent the stable steady wake and sleep states, respectively. The middle branch (dashed) represents an unstable state that separates the basins of attractions of the stable steady states. Notice that each curve has different upper and lower saddle-node points that eventually will define a curve in the $c - h - f_W$ space. B: Obtaining the Z-shaped curves for all values of $c \in [-1, 1]$ defines a surface that maintains the general Z-shape. The upper and lower saddle-node points of each Z-shaped curve define upper and lower saddle-node curves (curves in black).

$\{f_W = \theta_W\}$. We define the circadian phase of the n^{th} sleep onset, Φ_n, as the time difference between the intersection of the model trajectory with the section (sleep onset) and the preceding minimum of the f_{SCN} variable divided by the period of the circadian drive $c(t)$:

$$\Phi_n = \frac{1}{24}(\text{time of sleep onset section crossing - time of preceding circadian minimum}) \tag{2.17}$$

We then define $\Pi : [0, 1] \to [0, 1]$ as the circle map with $\Phi_{n+1} = \Pi(\Phi_n)$.

To compute the map Π, we simulate the model from initial conditions corresponding to sleep onset occurring at each circadian phase. Recall that the transition to sleep is initiated when the model trajectory passes over the curve of saddle-node points on the upper plane of the Z-shaped surface of steady state solutions of the fast subsystem. Thus, we select points on the upper saddle-node curve as a stable solution of the sleep-

wake network that is near sleep onset and use those values for initial conditions for the sleep-wake network variables in the map construction. We compute these values on the upper saddle-node curve for all c values over one circadian cycle by two-parameter numerical continuation, implemented in AUTO using XPPAUT [59]. By numerically integrating the model from these initial conditions, the circadian phases of sleep onsets are computed as the trajectories pass through the switching boundary Γ. From the majority of these initial conditions, model trajectories immediately transition down to the lower plane of the Z-shaped surface crossing Γ on the way. However, there is an interval of circadian phase values (where Φ_n is between approximately 0.2 and 0.4) for which the model trajectory does not immediately transition to sleep but instead continues to move along the upper plane until eventually transitioning at a later circadian phase. This produces a horizontal gap in the map. This phenomenon occurs during the rising phase of c that promotes the waking state at higher values of the homeostatic sleep drive h. Dynamically speaking, the variables c and h vary on similar time scales at these moments, and the drive to sleep associated with increasing h is balanced by a drive to wake associated with increasing c. To overcome this issue and fill in the horizontal gap in the map, for this interval of circadian phases, we substituted initial condition values that lie on the unstable manifold associated with the saddle of the upper saddle-node point that are closer to the switching boundary Γ (purple points in Figure 2.3A).

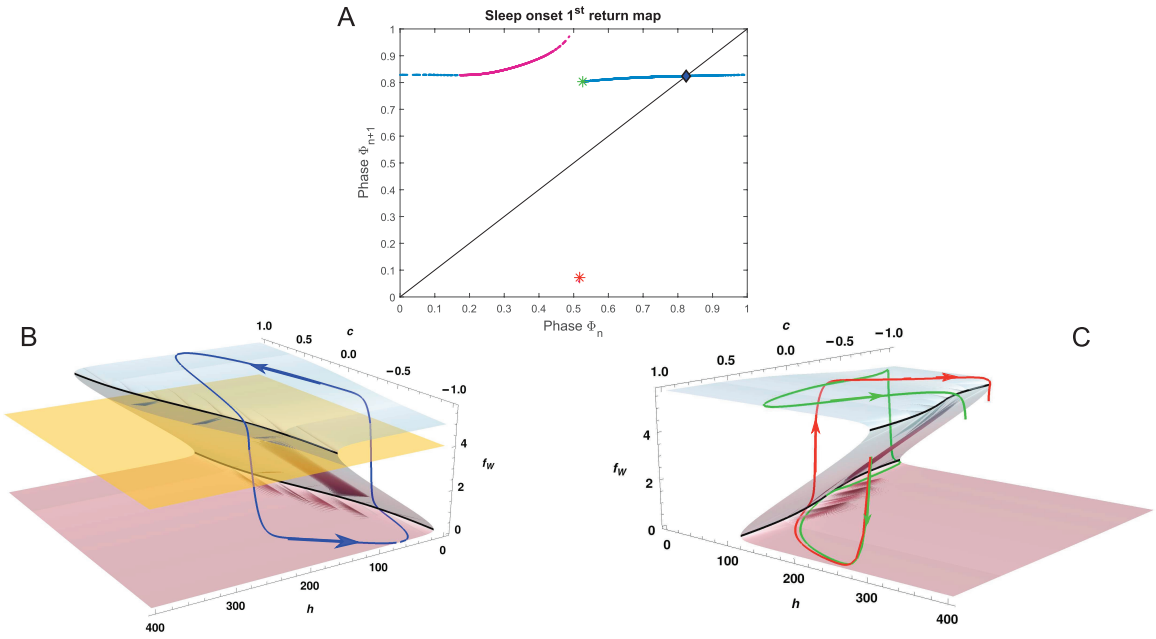

Figure 2.3: Circle map and model trajectories relative to the fast-slow decomposition of the SWFF model. A: First return circle map for circadian phase of $n+1^{st}$ sleep onset, Φ_{n+1} as a function of circadian phase of n^{th} sleep onset, Φ_n. Purple points indicate circadian phases obtained by integrating the model from initial conditions "forced" to lie on the unstable manifold. The blue diamond corresponds to the stable orbit shown in panel B (in blue). The green and red asterisks correspond to circadian phases associated with the trajectories in panel C (red and green, respectively). B: The stable trajectory for the default parameter set (blue curve) plotted on the Z-surface computed from equilibrium solutions of the fast subsystem in Eq. (2.15). Sleep is initiated when the trajectory falls off the upper saddle-node curve. Sleep onset is defined as the time the trajectory crosses the switching boundary $\Gamma = \{f_W = 4\}$ (yellow plane) and h starts decreasing. C: Trajectories with initial conditions on either side of the gap in the sleep onset map exhibit distinct behavior. The green trajectory becomes tangent to the lower saddle-node curve, resulting in a longer sleep episode, while the red one passes over the saddle-node curve and transitions to the wake state.

Figure 2.3A illustrates the circle map; the circadian phase of the n^{th} crossing of the section defined by Γ, Φ_n, is on the $x-$axis, and the circadian phase of the $n+1^{st}$ section crossing Φ_{n+1} is on the $y-$axis. This first return sleep onset map is periodic in phase, consists of two branches, and has one stable fixed point at approximately (0.824,0.824), indicating that sleep onset of the stable solution occurs close to the trough of the circadian cycle. The stable solution trajectory is shown relative to the Z-shaped surface in Figure 2.3B.

The map is piecewise-smooth due to the discontinuity or gap around $\Phi_n = 0.5$. The left branch of the map relative to the discontinuity has an infinite slope which is a consequence of trajectories approaching a tangent intersection with the saddle-node curve of the Z-shaped surface (Figure 2.3C). To see this, consider trajectories initiated on either side of the gap with sleep onsets very close to the peak of the circadian drive ($c = 1$, red and green curves). The trajectory initiated on the infinite slope to the left of the gap (red curve) exhibits a short sleep episode, as it jumps up from the lower saddle-node curve and transitions to the wake plane resulting in the next sleep onset phase of about $\Phi_{n+1} = 0.0722$. By contrast, the trajectory initiated on the right of the gap (green curve) becomes tangent to the lower saddle-node curve (grazing), resulting in a longer sleep episode. As the green trajectory evolves further, wake onset occurs close to the circadian minimum (that is $c = -1$), followed by a long wake episode resulting in the next sleep onset at a phase of about $\Phi_{n+1} = 0.8033$.

2.2 Three-state sleep-wake network model

In this section we first describe our three-state sleep-wake regulatory network model and then discuss the methods used to construct the one-dimensional circle maps that represent its dynamics.

2.2.1 Model equations of the three-state model

In Chapters IV and VI, we utilize a previously developed, sleep-wake regulatory network model to simulate sleep-wake behavior [53, 63, 129]. This model is based on neurotransmitter-mediated interactions between neuronal populations that promote the states of wake, NREM and REM sleep (Figure 2.4). REM-promoting populations include the REM-active, cholinergic areas of the laterodorsal tegmental nucleus (LDT) and pedunculopontine tegmental nucleus (PPT). Similar to the SWFF model, mutual inhibition between the wake-promoting and NREM sleep-promoting populations

introduces a flip-flop switch governing transitions between sleep and wake states. Transitions between NREM and REM sleep states are dictated according to the reciprocal interaction hypothesis for REM sleep [81], in which the wake-promoting population projects inhibitory synapses to the REM sleep-promoting population, while the REM sleep-promoting population projects excitatory synapses back to the wake-promoting population. The model also represents the suprachiasmatic nucleus (SCN) which is entrained to the environmental light cycle, and displays a 24-hour variation in neural firing.

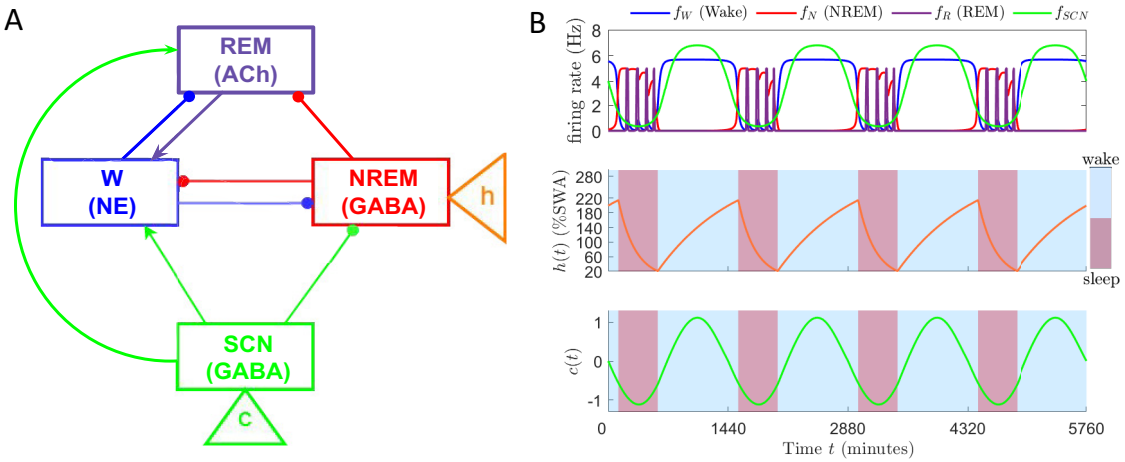

Figure 2.4: A physiologically based, three-state model for sleep-wake regulation. A: Schema of the model network summarizing interactions among the wake-promoting, NREM-promoting, REM-promoting and suprachiasmatic nucleus (SCN) neuronal populations with circles denoting inhibitory and arrows denoting excitatory synaptic connections. The representative neurotransmitters for each population are also indicated (NE: noradrenaline, ACh: acetylcholine, GABA: gamma aminobutyric acid). B: Time traces showing the evolution of the model variables corresponding to the stable solution with one daily sleep episode. The top panel includes the firing rates f_W (Wake), f_N (NREM), f_R (REM), f_{SCN}. The middle panel shows the evolution of the sleep homeostat, h, and the bottom panel shows the evolution of the circadian drive, c. The light blue and rose backgrounds correspond to the times at which the model is in wake and sleep, respectively.

As before, neuronal population activity is modeled using a firing rate formalism that captures averaged behavior of spike rates of the neuronal populations, f_W, f_N, f_R, where W, N, and R denote Wake, NREM and REM, respectively. The

neurotransmitter concentration released as a result of activity of the presynaptic neuronal population depends on the mean firing rate of the presynaptic neuronal population. In particular, we assume that a firing rate f_X induces instantaneous expression of neurotransmitter concentration that is described by its steady state function: $C_i(f_X) = \tanh\left(\frac{f_X}{\gamma_i}\right)$, where $X = W, N, R, SCN$ and corresponding $i =$ NE (noradrenaline), G (GABA), ACh (acetylcholine), S (GABA expressed by the SCN). The postsynaptic firing rates, $f_X(t)$ (in Hz), saturate to their steady state firing rate response functions with time constants τ_X for $X = W, N, R, SCN$. The steady state firing rate functions, $X_\infty(\cdot)$, have a sigmoidal profile that has been utilized in many firing rate models [41, 123, 124, 24, 163]. Here, $X_\infty(z) = \frac{X_{max}}{2}\left(1 + \tanh\left(\frac{z-\beta_X}{\alpha_X}\right)\right)$.

Neuronal populations

Hence, in this formalism the firing rates f_X for $X = W, N, R, SCN$ are governed by the following equations:

$$\frac{df_W}{dt} = \frac{W_\infty(g_{ACh,W}C_{ACh}(f_R) + g_{S,W}C_S(f_{SCN}) - g_{G,W}C_G(f_N)) - f_W}{\tau_W} \tag{2.18}$$

$$\frac{df_N}{dt} = \frac{N_\infty(-g_{NE,N}C_{NE}(f_W) - g_{S,N}C_S(f_{SCN}) - g_{G,N}C_G(f_N)) - f_N}{\tau_N} \tag{2.19}$$

$$\frac{df_R}{dt} = \frac{R_\infty(g_{ACh,R}C_{ACh}(f_R) - g_{NE,R}C_{NE}(f_W) - g_{S,R}C_S(f_{SCN}) - g_{G,R}C_G(f_N)) - f_R}{\tau_R} \tag{2.20}$$

$$\frac{df_{SCN}}{dt} = \frac{SCN_\infty(c(t)) - f_{SCN}}{\tau_{SCN}} \tag{2.21}$$

The parameters X_{max}, α_X, and β_X represent the maximum firing rate, sensitivity of response, and half-activation threshold, respectively. The weights $g_{i,X}$ convert the concentrations C_i into effective synaptic input. A positive sign in front of $g_{i,X}$ denotes excitation of the postsynaptic population X due to release of the neurotransmitter i; a negative sign denotes inhibition.

Circadian Drive

Simulations of the three-state model in this thesis have been conducted using the limit cycle model for the circadian drive [64] described earlier that includes equations 2.12-2.13.

Homeostatic Sleep Drive

The homeostatic sleep drive (h) regulating sleep propensity is modeled using equation 2.7 and modulates the activity of the NREM sleep-promoting population through $\beta_N(h)$, a linear function of h.

Model Parameters

All default model parameter values are given in Table 2.2. This parameter set is used in the work presented in Chapters IV and VI.

$W_{max} = 6$ Hz	$\tau_W = 23$ min	$\alpha_W = 0.4$	$\beta_W = -0.4$
$N_{max} = 5$ Hz	$\tau_N = 10$ min	$\alpha_N = 0.2$	
$R_{max} = 5$ Hz	$\tau_R = 1$ min	$\alpha_R = 0.1$	$\beta_R = -0.8$
$SCN_{max} = 7$ Hz	$\tau_{SCN} = 0.5$ min	$\alpha_{SCN} = 0.7$	$\beta_{SCN} = -0.1$
$g_{ACh,W} = 0.8$	$g_{S,W} = 0.1911$	$g_{G,W} = 1.4928$	
$g_{NE,N} = 1.5$	$g_{S,N} = 0.2141$	$g_{G,N} = 0$	
$g_{ACh,R} = 2.2$	$g_{NE,R} = 10.7473$	$g_{S,R} = 0.8$	$g_{G,R} = 1.07$
$h_{max} = 323.88$	$h_{min} = 0$	$\tau_{hw} = 946.8$ min	$\tau_{hs} = 202.2$ min
$k_1 = -0.1$	$k_2 = -0.0045$	$\theta_W = 2$ Hz	

Table 2.2: Parameter values for the network model for human monophasic sleep. For $X = W, N, R, SCN$, α_X and β_X are in units of effective synaptic input. Additionally, for $i = NE, G, ACh, S$, g_{iX} has units of (effective synaptic input / Hz). Units for h_{max} and h_{min} are percentage mean SWA. The parameters k_1 and k_2 are measured in effective synaptic input and effective synaptic input/(% mean SWA), respectively. The remaining units are included in the table.

For the default parameter values, the model produces a stable solution representing monophasic sleep with 16.11 hours of wake and 7.89 hours of sleep including 6.58 and 1.31 hours of NREM and REM sleep, respectively (Figure 2.4). During each sleep

episode, cycling between NREM and REM sleep produces four distinct REM bouts. For the stable default solution, the sleep onset phase (defined as in equation 2.17) is $\Phi = 0.829$, so the sleep onset occurs on the decreasing phase of c. This is consistent with the relationship between sleep onset and the phase of core body temperature in typical adult human sleep behavior.

2.2.2 Summary of the three-state model dynamics

In this section, we analyze the model equations (Eq. 2.18-2.21 and 2.7, 2.12-2.13) with the default parameter values (see Table 2.2) and describe model dynamics using the techniques introduced earlier.

Fast-slow decomposition of the three-state model

As in the SWFF model, the steady state solutions of the fast subsystem, which are represented in terms of the firing rate f_W of the wake-promoting population, form a Z-shaped curve with respect to h at each value of $\mathbf{c}$ (Figure 2.5A). The upper branch of the Z-shaped curve comprises the stable steady state solutions that correspond to the wake state. The middle and lower branches correspond to unstable fixed points of the fast subsystem, and the folds of the Z are saddle-node bifurcation points where two steady states coalesce. Associated with the lower branch of unstable solutions are stable periodic solutions corresponding to NREM-REM cycling in which the REM firing rate f_R displays high amplitude oscillations and f_W displays low amplitude oscillations. The unstable fixed points of the fast subsystem separate the basins of attraction for the stable fixed point and the stable periodic solution.

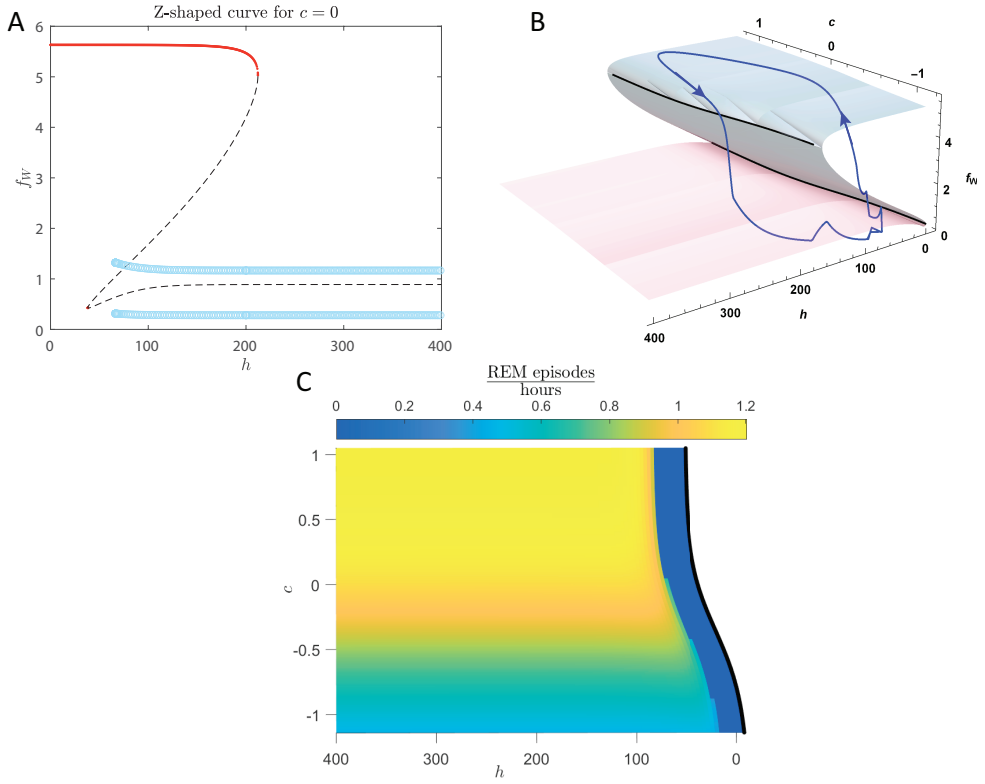

Figure 2.5: Fast-slow decomposition of the three-state sleep-wake model. A. The Z-shaped curve obtained by the fast-slow decomposition for $c = 0$ illustrates the steady state solutions of the variable f_W as a function of the varying parameter, h. The red solid and black dashed curves correspond to stable and unstable steady state solutions of the fast subsystem, respectively. The light blue circles correspond to the periodic solution representing the NREM-REM cycling occurring during the sleep state. B. The fast-slow Z-shaped surface for varying h and c values and the stable orbit (blue curve) of the model for the default parameter set. C. Frequency plot of NREM-REM cycling for various values of the parameters c and h, corresponding to the periodic solutions in the fast subsystem during the sleep state. The black curve corresponds to the lower saddle-node points of the Z-shaped surface. The darkest blue region (to the left of the saddle-node curve) corresponds to (h, c) values for which the stable solution of the fast subsystem is not periodic and corresponds to the wake state.

For each fixed **c** value we obtain similar solutions with respect to h which collectively form a Z-shaped fast-slow surface on which trajectories of the full system evolve (Figure 2.5B). On this surface the lower manifold representing the sleep state captures the periodic solutions corresponding to the oscillations of f_R which occur at different frequencies depending on the strength of the circadian rhythm drive (c) (Figure 2.5C).

Lower values of c lead to lower frequency NREM-REM cycling with longer REM bouts, while higher values of c yield higher frequency cycling with shorter REM bouts. Additionally, NREM-REM cycling is more sensitive to changes in the strength of the circadian drive than in the strength of the homeostatic sleep drive.

As explained previously, in the two-state model the lower branch of the Z-shaped curve is stable, and the sole mechanism for transition from sleep to wake is the passage through the saddle-node point at the lower knee of the Z-shaped curve. In contrast, transitions from sleep to wake in our three-state model depend on the interaction of the lower saddle-node point with the periodic solution representing the REM oscillations [54].

Sleep onset circle map of the three-state model

The map is constructed by tracking the circadian phases when trajectories cross the $f_W = \theta_W$ section during numerical integration of the model from initial conditions representing sleep onsets occurring across the range of circadian phases.

Following the process described in Section 2.1.2, we obtain initial conditions that place the sleep-wake variables on a stable solution of the sleep-wake subsystem (f_W, f_N, f_R, h) near the transition to sleep that is associated with a fixed value of the circadian drive c, and to place the circadian rhythm variables on a stable solution of the circadian subsystem (c, x_c, n) associated with the same fixed value of c. Assumption of a fixed light:dark schedule is required for the map computation to maintain a rigorous definition of circadian phase, but, based on previous work, we expect that similar results would be obtained if light intensity was allowed to vary with behavioral state (see [128], Chapter VI and Discussion in Chapter IV for more details).

The map for the three-state sleep-wake model is piecewise, non-monotonic, non-invertible and exhibits both large vertical discontinuities or gaps, and smaller gaps occurring at cusps that separate distinct branches of the map (Figure 2.6). The

separate branches of the map correspond to sleep-wake cycles with distinct sleep and wake bout durations, and numbers of REM bouts. For default parameter values, the map has one stable fixed point at $\Phi_n = 0.829$ corresponding to the stable periodic solution displayed in Figure 2.4. This solution has one sleep episode per circadian day with a duration of 7.89 h; each sleep episode contains four REM bouts.

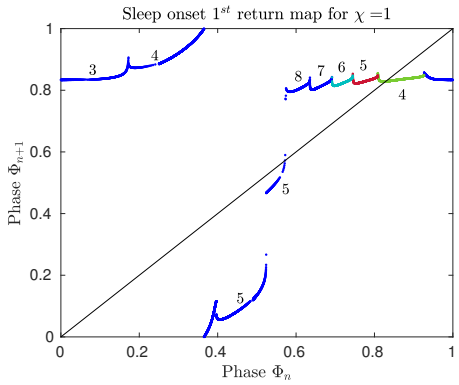

Figure 2.6: One dimensional circle map illustrating the circadian phase of the $n+1$st sleep onset, Φ_{n+1} as a function of circadian phase of the nth sleep onset, Φ_n. For each branch of the map we indicate the distinct number of REM bouts occurring in sleep episodes initiated at the associated circadian phase. We distinguish the branches representing 4 REM bouts (green), 5 REM bouts (red) and 6 REM bouts (light blue), as these are significant for our later analysis.

The map exhibits a large vertical gap close to the phase associated with the peak of the circadian drive ($\Phi_n = 0.5$), similar to the gap in the map of the SWFF model (Figure 2.3A). The left branch at the discontinuity has an infinite slope which is a consequence of trajectories starting from these initial conditions approaching a tangent intersection with the saddle-node curves of the Z-shaped surface (grazing).

The unique features of maps for the three-state model are the cusp gaps between map branches for trajectories with distinct numbers of REM bouts. The number of REM bouts during a sleep episode depends on how the trajectory traverses the periodic solutions on the lower manifold of the Z-surface, especially as it approaches the lower curve of saddle nodes. Trajectories that are initiated at similar sleep onset phases may approach the lower saddle-node curve at slightly different circadian phases

resulting in a difference of one REM bout and thus different subsequent sleep onset phases, placing their corresponding phase points on distinct map branches.

CHAPTER III

Bifurcations of Sleep Patterns Under Circadian and Homeostatic Variation

3.1 Introduction

In this chapter[1], we investigate changes in sleep patterns under homeostatic and circadian variation using the SWFF model presented in Chapter II. Specifically, we consider varying the time constants of the homeostatic sleep drive and the temporal profile of the circadian drive. Several experimental studies have shown that characteristics of sleep homeostasis depend on individual traits such as age and sex [48, 136, 87] and may vary with development [136]. For example, the transition from polyphasic (multiple sleeps per day) to monophasic (one sleep per day) sleep behavior that occurs in infancy/early childhood is thought to result from differences in the time constants of the homeostatic sleep drive dictating the accumulation and dissipation of sleep pressure [89, 138, 88]. The temporal profile of the circadian drive, reflecting the firing rate of neurons in the SCN, can also vary with age [38], the Earth's latitude, as well as in response to seasonal changes in day length. In particular, the mean duration of high SCN firing activity was shorter in animals entrained to a short photoperiod (i.e., daily illumination) (Light:Dark 8 h:16 h) and longer in those entrained to a long

[1]A manuscript on these results has been accepted for publication in *SIAM Journal on Applied Dynamical Systems*.

photoperiod (Light:Dark 14 h:10 h)[117]. Similar results were reported in [109, 157] who found longer intervals of peak firing activity of the SCN during long days and shorter peak firing intervals during short days.

Physiologically-based models of sleep-wake networks are based on the interactions of neuronal populations that promote wake and sleep states, with the suprachiasmatic nucleus (SCN) that generates the circadian rhythm [125, 17, 53, 71, 134, 100, 24]. The simplest of such ordinary differential equation (ODE) -based models [125] has been formally reduced to the same form as the Two Process model [147] and a numerical study suggests that similar types of phase-locked solutions are obtained as the time constants of the homeostatic sleep drive and amplitude of circadian drive are varied [127]. However, to our knowledge, the types of bifurcations governing the gain and loss of stability of the phase-locked solutions in the ODE model have not been reported.

Here, we draw on multiple mathematical methods, including numerical computation of circle maps, to analyze the bifurcations of phase-locked solutions in an ODE-based sleep-wake flip-flop model. Motivated by changes that have been documented in the experimental literature, we consider the effects of variation in both the homeostatic sleep and the circadian drives on the types of bifurcations leading to changes in the number of daily sleep episodes. To our knowledge, this has not been thoroughly analyzed in a physiologically-based sleep-wake model previously.

Previous analysis of mathematical models of sleep-wake regulation has considered the effects of changing homeostatic time constants in the transition from polyphasic to monophasic sleep [127, 147, 14]. However, these studies have not taken into account the effects of the steepness of the circadian waveform and how this interacts with changing homeostatic time constants. Therefore, we extend these previous findings by additionally considering how the temporal profile of the circadian drive affects the bifurcation sequences of entrained sleep-wake patterns that are observed in the transition from polyphasic to monophasic sleep behavior and driven by changing

homeostatic time constants.

To identify types of bifurcations and understand how they arise in the SWFF model, we employ multiple methods (described in detail in Chapter II) to analyze model dynamics and numerically compile a two-parameter bifurcation diagram.

Similarly to the maps explicitly derived from the Two Process model, SWFF circle maps are discontinuous with an infinite slope on one side of the vertical discontinuity. Tracking fixed points of the circle maps as the homeostatic and circadian drives are varied allows us to characterize the types and sequences of bifurcations when different phase-locked solutions lose and gain stability. Finally, to explain changes observed with increasing steepness of the circadian drive waveform, we consider the limit of the circadian drive as a step function which we call the circadian hard switch model (CHS). This limit introduces a second switching boundary to the piecewise smooth model, and we analyze its bifurcation sequence as the homeostatic sleep drive is varied to verify the trends observed in the original SWFF model. Thus, with these multiple techniques and numerical simulations, we obtain a complete understanding of the dynamics of the SWFF model, and detect and classify the types of bifurcations that occur as two key parameters are varied.

The chapter is organized as follows: in Section 3.2 we briefly discuss the mathematical model utilized in this study. In Section 3.3 we analyze the bifurcations of entrained sleep-wake patterns under variation of the time constants of the homeostatic sleep drive and the duration of peak activity of the circadian drive waveform. In Section 3.4 we formulate the circadian hard switch model and describe the bifurcations in this case. In Section 3.5, we provide a brief discussion of our results.

3.2 Sleep-Wake Flip-Flop (SWFF) model

In this work, we employ the SWFF model presented in Chapter II using a sinusoidal function to produce the 24h-periodic signal of the circadian oscillator. Parameter values

are shown in Table 2.1 and generate a sleep pattern typical for healthy young adults. The wake and sleep durations are approximately 15.33 and 8.67 hours, respectively. As is typical for entrained adult human sleep, wake onset occurs at the early rise of the circadian cycle, while sleep onset occurs as SCN activity approaches its minimum (Figure 2.1B).

3.3 Analysis of bifurcation sequences in the SWFF model

For our analysis of bifurcations in the SWFF model, we first identify the bifurcation sequences associated with the emergence and change of stable, phase-locked solutions as the time constants of the homeostatic sleep drive are varied. We then consider how the steepness of the circadian waveform affects the bifurcations of stable, phase-locked solutions and the associated bifurcation sequences as homeostatic time constants vary. We end this section by examining how the bifurcation sequences change in the regime of the fastest homeostatic time constants when sleep onset circle maps may be continuous.

3.3.1 Varying time constants of the homeostatic sleep drive

To examine how decreasing the homeostatic time constants τ_{hs} and τ_{hw} affects model solutions, we introduce a scaling constant $k \in (0, 1]$ that multiplies both τ_{hs} and τ_{hw} in Eq. 2.7. This is a simple scaling that preserves the ratio between time constants and is consistent with approaches in previous work [147, 14]. We numerically computed model solutions (Figure 3.1A) with respect to the bifurcation parameter k to understand the change in the types of stable phase-locked solutions obtained as we decrease k from 1. Specifically, we tracked the timing and duration of the sleep episodes of the stable solutions (black intervals) over the course of 10 days.

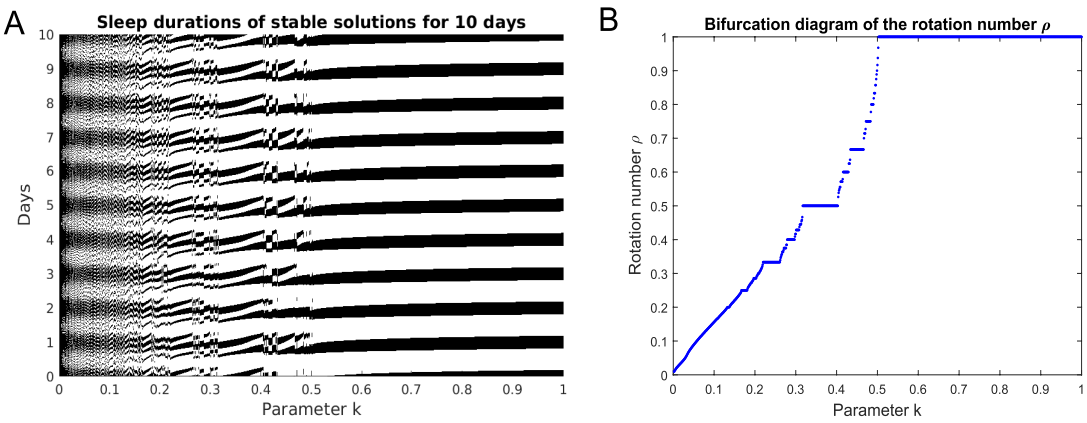

Figure 3.1: Multiple sleep episodes per day occur as time constants for the homeostatic sleep drive are decreased. A: Simulated sleep periods (dark intervals) over the course of 10 days as the homeostatic sleep drive time constants are decreased by the scaling parameter k (x-axis). B: Bifurcation diagram of stable solutions in terms of the rotation number ρ for the default parameter set. The parameter k is on the $x-$axis and the rotation number ρ, defined as the number of circadian days over the number of sleep episodes in the stable sleep pattern is on the y-axis. The step size for k was 0.001.

We found that the number of sleep episodes per day increased as the time constants for the homeostatic drive decreased. At the default value $k = 1$, the model produces one sleep episode per day (which we define here as a 24-hour cycle measured between two minimums of the circadian variable $(c(t))$. As we reduce k, the stability of solutions with one sleep episode per day is lost, and higher order patterns in which some days contain two sleep episodes may occur. In the interval $(k \in [0.317, 0.403])$ a stable solution with two sleep episodes per day emerges. For smaller values of k, higher order patterns in which some days contain three sleep episodes appear, eventually resulting in the stable solution with three sleep episodes per day, and so on.

To quantify the sleep patterns associated with the attracting periodic orbits obtained for each value of k, we define the rotation number, ρ, to be the number of circadian days q over the number of sleep episodes p occurring in one period of the stable orbit, i.e. $\rho = \frac{q}{p}$. Tracking ρ as k is decreased from 1 to 0 (Figure 3.1B),

we find that the rotation numbers vary as dictated by a Farey sequence [75, 11]. In between neighboring intervals of k displaying solutions with rotation numbers $\rho_1 = \frac{a}{b}$ and $\rho_2 = \frac{c}{d}$, where the greatest common divisor $\gcd(a, b) = 1$, $\gcd(c, d) = 1$, and $|ad - bc| = 1$ is a k interval with rotation number $\rho = \frac{a+c}{b+d}$. Such a Farey sequence of rotation numbers will generate a Devil's staircase-like structure for the rotation number as a function of k. This suggests that the stable solutions follow a period-adding bifurcation sequence that is consistent with previous work on systems governed by monotonic circle maps with discontinuities [75, 14, 42]. Here, we numerically detect a subset of a Farey sequence of rotation numbers (see Appendix B for a description of the algorithm used for the computation of the bifurcation diagram of ρ).

Interestingly, for small values of k ($0 < k \leq 0.18$), we obtain a denser set of rotation numbers from the computed solutions compared to the rotation numbers observed for larger values of k. For small k, the numerical results suggest that solutions with rotation numbers for all rational numbers less than about $\frac{1}{4}$ may exist. This is expected as sufficiently fast homeostatic time constants will result in continuous sleep onset circle maps. This occurs because fast time constants will prevent model trajectories from making tangent intersections with the saddle-node curves of the $Z-$shaped surface. In this case, the theory for monotonic, continuous circle maps guarantees that solutions exist with rotation numbers for all rational numbers [75, 11].

3.3.1.1 Bifurcation sequences for emergence of stable solutions

To identify the types of bifurcations leading to the gain (or loss) of stability of different sleep patterns for decreasing k, we track how the stable model trajectories and sleep onset maps evolve as we reduce k for representative solutions associated with $\rho = 1, \frac{2}{3}$, and $\frac{1}{2}$. Our analysis suggests that other stable solutions with $\rho \in [\frac{1}{2}, 1]$ will show the same bifurcation sequences. Solutions with smaller ρ values may show different bifurcation sequences and are considered in Section 3.3.4.

For $k = 1$, the associated solution has rotation number $\rho = 1$. As k decreases, we describe the bifurcations associated with the loss of the $\rho = 1$ solution. Similarly, we identify $k-$intervals associated with the existence of solutions with $\rho = \frac{2}{3}$ and $\frac{1}{2}$ and observe the bifurcation sequences associated with the emergence and loss of these solutions. These bifurcation sequences will include saddle-node (SN) bifurcations and border collision bifurcations of both stable (BC-S) and unstable (BC-U) fixed points of the maps. A border collision bifurcation in the map occurs when the border of a map curve intersects the diagonal, and therefore, a fixed point is created or destroyed. In the listing of the sequences, for all cases except $\rho = 1$, the leftmost and rightmost bifurcations create and destroy, respectively, the stable solution with rotation number $\rho = \frac{q}{p}$ as k is decreased.

Border collision $\rightarrow$ saddle-node

We first consider the loss of stability of the $\rho = 1$ solution as k is decreased from 1. The smallest value of k for which this solution is stable is $k = 0.503$ (Figure 3.2A,B). As k is decreased towards this value, the stable periodic orbit shifts on the $Z-$shaped surface such that sleep onset occurs at earlier phases. The sleep onset map for $k = 0.503$ reveals a saddle-node bifurcation to the right of the discontinuity (Figure 3.2A). The unstable fixed point associated with the saddle-node bifurcation was created at a higher value of k ($k = 0.504$) in a border collision bifurcation on the right side of the discontinuity (referred to as a Type I border collision in [14, 42]). Numerical simulations suggest that at the border collision bifurcation of the map the unstable orbit makes a tangent intersection with the curve of saddle-node points on the upper plane of the $Z-$shaped surface, also called a grazing bifurcation of the flow [45]. Thus, as k decreases, the $\rho = 1$ solution loses stability in the bifurcation sequence of

$$\text{BC-U} \rightarrow \text{SN}.$$

Saddle-node → border collision → border collision

Next we describe the bifurcation sequences associated with the emergence and loss of a stable solution with alternating 1 and 2 sleeps per 24-h circadian cycle ($\rho = \frac{2}{3}$). This solution gains stability at $k = 0.4663$ and loses stability at $k = 0.434$. Fixed points associated with this solution appear in the 3rd return sleep onset map (Figure 3.2C,D). These maps consist of 3 separate branches, each showing an infinite slope at its right end and a finite slope at its left end (see Appendix A). Note that the two segments for lower Φ_{n+3} values form one connected branch (modulo 1) due to periodicity of the circle map. At $k = 0.4663$, the map shows a saddle-node bifurcation near the infinite slope end of the map branches (numbered 1-3 in Figure 3.2C). The unstable fixed points are destroyed in a border collision (referred to as a Type II border collision in [14, 42]) at a slightly lower value of k ($k = 0.466$). Numerical solutions suggest that this border collision is associated with the unstable orbit making a tangent intersection with the upper curve of saddle-node points of the $Z-$shaped surface. As k decreases to $k = 0.434$, the map transitions so the stable fixed points move towards the left end of the map branches and disappear in a border collision bifurcation (Figure 3.2D). Numerical simulations indicate that this border collision bifurcation occurs due to a tangent intersection with the upper curve of saddle-node points of the $Z-$shaped surface. Thus, as k is decreased, the emergence and disappearance of the $\rho = \frac{2}{3}$ stable solution occurs in the bifurcation sequence

$$\text{SN} \rightarrow \text{BC-U} \rightarrow \text{BC-S}.$$

We find that other stable solutions for lower values of k also emerge through this same bifurcation sequence. For example, the $\rho = \frac{1}{2}$ solution with two sleep episodes per circadian cycle is stable in the interval $k \in [0.317, 0.403]$. Fixed points for this solution appear in the second return sleep onset maps which in this regime consist of

two separate branches, each with an infinite slope at the right end and a finite slope at the left end (Figure 3.2E,F). Again, as k decreases the solution gains stability in a saddle-node bifurcation at the right end of the map branches where the unstable fixed points are destroyed in a border collision at $k = 0.401$. Numerical simulations suggest that the unstable orbit makes a tangent intersection with the upper curve of saddle-node points of the $Z-$shaped surface. The fixed points disappear in a border collision with the left end of the map branches (Figure 3.2F), where again the stable orbit makes a tangent intersection with the upper curve of saddle-node points of the $Z-$shaped surface (Figure D.1 in Appendix D).

We have demonstrated that as k varies, the appearance of tangent intersections of model trajectories with the curves of saddle-node points of the $Z-$shaped surface influence the occurrence of the bifurcations, and thereby, the emergence of stable orbits. The presence of tangent intersections depends, in part, on the circadian waveform and highlights the importance of the circadian drive on the bifurcation sequences.

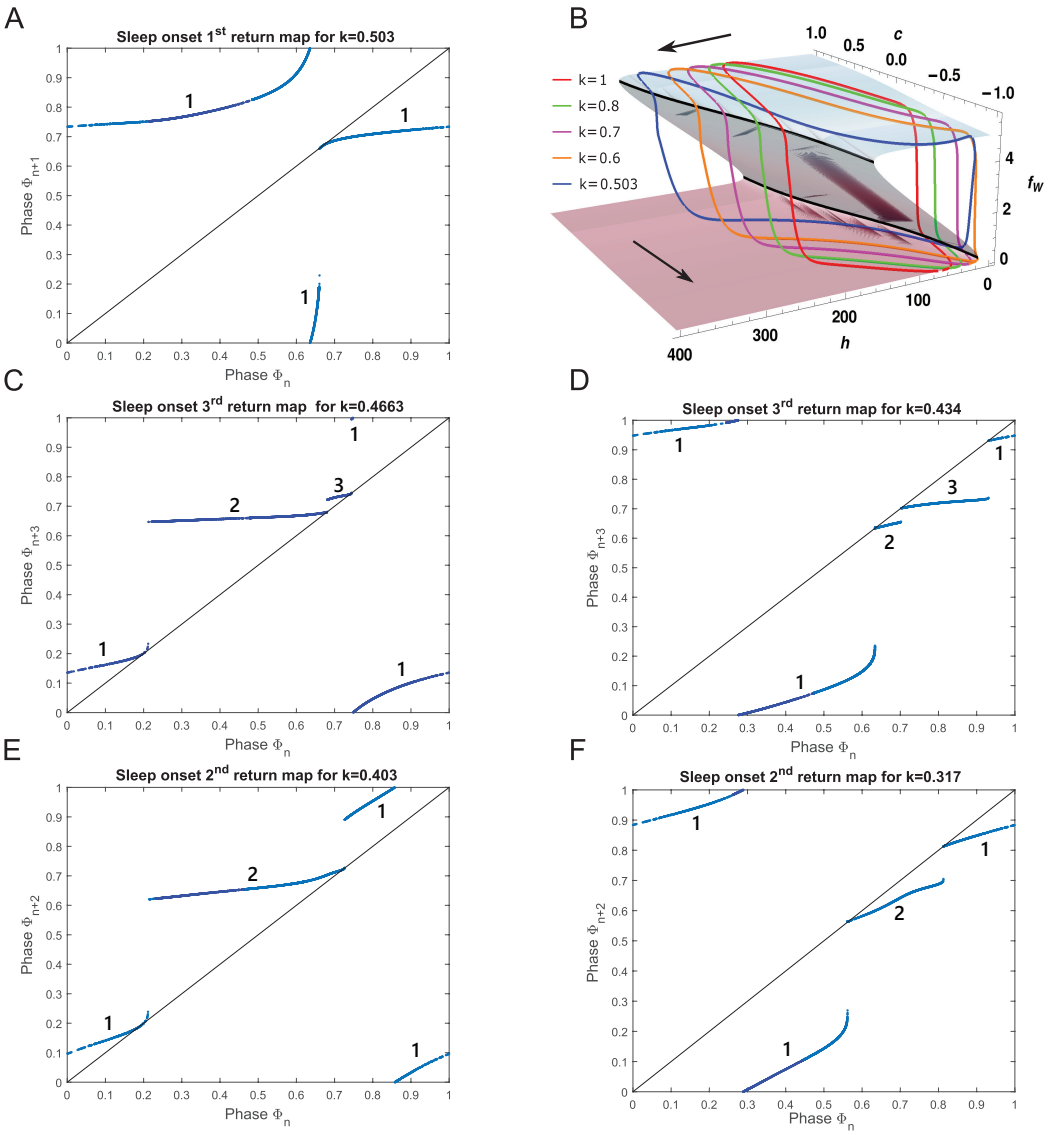

Figure 3.2: Sleep onset circle maps reveal the types of bifurcations at the emergence and disappearance of stable solutions as k is varied. Distinct branches of the circle maps are labelled by numbers 1,2 and 3 as needed. A: The first return sleep onset map for $k = 0.503$, the smallest value where the one sleep episode per day solution ($\rho = 1$) is stable, shows a saddle-node bifurcation. B: Evolution of stable $\rho = 1$ periodic orbits plotted in relation to the $Z-$shaped surface in the $c - h - f_W$ space as k approaches $k = 0.503$. Each closed orbit corresponds to the stable solution for a particular value of the parameter k: $k = 1$ (red), $k = 0.8$ (green), $k = 0.7$ (magenta), $k = 0.6$ (orange), $k = 0.503$ (blue). C,D: Third return sleep onset maps for $k = 0.4663$ (C) and $k = 0.434$ (D). For this range of k values the stable solution alternates between one and two sleep episodes per circadian cycle ($\rho = \frac{2}{3}$). The map has three branches (modulo 1) with a saddle-node bifurcation occurring at the right branch end at $k = 0.4663$ (C) and a border collision occurring at the left branch end at $k = 0.434$ (D). E,F: The second return sleep onset maps for $k = 0.403$ (E) and $k = 0.317$ (F) between which exists the stable solution with two sleep episodes per circadian cycle. The map has two branches (modulo 1) with a saddle-node bifurcation occurring at the right branch end at $k = 0.403$ (E) and a border collision occurring at the left branch end at $k = 0.317$ (F).

3.3.2 Varying the circadian waveform

The circadian waveform reflects the time-varying profile of the firing rate of the SCN population. The properties of the SCN waveform are determined by interindividual differences, the Earth's latitude as well as environmental light schedules that change with the seasons [157]. To investigate the effect of this waveform on the stable sleep-wake patterns, we varied the firing rate profile of the SCN population and tracked the existence of tangent intersections between model trajectories and the curves of saddle-node points of the $Z-$shaped surface.

Specifically, we modulated the circadian waveform such that its "steepness" (the transition region between low and high values of the SCN firing rate) varies without affecting the amplitude of the waveform. This is achieved by allowing the parameter α_{SCN} in the steady state response function of the SCN firing rate (Eq. 2.6) to vary from its default value $\alpha_{SCN} = 0.7$ (Table 2.1). We consider $\alpha_{SCN} \in (0, 3]$. Decreasing or increasing α_{SCN} results in longer or shorter intervals, respectively, of high SCN firing rate activity (Figure 3.3A) consistent with the response of SCN activity to longer or shorter environmental light periods [117, 157].

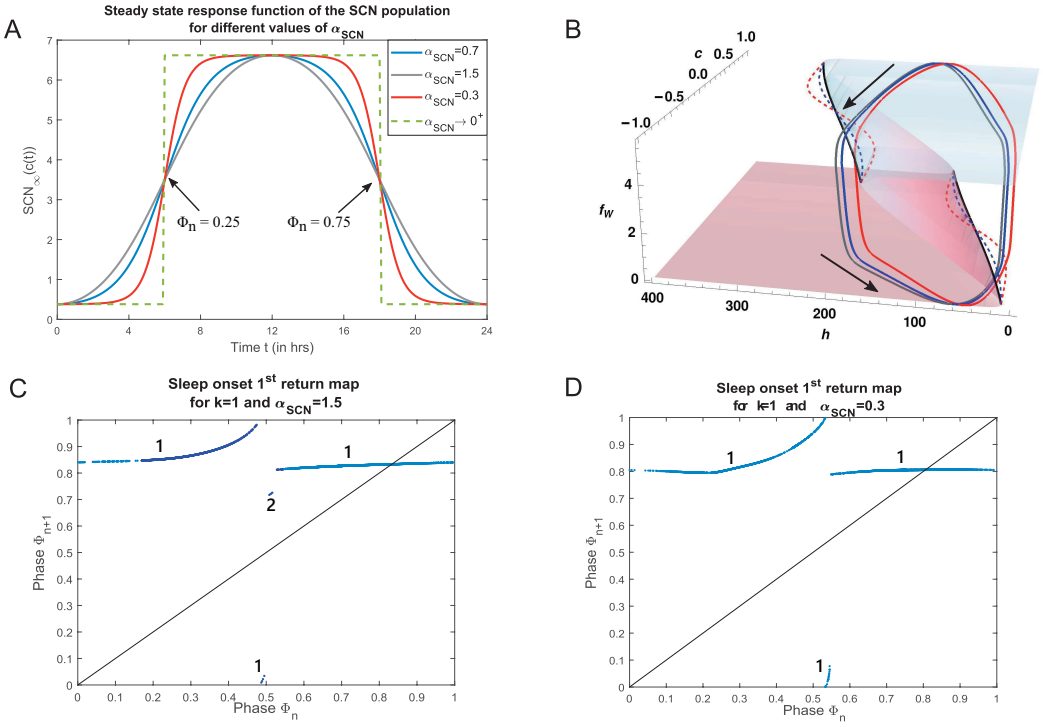

Figure 3.3: Effect of the parameter α_{SCN} on the circadian waveform, fast-slow decomposition surfaces and first return circle maps. A: Profile of $SCN_\infty(c(t))$ over 24 h for α_{SCN}=0.7 (default value, blue), α_{SCN}=1.5 (gray), α_{SCN}=0.3 (red) and the limiting case $\alpha_{SCN} \to 0^+$ (dashed green). B: The $Z-$shaped surface of steady state solutions of the model fast subsystem showing the variation in the curve of saddle-node points with α_{SCN} ($\alpha_{SCN} = 1.5$ (black), 0.7 (dashed blue) and 0.3 (dashed red)) with stable trajectories for $k = 1$ ($\alpha_{SCN} = 1.5$ (gray), 0.7 (blue) and 0.3 (red)). C,D: First return sleep onset circle maps for $k = 1$ and $\alpha_{SCN} = 1.5$(C) and 0.3(D). Distinct branches of the circle maps are labelled by the number 1 and 2 as needed.

To illustrate the effects of changing the profile of the $SCN_\infty(c(t))$ function on solutions with $k = 1$, we consider sleep onset maps and fast-slow decomposition for representative α_{SCN} values, $\alpha_{SCN} = 0.3$ and 1.5 (Figure 3.3B-D). In the $Z-$shaped surface, the curves of saddle-node points have smaller (larger) curvature for larger (smaller) values of α_{SCN}. Stable trajectories trace out similar hysteresis loops over the $Z-$surface. In addition, the sleep onset first return maps have the same general shape as the default case, displaying a similar discontinuity with an infinite slope on its left side. The fixed points also occur at similar phases for α_{SCN} equal to 0.3, 0.7 and 1.5: namely $(\Phi_n, \Phi_{n+1}) = (0.8057, 0.8057)$, $(0.8242, 0.8242)$, and $(0.833, 0.833)$,

respectively.

The map for $\alpha_{SCN} = 1.5$ exhibits a second discontinuity resulting in a small map branch near $\Phi_n = 0.5$ (Figure 3.3C). This discontinuity is caused by tangent intersections for trajectories associated with Φ_n values near 0.5: one initial phase produces a trajectory that makes a tangent intersection with the lower saddle-node curve, and a slightly higher initial phase produces the trajectory that makes a tangent intersection with the upper saddle-node curve.

3.3.3 Varying both homeostatic time constants and circadian waveform

We study the combined effect of the parameter $\alpha_{SCN} \in (0, 3]$ on the stable sleep-wake patterns obtained and bifurcation sequences arising as the homeostatic sleep drive time constants are scaled by k. To that end, we first consider the stable, phase-locked solutions obtained as k is decreased for representative α_{SCN} values greater ($\alpha_{SCN} = 1.5$) and less ($\alpha_{SCN} = 0.3$) than the default value ($\alpha_{SCN} = 0.7$). We initially analyze the α_{SCN} effect on the bifurcation sequence for the loss of stability of the $\rho = 1$ solution. Next, we compute the (k, α_{SCN}) two-parameter bifurcation diagram to illustrate the evolution of bifurcation sequences over ranges of k and α_{SCN} values.

As we describe below, for lower values of α_{SCN}, numerical simulations detect many fewer stable solutions associated with rotation numbers $\rho \in [\frac{1}{2}, 1]$. To verify this trend for the lowest values of α_{SCN}, we additionally consider the limiting case of $\alpha_{SCN} \to 0^+$ corresponding to the SCN firing rate changing as a step function (see Section 3.4).

3.3.3.1 Stable solutions for shallow and steep circadian waveforms (i.e., α_{SCN} =1.5 and 0.3)

One key effect of changing the circadian waveform is that as k is decreased from 1, the $\rho = 1$ solution corresponding to one sleep episode per circadian cycle loses stability earlier for larger values of α_{SCN} (shallower waveforms) (Figure 3.4). For

example, the $\rho = 1$ solution loses stability at $k = 0.556$, $k = 0.503$, and $k = 0.455$ for $\alpha_{SCN} = 1.5, 0.7$ and 0.3, respectively. As discussed above, the creation of tangencies of trajectories with the upper saddle-node curves of the $Z-$shaped surface is important in order for bifurcations to occur. Both parameters k and α_{SCN} influence the creation of such tangent trajectories since the latter dictates the shape of the saddle-node curve and together they determine the angle at which a trajectory approaches it. As the upper saddle-node curve becomes steeper (for lower values of α_{SCN}), h must evolve faster for a trajectory orbit (stable or unstable) to become tangent to it, thus leading to the lower k values when the $\rho = 1$ solution loses stability.

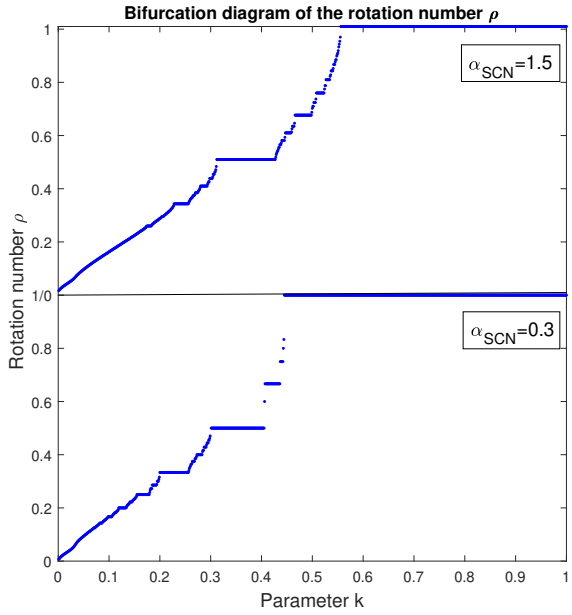

Figure 3.4: Comparison of the bifurcation diagrams of the rotation number ρ for $\alpha_{SCN} = 1.5$ (top) and $\alpha_{SCN} = 0.3$ (bottom). Using a numerical approach to construct these diagrams, we obtained more types of periodic solutions with $\rho \in [\frac{1}{2}, 1]$ for larger α_{SCN} (shallower circadian waveform) compared to the solutions for smaller α_{SCN} (steeper circadian waveform).

Additionally, for larger values of α_{SCN}, numerical simulations detect more stable solutions (than in the default $\alpha_{SCN} = 0.7$ case) corresponding to distinct values of the rotation number, particularly types of $\rho = \frac{q}{p}$ periodic solutions within the intervals between $\rho = \frac{1}{p}$ periodic solutions (Figures 3.4 (top) and 3.1B). Conversely, for smaller

α_{SCN} values, a winnowing (i.e., shrinking of the k-distance) of stable solutions with $\rho \in [\frac{1}{2}, 1]$ is observed (Figure 3.4 (bottom)). While the arithmetic precision and the step size of the parameter k in our numerical simulations could account for the inability to detect more solutions, we can conclude that stable solutions in this ρ range exist over shorter k intervals.

3.3.3.2 Bifurcations sequences for $\rho = 1$ solutions for representative α_{SCN} values

Border collision $\rightarrow$ saddle-node

To understand the bifurcation leading to the loss of stability of the $\rho = 1$ solution as k decreases when α_{SCN}=1.5, Figure 3.5A displays the evolution of the stable periodic orbits for various values of k ranging from $k = 1$ to $k = 0.556$, the k value just before the loss of stability of the $\rho = 1$ solution. As suggested by the absence of a tangent intersection of the trajectory with the saddle-node curve, the sleep-onset map demonstrates a saddle-node bifurcation near the right side of the discontinuity for the bifurcation value of k=0.556 (Figure 3.5B). The unstable fixed point associated with the saddle-node bifurcation was created at a higher value of k ($k = 0.56$) in a border collision bifurcation on the map branch on the right side of the discontinuity. The associated unstable orbit makes a tangent intersection with the upper curve of saddle-node points of the $Z-$shaped surface. Similarly to the default $\alpha_{SCN} = 0.7$ case, the $\rho = 1$ solution for $\alpha_{SCN} > 0.7$ loses stability in the bifurcation sequence of BC-U $\rightarrow$ SN as k is decreased.

Border collision

For $\alpha_{SCN} = 0.3$, we observe a different bifurcation sequence when the $\rho = 1$ solution loses stability at $k = 0.445$. At this bifurcation point, the associated sleep-onset map continues to show two discontinuities as observed for the map for $k = 1$. The map

demonstrates that the bifurcation occurs due to a border collision on the right side of the discontinuity (Figure 3.5D). This border collision corresponds to the stable trajectory (Figure 3.5C, blue curve) creating a tangency at the upper saddle-node curve of the $Z-$shaped surface (Figure 3.5C). This suggests that for smaller α_{SCN} values, the $\rho = 1$ solution ceases to exist due to a BC-S bifurcation.

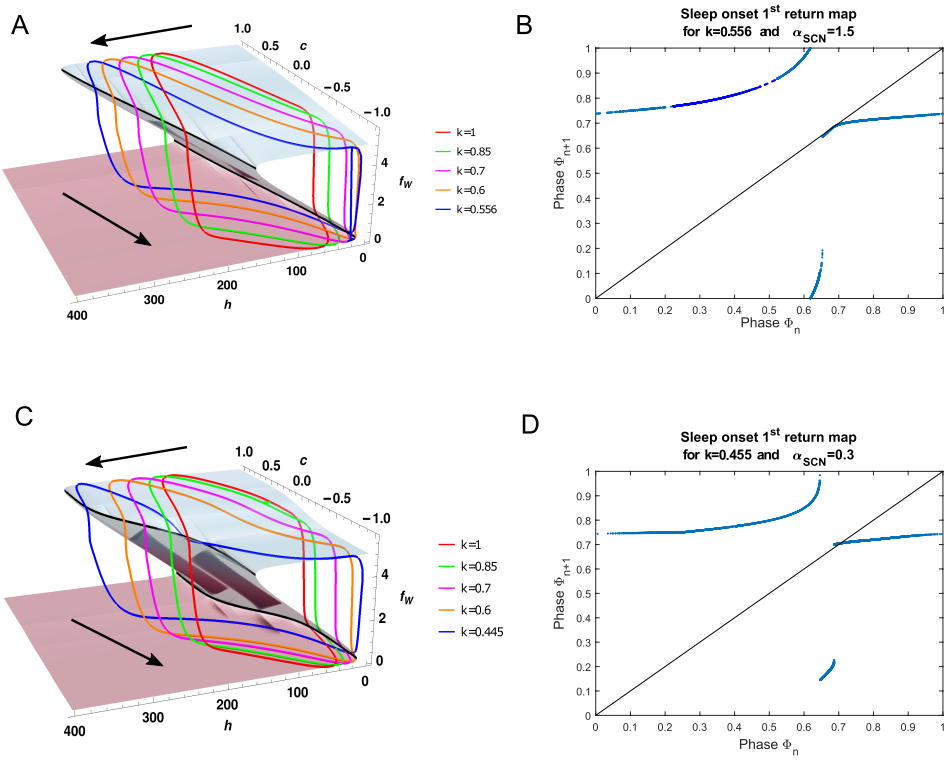

Figure 3.5: Bifurcations at the loss of stability of the $\rho = 1$ solution for representative large (A,B) and small (C,D) α_{SCN} values. A: Stable trajectories for $\alpha_{SCN} = 1.5$ and $k = 1$ (red), $k = 0.8$ (green), $k = 0.6$ (orange) and $k = 0.556$ (blue). B: First return sleep onset map for $\alpha_{SCN} = 1.5$ and $k = 0.556$ indicates the loss of stability of the $\rho = 1$ solution occurs due to a saddle-node bifurcation. C: Stable trajectories for $\alpha_{SCN} = 0.3$ and $k = 1$ (red), $k = 0.8$ (green), $k = 0.6$ (magenta), $k = 0.55$ (orange) and $k = 0.506$ (blue). D: First return map for $\alpha_{SCN} = 0.3$ and $k = 0.445$ indicates the $\rho = 1$ solution loses stability due to a border collision bifurcation.

3.3.3.3 Bifurcation sequences in (k, α_{SCN}) parameter space

To illustrate the evolution of bifurcation sequences over a range of homeostatic time constants and circadian waveforms, we constructed a two-parameter bifurcation diagram with respect to k and α_{SCN} (Figure 3.6). The $\rho = 1$ entrainment region (cyan) is bordered on the left by a curve of (k, α_{SCN}) values associated with stable fixed points at which a saddle-node bifurcation (dashed black) or a border collision (solid red) occurs.

The transition from the regime where the stable $\rho = 1$ solution is lost due to the BC-U $\rightarrow$ SN bifurcation sequence to the regime where it is lost due to a BC-S bifurcation occurs continuously as α_{SCN} decreases. In the BC-U$\rightarrow$SN regime, at the k value associated with the border collision the slope of the map at the created fixed point is greater than 1 (but finite) resulting in an unstable fixed point. As α_{SCN} decreases, the slope of the map curve at the unstable fixed point created in this bifurcation also decreases.

The two regimes are separated at $(k, \alpha_{SCN}) = (0.486, 0.6)$ which is marked with a diamond. At this point, the curve of stable fixed points (solid red) merges with the curve of unstable fixed points (solid yellow). For $\alpha_{SCN} > 0.6$, the unstable fixed points are created in a border collision bifurcation occurring at a higher k value than the k value associated with the saddle-node bifurcation that forms the boundary of the $\rho = 1$ entrainment region. The transition between bifurcation regimes occurs at $(k, \alpha_{SCN}) = (0.486, 0.6)$. Here, the fixed point of the map coincides with the end point (border) of the map curve, and the slope of the map curve at that point is equal to 1. For $\alpha_{SCN} < 0.6$, the stable fixed point associated with the $\rho = 1$ solution is lost directly due to a border collision bifurcation.

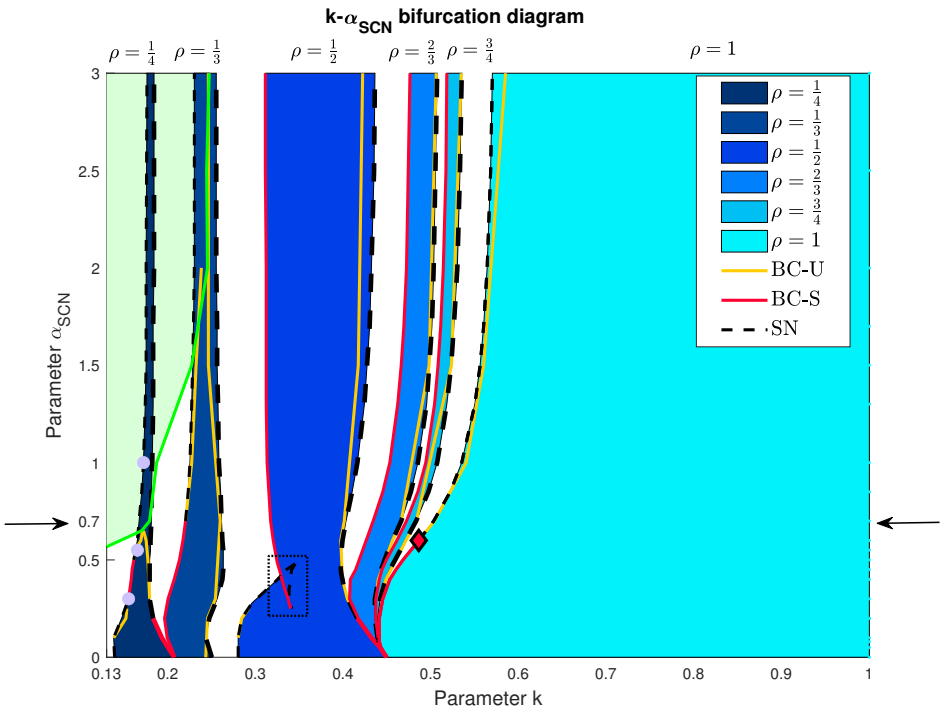

Figure 3.6: Two parameter bifurcation diagram with respect to k and α_{SCN}. The resolution of the diagram is not uniform, with the modes in $alpha_{SCN}$ and k step sizes being 0.02 and 0.002, respectively. Colored areas indicate parameter regions (or tongues) where the following stable, phase-locked solutions exist (from left to right): $\rho = \frac{1}{4}, \frac{1}{3}, \frac{1}{2}, \frac{2}{3}, \frac{3}{4}, 1$. Line type indicates bifurcation type: saddle-node (dashed black), border collision of a stable fixed point (solid red), border collision of an unstable fixed point (solid yellow). Diamond indicates transition between bifurcation sequences governing loss of stability of the $\rho = 1$ solution (see Figure 3.5). Arrows indicate the default α_{SCN} value of 0.7. The green line is the set of (k, α_{SCN}) points that forms the boundary between regions where maps are discontinuous and continuous, and the light green shaded region indicates the (k, α_{SCN}) values for which the map is continuous. The black dotted rectangle indicates a zoomed in version of the two-parameter bifurcation diagram shown in Figure 3.7. The three light purple bullets indicate the (k, α_{SCN}) values of the maps shown in Figure 3.8.

The two parameter bifurcation diagram of Figure 3.6 also shows the entrainment regions (or tongues) in (k, α_{SCN}) space for stable solutions with $\rho = \frac{3}{4}, \frac{2}{3}$ and $\frac{1}{2}$. For $\alpha_{SCN} \geq 0.2$, each of these solutions gains stability, as k is decreased, through a saddle-node bifurcation (dashed black curve) that is followed by a border collision (solid yellow curve) that eliminates an unstable fixed point. For the $\rho = \frac{3}{4}, \frac{2}{3}$ solutions as k is further decreased, stability is lost through a border collision (solid red curve)

resulting in the bifurcation sequence SN $\rightarrow$ BC-U $\rightarrow$ BC-S, similar to the bifurcation sequence observed for these solutions for the default $\alpha_{SCN} = 0.7$.

While not computed explicitly, we argue that this bifurcation sequence delimits the entrainment regions of all solutions with $\rho \in (\frac{1}{2}, 1)$ and $\alpha_{SCN} \geq 0.2$. Specifically, for a stable solution with rotation number $\rho = \frac{q}{p}$ we consider the p^{th} order return map. As explained in Appendix A, the p^{th} order map retains similar structure as the first return map. For example, for values of (k, α_{SCN}) where the first return map is discontinuous, the p^{th} return map is likewise discontinuous. Furthermore, the p^{th} return map has p discontinuities corresponding to each discontinuity in the first return map. For $\alpha_{SCN} \geq 0.2$ and all the k values where solutions with these ρ values exist, first return maps display an infinite slope at the left of a discontinuity and a finite slope on the right. The p^{th} return map similarly shows this structure in each of the branches of the map. Computing maps at the k values where these solutions gain and lose stability reveals that stable fixed points are created on map branches to the left of a discontinuity and are lost on map branches to the right of a discontinuity. Specifically, for fixed α_{SCN}, we consider the p^{th} return map at the highest value of k for which $\rho = \frac{q}{p}$ exists. On the p branches associated with this map, there are p saddle-node points formed by the infinite slope end of the map branches. As k is decreased, p unstable fixed points are eliminated in a border collision bifurcation on the infinite slope ends of the p map branches. As k is decreased further, the p stable fixed points for the $\rho = \frac{q}{p}$ solution disappear in a border collision bifurcation at the finite slope end of the p map branches. Since, for decreasing k, the bifurcation sequence SN $\rightarrow$ BC-U $\rightarrow$ BC-S is predicted by the structure of the map, we expect that all solutions with $\rho \in (\frac{1}{2}, 1]$ and $\alpha_{SCN} \geq 0.2$ will show a similar bifurcation sequence.

The bifurcations bounding the $\rho = \frac{1}{2}$ entrainment region are the same for $\alpha_{SCN} > 0.42$. However, the bifurcation governing the loss of stability of the $\rho = \frac{1}{2}$ solution changes to a saddle-node for $\alpha_{SCN} < 0.42$ (Figure 3.6). This exchange in

the bifurcations is a result of a small region or "island" of bistability emerging in the interior of the $\rho = \frac{1}{2}$ entrainment tongue (Figure 3.7E). The "bistability island" exists for $\alpha_{SCN} \in [0.25, 0.48]$. It is bounded by curves of saddle-node bifurcations for high k values while for lower k, it is bounded by a saddle-node curve for $\alpha_{SCN} \in (0.42, 0.48)$ and a curve of border collisions for $\alpha_{SCN} \in [0.25, 0.42)$. As described below, at $\alpha_{SCN} = 0.42$, both bifurcations occur at the same value of k, enabling the switch in bifurcation type eliminating the stable $\rho = \frac{1}{2}$ solution.

The region of bistability occurs due to the curves of the second return map becoming S-shaped which allows for multiple intersections with the diagonal $\Phi_{n+2} = \Phi_n$, and thus multiple fixed points. Specifically, in this α_{SCN} interval, as k decreases within the $\rho = \frac{1}{2}$ entrainment interval, the second pair of stable fixed points (and a pair of unstable fixed points) are created in the second return map due to a saddle-node bifurcation at the lower knees of the S-shaped map curves (Figure 3.7C, figure shows one of the map branches). On the map branch shown in Figure 3.7C, the original $\rho = \frac{1}{2}$ solution corresponds to the stable fixed point at higher sleep onset phase and the newly created solution with the stable fixed point at lower sleep onset phase. The newly created unstable solution has a sleep onset phase between those of the stable fixed points. For $\alpha_{SCN} \in (0.42, 0.48]$, as k decreases further, the new unstable fixed points and the original stable fixed points approach each other and eventually collide in a saddle-node bifurcation at the upper knees of the S-shaped map curves (Figure 3.7B). This bifurcation marks the end of the interval of bistability and the newly created stable fixed points remain. These fixed points are eliminated, and the $\rho = \frac{1}{2}$ solution loses stability, in a border collision at the left ends of the map branches (Figure 3.7A). Thus, the complete bifurcation sequence for $\alpha_{SCN} \in (0.42, 0.48]$ is

$$\text{SN} \rightarrow \text{BC-U} \rightarrow \text{SN} \rightarrow \text{SN} \rightarrow \text{BC-S}.$$

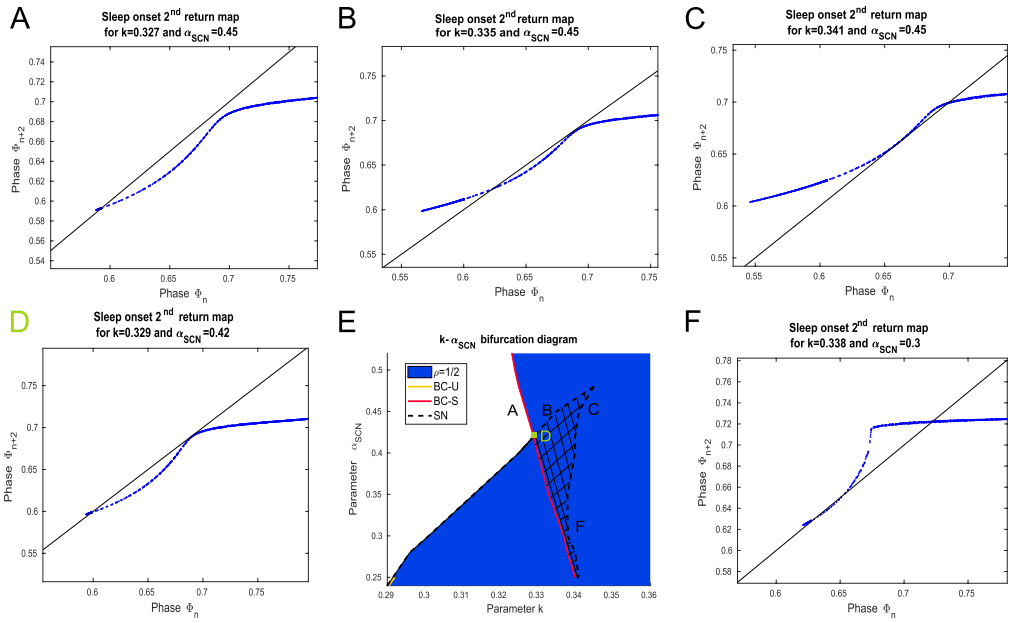

Figure 3.7: Bifurcations creating a bistability island in the $\rho = \frac{1}{2}$ stable entrainment region. A-C: Evolution of the second return map for $\alpha_{SCN} = 0.45$. Here only one branch of the map is shown. For $k = 0.341$ (C) a saddle-node bifurcation occurs at the lower part of the map curve. This gives birth to a new pair of stable and unstable fixed points. At $k = 0.335$ (B) another saddle-node bifurcation leads to the collision of the new unstable and original stable fixed points. Complete loss of stability of the $\rho = \frac{1}{2}$ solution occurs at $k = 0.327$ (A) in a border collision. D: At $\alpha_{SCN} = 0.42$, the loss of bistability coincides with the loss of stability of the $\rho = \frac{1}{2}$ solution. At $k = 0.329$ a saddle-node and a border collision eliminate two stable and one unstable fixed points. E: Close up of the two-parameter bifurcation diagram in (k, α_{SCN}) space shown in Figure 3.6 shows the bistability island within the $\rho = \frac{1}{2}$ stable entrainment region. Letters in panel E correspond to maps shown in panels A-D and F. F: Second return map curve showing a "sharp cornered S" shape for $\alpha_{SCN} = 0.3$ and $k = 0.338$ where a saddle-node bifurcation initiates the interval of bistability.

At $\alpha_{SCN} = 0.42$, the end of the bistability interval coincides with the loss of stability of the $\rho = \frac{1}{2}$ solution as the saddle-node bifurcation at the upper knees of the S-shaped map curves occurs at the same k value as the border collision at the left ends of the map branches (Figure 3.7D, $k = 0.329$). At this value of k, the two pairs of stable fixed points (one on each map branch of the second return map) lose stability simultaneously. The fixed points corresponding to the original stable solution that initiated the $\rho = \frac{1}{2}$ tongue (at higher sleep onset phase in Figure 3.7D) lose stability due to a saddle-node bifurcation with the unstable fixed points. The other stable fixed points (at lower sleep onset phase in Figure 3.7D)lose stability due to a border collision. This causes the exchange of the bifurcation dictating the loss of stability of the $\rho = \frac{1}{2}$ solution from a border collision to a saddle node. Thus at $\alpha_{SCN} = 0.42$ the full bifurcation sequence is

$$\text{SN} \rightarrow \text{BC-U} \rightarrow \text{SN} \rightarrow \text{BC-S} + \text{SN}.$$

For $\alpha_{SCN} \in [0.25, 0.42)$, the shape of the map branches in the second return map transitions to a "sharp cornered S" (Figure 3.7F). When the map is continuous in this sharp cornered S shape, the following bifurcation sequence takes place

$$\text{SN} \rightarrow \text{BC-U} \rightarrow \text{SN} \rightarrow \text{BC-S} \rightarrow \text{SN}.$$

Here, the stable fixed points that introduced bistability (at lower phase in the figure) lose stability first in a border collision at the left end of the map curves. For lower k values, the unstable and original stable fixed points collide in a saddle-node bifurcation which eliminates the stable $\rho = \frac{1}{2}$ solution.

As α_{SCN} approaches 0.25, a discontinuity can occur in the map in this sharp cornered S shape, where the slope of the map branches are infinite from the left and

finite from the right. In this case, the complete bifurcation sequence is

$$\text{SN} \rightarrow \text{BC-U} \rightarrow \text{SN} \rightarrow \text{BC-S} \rightarrow \text{BC-U} \rightarrow \text{SN}.$$

The last border collision bifurcation creates another pair of unstable fixed points (one on each of the associated branches of the second return map), as the sharp cornered S shape of the map curves starts deforming as k is decreased.

3.3.4 Bifurcation sequences for small k

As noted previously, for small values of k, the homeostatic sleep drive varies more quickly relative to the SCN firing rate especially for high values of α_{SCN}, thereby making tangent intersections of the solution trajectory with the curve of saddle-node points on the $Z-$surface less likely. As a result, the associated sleep onset maps can be continuous. This affects the bifurcation sequence delimiting stability of solutions with rotation numbers $\rho \leq \frac{1}{3}$. The two parameter bifurcation diagram can be separated into regimes associated with continuous or discontinuous sleep onset maps. There exists a curve of (k, α_{SCN}) points (Figure 3.6, solid green curve) above which the map is continuous (Figure 3.6, light green area). We will refer to this (green) curve as the transition zone.

We note that bifurcation sequences closer to the continuous regime, and hence across the transition zone, may not involve border collision bifurcations associated with the creation or destruction of stable fixed points (BC-S). As the maps obtain larger discontinuities, we observe bifurcation sequences similar to the ones delimiting the entrainment regions we have encountered so far. We describe representative examples of the bifurcations across the transition zone with the $\rho = \frac{1}{4}$ solutions for different values of α_{SCN}.

Saddle-node → saddle-node

For pairs of (k, α_{SCN}) values above the transition zone (see light green area), the first and fourth return sleep onset maps are continuous, and hence saddle-node bifurcations lead to loss of stability of the $\rho = \frac{1}{4}$ periodic solution (Figure 3.8A). The fourth return map has four pairs of stable and unstable fixed points, and the unstable fixed points remain over the k interval where the solution is stable, i.e. the unstable fixed point is not lost through a border collision. Thus, the stability of the $\rho = \frac{1}{4}$ periodic solution in this regime occurs in the bifurcation sequence

$$\text{SN} \rightarrow \text{SN}.$$

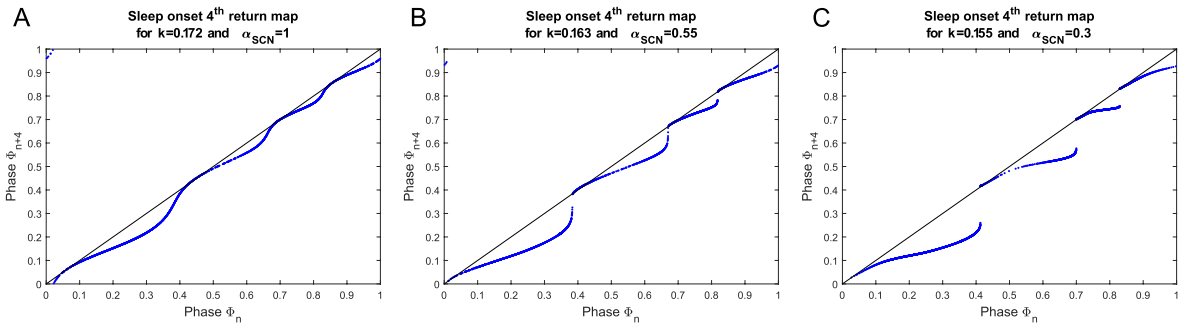

Figure 3.8: Transition from a continuous to a discontinuous sleep onset map within the $\rho = \frac{1}{4}$ entrainment region. Fourth return sleep onset maps are shown at smallest k values where the $\rho = \frac{1}{4}$ solution is stable for different α_{SCN} values. A: For $\alpha_{SCN} = 1$ the map is continuous and loss of the stable $\rho = \frac{1}{4}$ solution is due to a saddle-node bifurcation. B: For $\alpha_{SCN} = 0.55$ the map is discontinuous, but the slope of the map branches on the right of each discontinuity is greater than 1 in magnitude, leading to a border collision that generates an unstable fixed point followed by a saddle-node bifurcation as k decreases. C: For $\alpha_{SCN} = 0.3$ the map is discontinuous. A border collision on the right of each discontinuity leads to loss of the stable fixed points associated with the $\rho = \frac{1}{4}$ solution.

Saddle-node → border collision → border collision [→ saddle-node]

For (k, α_{SCN}) pairs below the transition zone, the first and fourth return maps are discontinuous with infinite slopes to the left of the discontinuity and finite slopes to

the right of the discontinuity. A saddle-node bifurcation leads to gain of stability of the $\rho = \frac{1}{4}$ periodic solution as k is decreased. This is followed by a border collision bifurcation at a slightly lower value of k.

For larger α_{SCN} values, right below the transition zone, the slope of the discontinuous map is greater than 1 at the right of the discontinuity (Figure 3.8B). Therefore, for decreasing k there is first a border collision bifurcation that generates an unstable fixed point, and then this unstable fixed point eventually collides with the stable fixed point in a saddle-node bifurcation as k decreases. Thus, stability of the $\rho = \frac{1}{4}$ solution in this regime occurs in the bifurcation sequence of

$$\text{SN} \rightarrow \text{BC-U} \rightarrow \text{BC-U} \rightarrow \text{SN}.$$

As α_{SCN} is reduced, the slope of the map decreases smoothly to values less than 1. Then the stable fixed point ceases to exist due to a border collision bifurcation as k decreases. In particular, the full bifurcation sequence is SN $\rightarrow$ BC-U $\rightarrow$ BC-S.

Transitions between these bifurcation sequences occurred smoothly. Specifically, for the $\rho = \frac{1}{4}$ solution at the transition zone, the unstable fixed points associated with the border collisions appear at the same k value and their k values diverge for smaller α_{SCN}. Additionally, for the $\rho = \frac{1}{4}$ and $\frac{1}{3}$ solutions, as the bifurcation at the loss of stability as k decreases changes, the k values at the border collisions associated with the creation of unstable fixed points (solid yellow curve) merges with the values associated with the destruction of the stable fixed points (solid red curve) as α_{SCN} decreases, as we have observed with solutions of $\rho > \frac{1}{3}$. We expect that similar bifurcation sequences delimit other stable solutions with $\rho < \frac{1}{3}$ across the transition zone, as the associated maps are expected to maintain a similar structure.

3.4 Circadian Hard-Switch model in limit $\alpha_{SCN} \to 0^+$

As shown in the k-α_{SCN} bifurcation diagram (Figure 3.6), as α_{SCN} decreases, the widths of the k intervals associated with each stable entrainment regime change in the following way: For some rotation numbers, such as $\rho = 1, \frac{1}{2}$, and $\frac{1}{4}$, the k intervals expand for low α_{SCN} values, while for $\rho = \frac{3}{4}$, $\frac{2}{3}$ and $\frac{1}{3}$, the k intervals contract. In the limit $\alpha_{SCN} \to 0^+$, this leads to the loss of stable solutions with $\rho \in (\frac{1}{2}, 1)$ and $\rho \in (\frac{1}{4}, \frac{1}{3})$, and a change in the bifurcation sequence bordering the $\rho = \frac{1}{2}$ and $\rho = \frac{1}{4}$ stable solutions. To analyze this change in the size of k-intervals for a small α_{SCN}, we consider the model in the limit $\alpha_{SCN} \to 0^+$. We refer to this model as the circadian hard switch (CHS) model.

In this section, we first formally define the CHS model and then describe the stable solutions obtained as k decreases from 1 with a particular focus on the bifurcations delimiting the stable $\rho = \frac{1}{2}, \frac{1}{3}$ and $\frac{1}{4}$ solutions. Based on how the $\rho = 1$ (and $\rho = \frac{1}{3}$) solutions directly transition to the $\rho = \frac{1}{2}$ (and $\rho = \frac{1}{4}$) solutions in the CHS model, allows us to explain why the k intervals for stable solutions with $\rho \in (\frac{1}{2}, 1)$ (and $\rho \in (\frac{1}{4}, \frac{1}{3})$) shrink for small α_{SCN}.

3.4.1 Definition of the Filippov system with two switching boundaries

In the limit as $\alpha_{SCN} \to 0^+$, the firing rate response function of the SCN population can be approximated by a step function. This introduces a second discontinuity in the f_{SCN} derivative, when c crosses β_{SCN}:

$$\frac{df_{SCN}}{dt} = \frac{SCN_{max} \cdot 0.5 \cdot \left(1 + \tanh\left(\frac{1}{0.7}\right)(2\mathscr{H}(c - \beta_{SCN}) - 1)\right) - f_{SCN}}{\tau_{SCN}}, \tag{3.1}$$

where $\mathscr{H}$ is the Heaviside function. Then, our model becomes a Filippov system

with two switching boundaries [62]: one represents the switch between sleep and wake, and the other represents a switch between high and low activity in the circadian drive $c(t)$ as occurs in SCN firing rate over the 24 hour day [157].

To define the circadian hard switch (CHS) model, we introduce the new switching boundary Σ in addition to the original switching boundary Γ where Σ is defined as: $\Sigma = \{c = \beta_{SCN}\}$, where $\beta_{SCN} = 0$ (Figure 3.9A).
The regions lying on either side of each boundary are then defined as:

- $\Sigma^+ = \{c > \beta_{SCN}\}$ and $\Sigma^- = \{c < \beta_{SCN}\}$,
- $\Gamma^+ = \{f_W > \theta_W\}$ and $\Gamma^- = \{f_W < \theta_W\}$.

These boundaries divide the domain of the model into the following four subregions:

1. $\Sigma^+ \cap \Gamma^+ = \{c > \beta_{SCN}$ and $f_W > \theta_W\}$ (wake state with increasing h and high f_{SCN}),
2. $\Sigma^- \cap \Gamma^+ = \{c < \beta_{SCN}$ and $f_W > \theta_W\}$ (wake state with increasing h and low f_{SCN}),
3. $\Sigma^- \cap \Gamma^- = \{c < \beta_{SCN}$ and $f_W < \theta_W\}$ (sleep state with decreasing h and low f_{SCN}),
4. $\Sigma^+ \cap \Gamma^- = \{c > \beta_{SCN}$ and $f_W < \theta_W\}$ (sleep state with decreasing h and high f_{SCN}).

In each of these subregions, the model has smooth dynamics dictated by subsets of Equations (2.1) - (2.10), while on the boundaries Σ and Γ one way to define the dynamics is Filippov's convex method. In Appendix C, we show that the model flow is transversal across the boundaries of these four subregions and thus, a solution of this piecewise smooth system can be concatenated from trajectories in its four subregions.

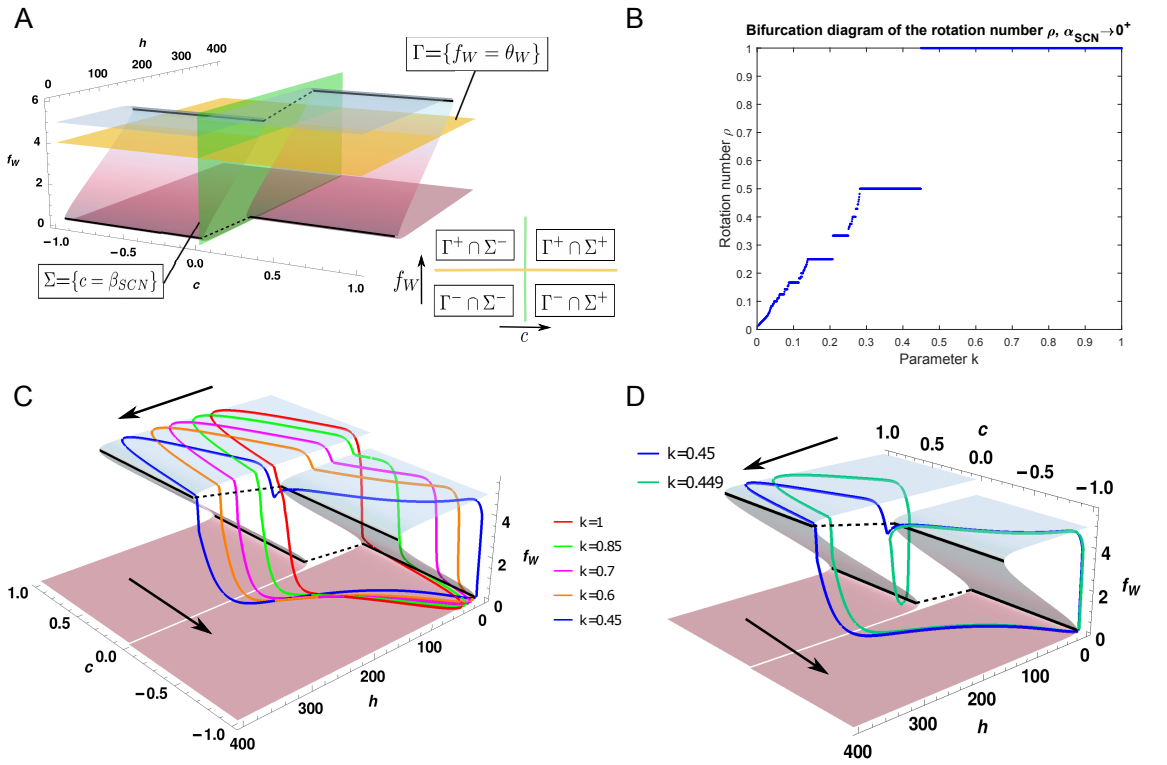

Figure 3.9: Dynamics and bifurcation structure in the circadian hard switch (CHS) model. A: The CHS model is a Filippov system with two boundaries, Γ (yellow plane) and Σ (green plane). Therefore, in the $c-h-f_W$ space we can visualize the fast-slow surface being divided into four regions, $\Gamma^+\cap\Sigma^+$, $\Gamma^+\cap\Sigma^-$, $\Gamma^-\cap\Sigma^-$ and $\Gamma^-\cap\Sigma^+$. We have plotted the individual fast-slow surfaces for the dynamical system when $c>\beta_{SCN}$ (corresponds to Σ^+) and $c<\beta_{SCN}$ (corresponds to Σ^-). In each of these regions, the system is smooth, but a discontinuity in the derivative occurs as the system crosses a boundary. B: The bifurcation diagram of the rotation number ρ for the CHS model. C: The evolution of the stable solutions leading to the loss of stability of the $\rho=1$ solution. In this regime, a sleep onset always occurs at the same circadian phase when the trajectory crosses the boundary Σ. D: Decreasing the value of the scaling parameter k leads to loss of stability of the $\rho=1$ solution and emergence of the stable $\rho=\frac{1}{2}$ solution.

3.4.2 Bifurcations in the CHS model

Using a numerical algorithm by Calvo et al. [33] to integrate the CHS model, we numerically computed the bifurcation diagram of the rotation number ρ for $k\in(0,1]$ (Figure 3.9B). The bifurcation diagram maintains a period-adding-like structure, as well as similar trends to those observed for small α_{SCN} values. As k was decreased

from 1, the $\rho = 1$ solution in the CHS model lost stability at $k = 0.45$, a similar value as found for $\alpha_{SCN} = 0.3$. As suggested by the shrinking of k intervals for solutions with $\rho \in (\frac{1}{2}, 1)$ for small α_{SCN}, the next stable solution detected as k was decreased was $\rho = \frac{1}{2}$. Specifically, we did not detect any intermediate $\rho = \frac{q}{p}$ solutions between the $\rho = 1$ and $\rho = \frac{1}{2}$ solutions in the CHS model. As k decreased further, there were fewer stable solutions between the $\rho = \frac{1}{2}$ and $\rho = \frac{1}{3}$ solutions in the CHS model than for solutions associated with larger α_{SCN} values. Between the $\rho = \frac{1}{3}$ and $\rho = \frac{1}{4}$ solutions, no intermediate solutions were detected in the CHS model.

Below, we explain why we detect many or few types of intermediate solutions between certain ρ values using the fast-slow surface associated with the CHS model.

Winnowing of entrainment regions

In the CHS model, the smoothly varying Z-shaped surface associated with continuous $c(t)$ is split into two connected Z-shaped surfaces corresponding to the positive and negative $c(t)$ of the CHS model. By considering model trajectories on this double $Z-$shaped surface, we identify a change in the bifurcation sequence delimiting the $\rho = \frac{1}{2}$ and $\rho = \frac{1}{4}$ stable solutions. We note that the switching boundary Σ constrains sleep onset phases for stable $\rho = 1$ solutions. Namely, as k is decreased from 1, sleep onset phases remain at $\Phi = 0.75$ due to trajectories falling off the upper wake manifold of the $Z-$shaped surface at Σ during decreasing circadian drive $c(t)$ (Figure 3.9C). At $k = 0.45$ where the $\rho = 1$ solution loses stability, the trajectory additionally approaches Σ during increasing circadian drive at h values where a transition off the upper manifold is possible (Figure 3.9D). For slightly smaller $k = 0.449$, the $\rho = \frac{1}{2}$ solution gains stability in a border collision bifurcation due to sleep onsets occurring at Σ for $\Phi = 0.25$ and $\Phi = 0.75$.

The absence of solutions with $\rho \in (\frac{1}{2}, 1)$ is due to the trajectory intersecting Σ as $c(t)$ increases and falling off the upper wake manifold at every circadian cycle.

A stable solution with $\rho \in (\frac{1}{2}, 1)$ requires that sleep onset phases slightly shift on successive circadian cycles such that some cycles only have 1 sleep episode and some cycles have 2 sleep episodes. Here, since one sleep onset always occurs at $\Phi = 0.75$ and the trajectory during the sleep episode is similar even if the h value at sleep onset is different (Figure 3.9D), trajectories do not shift to avoid falling off the upper wake manifold at $\Phi = 0.25$ at the Σ boundary.

In contrast, stable solutions with $\rho \in (\frac{1}{3}, \frac{1}{2})$ were obtained. The existence of stable $\rho \in (\frac{1}{3}, \frac{1}{2})$ solutions can be understood by considering the sleep onset phases of the multiple sleep episodes in those solutions. When the $\rho = \frac{1}{2}$ solution loses stability at $k = 0.28$, sleep onsets occur near $\Phi \approx 0$ near the minimum of c and at $\Phi = 0.75$. Thus, the switching boundary Σ constrains the phase of only one of the sleep episodes. For k slightly smaller, i.e. h slightly faster, sleep onsets will occur at earlier phases. For the sleep onset occurring near $\Phi \approx 0$, the phase is not constrained by the boundary Σ and can shift such that a third sleep onset may occur in a circadian cycle resulting in a solution with $\rho \in (\frac{1}{3}, \frac{1}{2})$. The evolution of sleep onset phases and sleep patterns as the period-adding structure progresses with decreasing k introduces the beginning of the stable $\rho = \frac{1}{3}$ solution with sleep onset phases close to 0, smaller and larger than 0.75.

The $\rho = \frac{1}{3}$ solution loses stability in a border collision bifurcation and directly transitions to the stable $\rho = \frac{1}{4}$ solution similarly to the way in which the $\rho = 1$ solution transitions to the $\rho = \frac{1}{2}$ solution. At the loss of stability of the $\rho = \frac{1}{3}$ solution at $k = 0.208$, the three sleep onset phases occur near the extrema of the circadian drive (i.e. $\Phi \approx 0$ and $\Phi \approx 0.5$) and at $\Phi = 0.75$ at the Σ boundary with decreasing $c(t)$. For $k = 0.207$, the $\rho = \frac{1}{4}$ solution gains stability as a fourth sleep onset occurs at $\Phi = 0.25$ at the Σ boundary with increasing $c(t)$. The constraint that the trajectory always intersects Σ as $c(t)$ increases, causing the border collision, does not permit the slight shifting of sleep onset phases on successive circadian cycles necessary to result in a

solution with $\rho \in (\frac{1}{4}, \frac{1}{3})$. Instead, the trajectory falls off the upper wake manifold at $\Phi = 0.25$ on every circadian cycle resulting in the stable $\rho = \frac{1}{4}$ solution.

Understanding the small $\alpha_{SCN} > 0$ case

For small $\alpha_{SCN} > 0$, similar constraints on sleep onset phases near $\Phi = 0.75$ and 0.25 also explain the shrinking k intervals for stable solutions with $\rho \in (\frac{1}{2}, 1)$ and $\rho \in (\frac{1}{4}, \frac{1}{3})$. Sleep onset phases in these solutions have slightly different values on successive circadian cycles that can result in different numbers of sleep episodes per cycle. For small α_{SCN}, the steep f_{SCN} profile similarly constrains sleep onset phases to be near $\Phi = 0.75$ and $\Phi = 0.25$ as observed in the CHS model. This restricts the ability to sustain differences between trajectory orbits on successive circadian cycles and prevents the slight shifts in sleep onset phases necessary for the stability of these solutions. The solutions in these particular ρ intervals are affected because the additional sleep episode occurring in a circadian cycle (the 2nd sleep episode for $\rho \in (\frac{1}{2}, 1)$ and the 4th sleep episode for $\rho \in (\frac{1}{4}, \frac{1}{3})$) occurs at phases near $\Phi = 0.25$. These constraints do not affect the newly obtained sleep onset phase in the stable $\rho = \frac{1}{3}$ solution ($\Phi \approx 0$), and therefore more types of solutions with $\rho \in (\frac{1}{3}, \frac{1}{2})$ are detected in this regime. The $\rho = \frac{1}{2}, \frac{1}{4}$ stable solutions are delimited by a BC-S $\rightarrow$ BC-U $\rightarrow$ SN bifurcation sequence, while the $\rho = \frac{1}{3}$ solution is characterized by the sequence SN $\rightarrow$ BC-U $\rightarrow$ BC-S.

3.5 Discussion

In this Chapter, we analyzed the bifurcations in an ODE based sleep-wake flip-flop model under circadian rhythm modulation. Our study highlights how applying multiple techniques that reveal model solution structures and their dependence on parameters can facilitate a full bifurcation analysis for a non-autonomous, high-dimensional piecewise smooth dynamical system. We applied fast-slow decomposition

to reveal an underlying $Z-$shaped solution manifold that supported the orbits of stable solutions. Tracking stable orbits on the $Z-$shaped surface as homeostatic sleep drive time constants were varied showed how the profile of the folds of the surface dictated and participated in border collision bifurcations of solutions when solution trajectories made tangent intersections with the folds. For border collision bifurcations of stable solutions, we were able to visualize the tangent intersection of the trajectory with the folds of the $Z-$shaped surface, which informed understanding of border collision bifurcations of unstable solutions. Importantly, knowledge of the $Z-$shaped surface enabled the numerical computation of circle maps for model dynamics, as initial conditions were chosen at the upper fold (saddle-node) curves. The circle maps allowed tracking of fixed point solutions, representing periodic solutions in the model, as parameters varied and identification of saddle-node bifurcations as well as border collision bifurcations of unstable periodic solutions. The value of using circle maps to identify and track bifurcations was previously demonstrated in the Two Process Model [14] (see below) for which the maps can be computed analytically. Overall, our multi-pronged approach may be applied to other non-autonomous, piecewise-smooth systems.

Our analysis focused on the effects of varying two physiologically-motivated factors that affect timing and duration of sleep episodes: The time constants of the homeostatic sleep drive and the profile of the SCN firing rate. The primary bifurcation sequence delimiting stable solutions as the homeostatic drive time constants were decreased (by decreasing the scaling parameter k) was SN $\rightarrow$ BC-U $\rightarrow$ BC-S. This sequence was dictated by the shape of the circle maps which exhibit discontinuities with infinitely increasing slopes on one side and finite slopes on the other side. The SN $\rightarrow$ BC-U sequence reflects the gain and loss of fixed points on the map branch(es) near the infinite slope(s) while the BC-S bifurcation reflects the loss of the stable solution on the other end of the map branch(es). This primary bifurcation sequence was modulated

by variation of the profile of the SCN firing rate, through the parameter α_{SCN}.

One such modified sequence observed for stable solutions displaying multiple sleep episodes per circadian cycle at smaller values of k, for example $\rho \leq \frac{1}{3}$ for some α_{SCN} values, was SN $\rightarrow$ BC-U $\rightarrow$ BC-U $\rightarrow$ SN. This sequence occurred due to deformation of circle maps such that the finite slope at the discontinuity was less than -1. Our analysis of the loss of stability of the $\rho = 1$ solution as α_{SCN} was decreased provided a clear illustration of how this modification can occur as the finite slope at the discontinuity passes through 1.

Another modified sequence observed for multiple sleep episode solutions at small k values and larger α_{SCN} values was SN $\rightarrow$ SN. This sequence occurred when circle maps were continuous and tangent intersections of trajectories with the folds of the $Z-$shaped surface did not occur. This was because the homeostatic sleep drive varied sufficiently fast (small k) and the SCN firing rate profile varied sufficiently slowly (large α_{SCN}).

These bifurcation sequences obtained in the SWFF model are similar to those identified in the classic Two Process model under similar parameter variation. Specifically, Bailey et al. [14] performed an analytic bifurcation analysis of the Two Process model using circle maps as the level of the lower circadian threshold was varied leading to similar transitions between monophasic and polyphasic sleep patterns as obtained when homeostatic time constants are varied. In regimes where the amplitude of the circadian thresholds were sufficiently large, they found SN $\rightarrow$ BC-U $\rightarrow$ BC-S bifurcation sequences delimiting the stable regimes of solutions that followed a period adding sequence. In this regime, the analytically computed circle maps were monotonic and discontinuous with an infinite slope on one side of the gap, similar to the computed circle maps for the SWFF model. In regimes where the circadian threshold amplitudes were small, the circle maps became continuous due to the absence of tangent intersections of the homeostatic sleep process with the circadian thresholds

and bifurcation sequences as circadian threshold levels were varied changed to SN $\rightarrow$ SN.

In our analysis, we found that that the complexity of bifurcations increased for small values of α_{SCN}, as may be expected with steeper profiles of the folds of the $Z-$shaped surface. This was especially true for $\rho = \frac{1}{2}$ solutions which displayed intervals of bistability for some α_{SCN} values. Interestingly, the evolution of the two stable $\rho = \frac{1}{2}$ solutions as k decreased changed for different values of α_{SCN}. For the highest α_{SCN} values in this region of bistability, the 2nd stable solution gained stability in a saddle node and then a subsequent saddle node bifurcation destroyed the original stable solution, thus the solutions replaced one another as k decreased. For lower α_{SCN} values in the bistability region, the 2nd stable solution gained stability in a saddle node bifurcation and then was destroyed in a border collision (stable) bifurcation, leaving the original solution as the only stable solution. For an intermediate value of α_{SCN}, both solutions lost stability at the same k value in a coincident saddle node and border collision (stable) bifurcation, each bifurcation involving one of the stable fixed points.

Coexistence of stable solutions can occur in piecewise smooth maps with discontinuities [11, 94]. In many such maps showing coexistence of stable solutions, such as bistability, the values of the map branches across the discontinuity cover an overlapping interval. In our maps, there is no overlap of values of the map branches across the discontinuities, instead bistability emerges due to a deformation of the shape of map branches that introduces multiple fixed points. Given the similarity in its dynamics with the SWFF model, the Two Process model may be a good reduced system to formally analyze this mechanism for bistability, since it is analytically tractable. While bistability has not been previously reported in the Two Process model, an analysis in which the profile of Process C is varied as done here has not been conducted to our knowledge.

The striking effect of steeper profiles of the SCN firing rate (small α_{SCN}) was the winnowing of certain stable solutions, namely the $\rho \in (\frac{1}{2}, 1)$ and the $\rho \in (\frac{1}{4}, \frac{1}{3})$ solutions. Solutions that persisted in these ρ intervals as α_{SCN} decreased had rotation numbers of the form $n/(n+1)$. A similar winnowing of solutions has been observed in threshold models when the profile of the threshold is a square wave [6]. By analyzing the CHS model, where the SCN firing rate profile is a square wave, we found that solution winnowing was due to constraints on sleep onset phases near $\Phi = 0.75$ and $\Phi = 0.25$, at the edges of the square wave. Specifically, the steep slope of the SCN profile limited the slight variation in sleep onset phases on successive circadian cycles necessary for $\rho \in (\frac{1}{2}, 1)$ and the $\rho \in (\frac{1}{4}, \frac{1}{3})$ solutions.

Our work demonstrates that the combined effects of the sleep homeostat and circadian waveform modulate the timing, duration and number of sleep episodes in complex ways. These findings suggest that interindividual differences manifested in the time constants dictating the variation of the homeostatic sleep drive [136] affect the transition from early childhood sleep schedules that include naps to monophasic nighttime sleep that characterizes adult sleep schedules [89, 138, 88]. This transition process could be further modulated by the circadian rhythm. Future work is needed to connect the changes observed in the theoretical context of this simplified model to behavior observed in early childhood development. However, our results suggest a pertinent role of SCN activity profile, which is affected by seasonality and light conditions [157], in modulating the effects of homeostatic sleep drive variations.

CHAPTER IV

Bifurcations of NREM-REM Cycling and Sleep-Wake Patterns by Homeostatic Sleep Drive Modulation

4.1 Introduction

In humans, regular alternations between REM and NREM sleep give rise to ultradian (recurring with a period less than 24 hours) cycling across the sleep episode [7]. In this chapter[1], we use physiologically-based mathematical modeling to determine how the time scale of sleep homeostasis affects sleep episode timing with a particular focus on the influence of and variation in NREM-REM ultradian cycling during sleep episodes.

The circadian and homeostatic sleep drives influence the interactions between REM and NREM sleep states during a sleep episode. In humans and other species, the occurrence of REM sleep is strongly modulated by the circadian rhythm with a lower propensity for entering into the REM state during times of high circadian drive [37, 51]. High homeostatic sleep drive following sleep deprivation promotes NREM sleep over REM sleep during initial recovery sleep [51]. Furthermore, there is evidence that changes in sleep need interact with ultradian NREM-REM cycling in

[1]A manuscript based on these results has been submitted to *Mathematical Biosciences*.

early childhood [102].

Neuronal sleep-wake regulatory networks are largely conserved across mammalian species, but differences in network interactions give rise to the great phylogenetic diversity of sleep-wake behavior [124, 155]. As mentioned previously, the sleep-wake regulatory network produces a range of sleep behaviors across the human lifespan with frequent transitions between sleep and wake states in infants, regular napping behavior in early childhood, and a consolidated nighttime sleep period in adults [34]. These ontogenetic changes are likely driven by changing dynamics of the homeostatic sleep drive, and experiments have identified differences in the rates of growth and decay of SWA in humans at different life stages [66, 87].

Mathematical modeling has contributed to our understanding of the effects of changing homeostatic dynamics on sleep timing. Previous studies in two-state mathematical models of sleep-wake regulation examined implications of homeostatic variation for inter-species differences [124] and changes in sleep from adolescence to old age [147]. These results support a key role for homeostatic time constants in producing distinct patterns of sleep-wake behavior. In addition, previous studies, including our work in Chapter III, have analyzed the types and sequences of bifurcations produced as homeostatic time constants changed [147, 14]. However, the analyzed models simulate only two behavioral states, wake and sleep, and do not account for NREM-REM cycling during the sleep period. Indeed, it is unknown how NREM-REM cycling may affect the patterns of sleep-wake behavior as homeostatic time constants change.

As a first step in understanding the effects of NREM-REM cycling on homeostatically driven changes in sleep patterns, this chapter presents a computationally-based analysis of the bifurcations in sleep timing produced by varying homeostatic time constants in the three-state sleep-wake regulatory network model. This work provides novel insights into the potential role of REM sleep in the evolution of sleep-wake behavior across development. To analyze the types of bifurcations that occur in the

piecewise smooth sleep-wake network model, we construct one-dimensional circle maps that represent key dynamics of the full sleep-wake network model [25]. By computing representative maps for distinct intervals of homeostatic time constants, we gain insight into the types of bifurcations that occur and elucidate the effects of REM sleep on sequences of bifurcations in sleep timing.

The chapter is organized as follows: in Section 4.2 we present notation utilized to describe solutions of the mathematical model; in Section 4.3 we describe the bifurcations produced by varying the time constants of the homeostatic sleep drive with a specific focus on the transition from monophasic to polyphasic daily sleep; and in Section 4.4 we provide a brief summary of our results, relate them to previous results in two-state models of sleep-wake regulation, and discuss implications for sleep in early childhood.

4.2 Varying the dynamics of homeostatic sleep drive: our framework

In this work, we employ the three-state sleep-wake regulatory network model presented in Chapter II to investigate the effects of NREM-REM cycling on bifurcations occurring in the transition from monophasic (one sleep per day) to polyphasic (multiple daily sleeps) sleep behavior induced by decreasing the time constants of the homeostatic sleep drive h. The model incorporates the circadian clock model by Forger et al. [64] and parameter values implemented in this work can be found in Table 2.2.

We scale the time constants τ_{hw} and τ_{hs} by a parameter $0 < \chi \leq 1$. Thus, as χ decreases, h grows and decays more quickly causing sleep propensity to accumulate and dissipate faster, respectively. Recall that for default parameter values ($\chi = 1$), the model generates a stable periodic solution displayed in Figure 2.4B. This solution has one sleep episode per circadian day with a duration of 7.89 h; each sleep episode

contains four REM bouts.

We will use the following notation to indicate the numbers of sleep episodes per circadian cycle and REM bouts per sleep episode in stable solutions. A stable pattern that repeats after n circadian cycles is represented as $\{p^1_{r1}, p^2_{r2}, \ldots, p^n_{rn}\}^\infty$ where the number p^i gives the number of sleep episodes on the i^{th} circadian cycle and the number ri is a p^i-tuple whose entries represent the number of REM bouts in each sleep episode. For example, the default solution at $\chi = 1$ is represented as $\{1_4\}^\infty$, and a stable 2-cycle that occurs at $\chi = 0.8625$ is represented as $\{1_4, 1_4\}^\infty$. As another example, a pattern that alternates between 1 and 2 sleeps per day occurs at $\chi = 0.649$ and is represented as $\{1_3, 2_{(4,3)}\}^\infty$. On the first circadian cycle one sleep episode involving 3 REM bouts (1_3) occurs. On the second circadian cycle, two sleep episodes occur; one involves 4 REM bouts, while the other involves 3 REM bouts ($2_{(4,3)}$).

To quantify the sleep patterns generated as χ is decreased, we define a 'rotation number' of sleep episodes, $\rho = \frac{q}{p}$, where p is the number of sleep episodes in the pattern occurring over q circadian days [11]. If a stable pattern is not detected, we approximate ρ to be the average number of the total circadian days over the total sleep episodes in a 120 day simulation.

Similarly, to quantify NREM-REM cycling patterns during sleep episodes, we define a 'REM rotation number' as $\tilde{\rho}_{REM} = \frac{p}{r}$, where r is the number of REM bouts occurring during the p sleeps in the pattern. If a stable pattern cannot be detected, we approximate $\tilde{\rho}_{REM}$ by the total number of sleep episodes over the total number of REM bouts in a 120 day simulation. $\tilde{\rho}_{REM}$ takes on values less than 1. However, since it is more intuitive to talk about REM episodes per sleep, we will use the reciprocal of the REM-rotation number for the rest of this study. We will denote that as ρ_{REM} and refer to it as the 'REM rotation number' for simplicity.

Based on these definitions, the stable sleep patterns for $\chi = 1$ and $\chi = 0.8625$ discussed above are both associated with $\rho = 1$ and $\rho_{REM} = 4$. The sleep pattern for

$\chi = 0.649$ is associated with $\rho = \frac{1}{2}$ and $\rho_{REM} = \frac{10}{3}$.

In the analysis below, we investigate whether there is an underlying structure in ρ and ρ_{REM} as χ is reduced and how to properly describe it. For example, one such structure emerges from a period-adding bifurcation. A period-adding bifurcation dictates that the average number of sleep episodes per circadian cycle, i.e. the reciprocal of the rotation number as defined above, follows a predictable sequence that can be characterized by a Farey sequence. Elements of the Farey sequence obey the Farey addition (see Chapters I and III for more details).

4.3 Results

In the three-state sleep-wake model representing wake and NREM-REM cycling, we find complex sequences in the transitions of solutions as the homeostatic sleep drive time constants are decreased. Previous work in two-state sleep-wake models analyzing the transition from monophasic to polyphasic sleep patterns as time constants for the homeostatic sleep drive were decreased showed that sleep patterns varied in period-adding bifurcation sequences [14, 147, 10].

In the three-state model, as shown below, while the Farey sequence in sleep episodes per circadian cycle is overall generally retained, bifurcations in NREM-REM cycling introduce additional features including period-doubling cascades, intervals of bistability, and disruption of the period-adding structure. When the scaling parameter $\chi = 1$, the model produces a stable solution corresponding to the typical adult sleep pattern of one consolidated nocturnal sleep episode per day. As χ is decreased, we find χ intervals that generate polyphasic sleep solutions consisting of regular and alternating daily sleep patterns. For example, an average of two sleep episodes per day occurred for ($\chi \in [0.41, 0.542]$), and three sleep episodes per day occurred for ($\chi \in [0.264, 0.29]$) (Figure 4.1). Between the χ-intervals associated with n and $n+1$ sleep episodes per day, respectively, there are χ values associated with higher order

sleep patterns with periods over several circadian days that involve some days with n sleeps and some days with $n+1$ sleeps. For example, around $\chi = 0.65$ we observe that the pattern alternates between one and two sleeps per day.

As described in Section 4.2, these sleep patterns may be quantified with a 'rotation number' of sleep episodes, $\rho = \frac{q}{p}$, where p is the number of sleep episodes in the pattern occurring over q circadian days. The bifurcation diagram of ρ as a function of the scaling parameter χ (Figure 4.1B) depicts stable solutions (black points) obtained after simulating the model for 120 days. If a stable pattern was not detected, the approximate ρ is plotted (gray points). The sequence of rotation numbers of stable sleep patterns is similar to a Farey sequence that reflects a period adding bifurcation structure. In contrast, for the Two Process model, and simple sinusoidal threshold systems under similar parameter variations, the rotation number is a Cantor function or a Devil's staircase in terms of the varying parameter (namely a monotonic, continuous function that has derivative equal to 0 almost everywhere that attains every rational number in the Farey sequence) which results from the period-adding bifurcation. In two-state sleep-wake models, numerical simulations suggest a similar trend for typical circadian signaling [14]. Here, we numerically detect rotation numbers that form a subset of the full Farey sequence.

A significant difference between the two-state and three-state model is that the rotation numbers do not decrease monotonically with χ and are not unique in the three-state model. For example, within the $\rho = \frac{2}{3}$ interval there are χ values that generate a $\rho = \frac{7}{10}$ stable solution indicating bistability of solutions.

In the three-state model, NREM-REM cycling additionally varies with χ within intervals of constant ρ. As described in Section 4.2, we quantify NREM-REM cycling patterns during sleep episodes using a 'REM rotation number' $\rho_{REM} = \frac{r}{p}$, where r is the number of REM bouts occurring during the p sleeps in the pattern (Figure 4.1C, blue points). If a stable pattern is not detected, an approximate ρ_{REM} is computed

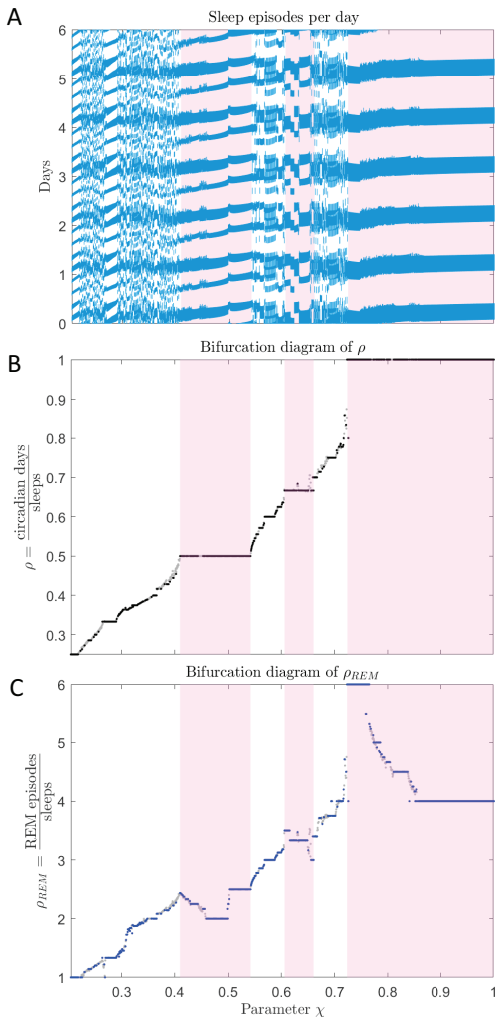

Figure 4.1: Summary of sleep patterns and bifurcation diagrams of ρ and ρ_{REM} as the homeostatic sleep drive time constants are decreased with respect to the scaling parameter χ. The pink shaded regions correspond to χ-intervals of $\rho = 1, 2/3, 1/2$ solutions. A. Patterning of sleep-wake behavior varies with scaling parameter χ. Sleep periods over 6 days (y-axis) are shown as a function of χ (x-axis). As χ decreases, sleep patterns transition from one sleep episode per day near $\chi = 1$ to two sleep episodes per day near $\chi = 0.542$ to three sleep episodes per day near $\chi = 0.29$. B. Bifurcation diagram of the rotation number, ρ, denoting stable (black dots) and quasi-periodic (gray dots) solutions with respect to χ. The parameter χ is on the x-axis and the rotation number ρ, defined as the number of circadian days over the number of sleep episodes in the stable sleep pattern is on the y-axis. C. Bifurcation diagram of the REM rotation number, ρ_{REM}, denoting stable (blue dots) and quasi-periodic (gray dots) solutions with respect to χ. The REM rotation number, ρ_{REM}, is defined as the number of REM bouts over the number of sleep episodes in the sleep pattern. For all panels, the step size for χ was 0.0005.

(gray points). For $\chi = 1$ we have $\rho_{REM} = 4$ corresponding to 4 REM bouts per sleep episode.

As χ is decreased from 1, ρ_{REM} changes within χ intervals of constant ρ indicating that the number of REM bouts during sleep episodes changed while the number of sleep episodes per circadian cycle did not. Additionally, bistability is exhibited in the bifurcation diagram of ρ_{REM}, as there are $\chi-$values in which two stable REM rotation numbers were found (Figure 4.2). In the three-state sleep-wake model, the associated circle maps are non-invertible which can lead to non-uniqueness of the rotation number of either sleep or REM episodes [95].

4.3.1 Bifurcations associated with NREM-REM cycling during monophasic sleep

Changes in NREM-REM cycling are particularly observed over the χ interval where $\rho = 1$ ($\chi \in [0.7235, 1]$) during which ρ_{REM} increases from 4 to 6 (Figure 4.2). In this section we show that, in this χ interval, ρ_{REM} values of stable solutions (in blue) in neighboring χ intervals are related by Farey addition with period-doubling cascades in intervals of constant ρ_{REM} and bistability of ρ_{REM} between some χ intervals.

To understand the types of bifurcations generating the changes in NREM-REM cycling as well as the occurrence of bistability, we employ our sleep onset circle maps. We explain the bifurcations in the maps and the evolution of sleep patterns as χ decreases from 1, and we follow the bifurcation diagram of ρ_{REM} (Figure 4.2) from lower to higher values of ρ_{REM}.

The types of bifurcations observed include saddle-node, period-doubling and border collision bifurcations. A border collision in the k^{th} return map occurs when the border of the map curve intersects the diagonal, $\Phi_{n+k} = \Phi_n$, and results in the creation or destruction of a fixed point (stable or unstable). This border collision bifurcation in the map corresponds to an orbit (stable or unstable) making a tangent intersection

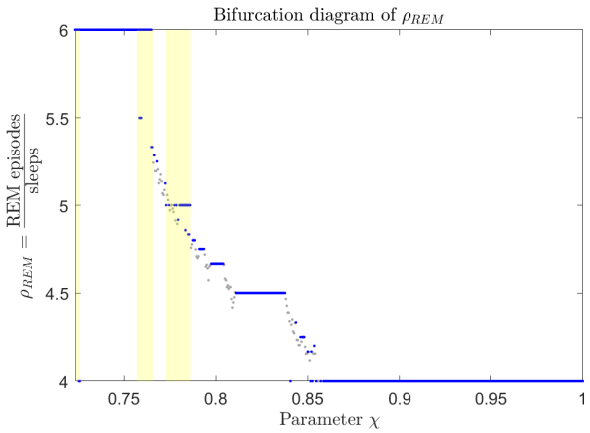

Figure 4.2: The bifurcation diagram of ρ_{REM} in the range of χ for which $\rho = 1$. There is an underlying, but not strict, period-adding structure in the sequence of ρ_{REM} values as χ is decreased. In addition, there are intervals of χ in which bistability occurs (denoted by the yellow shaded regions).

with the saddle-node curves of the Z-shaped surface (Figure 2.5B) which is referred as a grazing bifurcation of the flow [45].

$\underline{\rho_{REM} = 4}$

As described above, for the default value $\chi = 1$, the sleep onset map exhibits a stable fixed point on the map branch corresponding to 4 REM bouts per sleep episode (green branch in Figure 2.6). As χ decreases, the map evolves and the location and stability of the fixed point changes (Figure 4.3). For $\chi = 0.867$, the fixed point persists on the same map branch and occurs at a slightly earlier circadian phase. However, at this χ value the slope of the map curve at the fixed point is estimated to be equal to -1 (Figure 4.3A), indicating a loss of stability of the fixed point. For χ values in this regime, stable solutions correspond to higher order cycles. For example, for $\chi = 0.8625$ we observe a two day pattern in which one sleep episode occurs on each day, but the sleep onset phases of these episodes are distinct. Each sleep episode contains four REM bouts occurring at slightly different circadian phases. This pattern consists of two sleep episodes per two days with 4 REM bouts per sleep which means that the rotation numbers are $\rho = \frac{2}{2} = 1$ and $\rho_{REM} = \frac{8}{2} = 4$. Thus, the decrease in the value

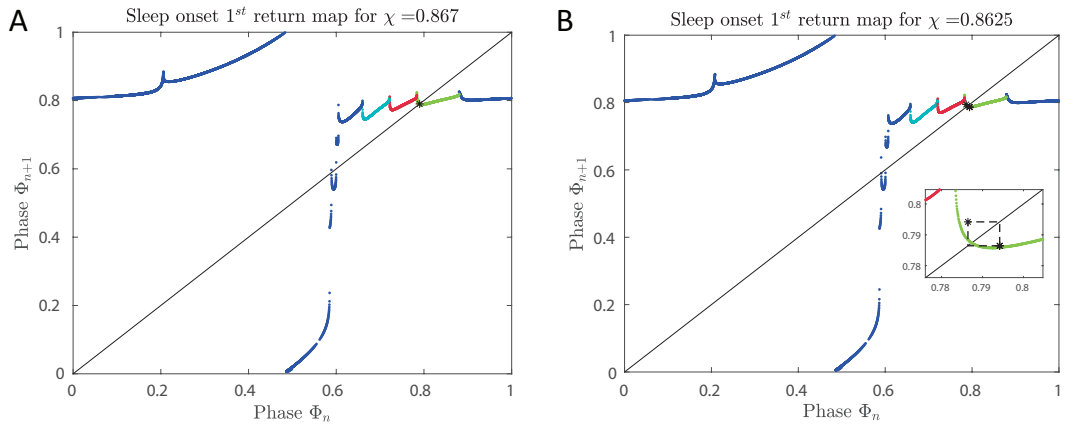

Figure 4.3: Maps in the $\rho_{REM} = 4$ regime showing a period doubling bifurcation. The green, red and light blue map branches correspond to circadian phases of sleep episodes involving 4, 5, and 6 REM bouts, respectively. A. The first return map for $\chi = 0.867$ has one stable fixed point on the green branch involving sleep episodes with 4 REM bouts. The slope of the map at the fixed point is -1 designating the loss of stability of the fixed point at a period doubling bifurcation. B. The first return map for $\chi = 0.8625$ has one unstable fixed point and a higher (second) order cycle detected by cobwebbing (inset) involving 2 phase points on the green branch representing sleep episodes with 4 REM bouts.

of the slope at the fixed point below -1 leads to a period-doubling bifurcation. In this regime, the period of the pattern described by higher order cycles is a power of 2, and contains sleep episodes involving four REM bouts. These higher order cycles can be detected in the map through the method of cobwebbing. In particular, one can determine which map branches are visited and the order in which they are visited by starting at one of the phases in the stable pattern. For example, for $\chi = 0.8625$ a cobwebbing cycle of order two exists that alternates between two values on the four-REM-branch on either side of the unstable fixed point (Figure 4.3B).

As χ decreases slightly further from the period-doubling bifurcation, we find a $\{1_4, 1_4, 1_4, 1_4\}^\infty$ pattern, corresponding to another period doubling. As shown in Figure 4.2, the $\rho_{REM} = 4$ regime ends at $\chi = 0.8545$ with a $\{1_4, 1_4, 1_4\}^\infty$ solution that follows the apparent period doubling cascade that we detect numerically for $\chi \in [0.8585, 0.866]$.

Additionally as the map shifts with decreasing χ, the shapes of the map branches

also change and some branches are lost. For example, for $\chi \sim 0.86$, the branch associated with eight REM bouts has disappeared. Since sleep need accumulates and dissipates at a higher rate with lower χ, the total number of REM bouts that can occur during a sleep episode decreases leading to the loss of sleep episodes with highest numbers of REM bouts.

$\underline{\rho_{REM} \in (4,5)}$

As χ continues to decrease, the map evolves further such that stable orbits visit the map branch involving sleep episodes with five REM bouts (Figure 4.4, red branch). Stable solutions consist of higher order cycles where sleep onset phases alternate between points on the four-REM- and five-REM-branches of the map. For example, at $\chi = 0.8535$ the stable solution $\{1_4, 1_4, 1_4, 1_4, 1_5\}^\infty$ is detected. These higher order cycles follow a period-adding type sequence as χ decreases with the number of sleep episodes with 4 REM bouts decreasing incrementally with each stable solution. In the interval $\chi \in [0.811, 0.8375]$, the stable solution is $\{1_4, 1_5\}^\infty$ with $\rho_{REM} = 4.5$, and for lower χ values the number of sleep episodes with 5 REM bouts in the pattern increases incrementally as ρ_{REM} approaches 5. Within this period-adding sequence, we detected some period-doubling transitions where the same sequence is repeated twice with slight variation in the phases of sleep onsets.

As shown in the ρ_{REM} bifurcation diagram (Figure 4.2), the $\{1_5\}^\infty$ solution with $\rho_{REM} = 5$ gains stability at $\chi \approx 0.786$ where higher order cycles also are stable, leading to an interval of bistability in the system. Interestingly, the structure of the map predicts the existence of the two stable solutions that are associated with distinct sets of fixed points on the map (Figure 4.4A). Specifically, the higher order cycles $\{1_4, \ldots, 1_4, 1_5, \ldots, 1_5\}^\infty$ manifest on the map as an orbit that moves between the left side of the four-REM-branch (green) and the right side of the five-REM-branch (red). In contrast, the $\{1_5\}^\infty$ solution first appears when the left side of

the five-REM-branch makes a tangent intersection with the $\Phi_{n+1} = \Phi_n$ diagonal, resulting in a saddle-node bifurcation. At $\chi = 0.786$ (Figure 4.4A), there are 4 fixed points on the map. The higher order cycle $\{1_4, 1_5, 1_5, 1_5\}^\infty$ occurs near unstable fixed points on the four-REM-branch and the right side of the five-REM-branch. The $\{1_5\}^\infty$ solution is associated with the stable fixed point of the stable-unstable fixed point pair on the left side of the five-REM-branch. Bistability with the $\{1_5\}^\infty$ solution and higher order cycles is also found at $\chi = 0.785$ and 0.7795 where the respective ρ_{REM} values for the higher order cycles are $\frac{58}{12} = \frac{29}{6}$ and $\frac{59}{12}$ and the solutions are $\{1_5, 1_4, 1_5, 1_5, 1_5, 1_5, 1_5, 1_4, 1_5, 1_5, 1_5, 1_5\}^\infty$ (a period-doubling solution) and $\{1_5, 1_5, 1_4, 1_5, 1_5, 1_5, 1_5, 1_5, 1_5, 1_5, 1_5, 1_5\}^\infty$, respectively.

$\underline{\rho_{REM} = 5}$

The $\{1_5\}^\infty$ solution is stable in the interval $\chi \in [0.773, 0.786]$ (Figure 4.2). The stable fixed point associated with this solution corresponds to sleep onset phases on the left side of the five-REM-branch that represent earlier phases compared to the phases that participate in the higher order cycle. The $\{1_5\}^\infty$ solution loses stability when the slope of the branch at this fixed point decreases below -1. In the narrow interval $\chi \in [0.7805, 0.7815]$, we establish numerical evidence for a period-doubling cascade involving $\{1_5, \ldots, 1_5\}^\infty$ solutions.

$\underline{\rho_{REM} \in (5, 6]}$

The bifurcation sequence associated with the appearance of sleep episodes with 6 REM bouts is similar to the sequence described for the sleep episodes with 5 REM bouts. Specifically, as χ decreases from 0.773, we find stable higher order cycles with sleep onset phases alternating between the 5-REM- (red branch) and 6-REM-branches (light blue branch) of the map (Figure 4.4B). These stable orbits form a period-adding-type sequence as χ decreases with the number of sleep episodes containing 5

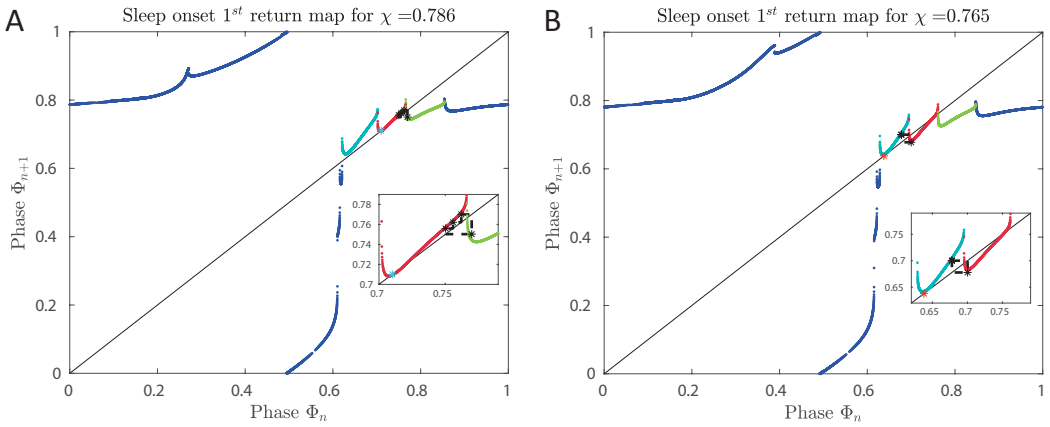

Figure 4.4: First return maps designating the onset of the $\rho_{REM} = 5$ and $\rho_{REM} = 6$ solutions. The green, red and light blue map branches correspond to circadian phases of sleep episodes involving 4, 5, and 6 REM bouts, respectively. A. First return map for $\chi = 0.786$ showing bistability of solutions with $4 < \rho_{REM} < 5$ and $\rho_{REM} = 5$. The light blue asterisk (at $(\Phi_n, \Phi_{n+1}) = (0.71, 0.71)$ on the red branch) indicates the onset of the stable $\rho_{REM} = 5$ solution in a saddle-node bifurcation. This solution coexists with a higher order cycle of $\rho_{REM} = \frac{19}{4}$ illustrated by cobwebbing on the map (inset). B. The first return map for $\chi = 0.765$ showing bistability of solutions with $5 < \rho_{REM} < 6$ and $\rho_{REM} = 6$. The red asterisk (at $(\Phi_n, \Phi_{n+1}) = (0.6379, 0.6379)$ on the light blue branch) indicates the onset of the stable $\rho_{REM} = 6$ solution in a saddle-node bifurcation. This solution coexists with a higher order cycle of $\rho_{REM} = \frac{11}{2}$ illustrated by cobwebbing on the map (inset).

REM bouts decreasing until the $\{1_5, 1_6\}^\infty$ solution is obtained at $\chi = 0.7595$. At the higher value $\chi = 0.765$, the stable solution $\{1_6\}^\infty$ with $\rho_{REM} = 6$ appears for the first time when the six-REM-branch of the map intersects the diagonal $\Phi_{n+1} = \Phi_n$ at a saddle-node bifurcation. As above, the bistable solutions correspond to different sets of fixed points on the map. The stable fixed point of the stable-unstable fixed point pair on the left side of the six-REM-branch is associated with the $\{1_6\}^\infty$ solution, while the sleep onset phases of the higher order orbits alternate between the right side of the six-REM-branch and the left side of the five-REM-branch (Figure 4.4B, inset). There are also 2 unstable fixed points near the right end of the five-REM-branch (one on the four- and one on the five-REM branch), however, we did not numerically detect any stable higher order orbits near those points.

Summary

In summary, we have shown that in the $\rho = 1$ regime of the three-state model, NREM-REM cycling introduces a sequence of bifurcations as χ is reduced. These bifurcations are initiated by a loss of stability in the $\{1_4\}^\infty$ solution and include period-adding-type patterns in the numbers of REM bouts and bistability at the transitions to the $\{1_5\}^\infty$ and $\{1_6\}^\infty$ solutions. Specifically, the $\{1_n\}^\infty$ $(n = 4, 5)$ solutions lose stability in period-doubling bifurcations when the slope of the map at the stable fixed point decreases below -1 because of the non-monotonic shape of the map branches. For $n = 4, 5$, period-doubling solutions are replaced by solutions involving daily sleep episodes with n and $n + 1$ REM bouts that follow a period-adding sequence. These higher order stable orbits display sleep onset phases near an unstable fixed point on the map. The stable solutions $\{1_n\}^\infty$ $(n = 5, 6)$ are initiated at saddle-node bifurcations which introduce stable and unstable fixed points on the map. These saddle-node bifurcations occur at χ values where the higher-order cycle solutions retain stability leading to intervals of bistability near these bifurcations. The unstable fixed point associated with higher order cycling between $\{1_4\}^\infty$ and $\{1_5\}^\infty$ solutions is eventually lost through a border collision bifurcation.

Interestingly, this sequence of bifurcations does not fully apply in the evolution and finally disappearance of the $\{1_6\}^\infty$ solution at $\chi = 0.7235$. As χ is reduced from 0.765 (where the $\{1_6\}^\infty$ solution gains stability in a saddle-node bifurcation), the six-REM-branch shrinks to cover a narrower interval of circadian phases but the stable and unstable fixed points remain on the branch. At $\chi = 0.7235$, the lowest χ value where the $\rho = 1$ solution exists, the stable and unstable fixed points on the six-REM-branch coalesce in a saddle-node bifurcation leading to the loss of the $\{1_6\}^\infty$ solution (Figure 4.5B). Additional occurrences of bistability appear near this bifurcation where at the slightly higher χ value of $\chi = 0.726$ we find a stable higher order orbit with $\rho = \frac{4}{5}$, $\rho_{REM} = \frac{20}{5} = 4$, and a pattern of $\{1_5, 1_5, 1_3, 2_{(4,3)}\}^\infty$ (Figure

4.5A). Thus, near where the $\rho = 1$ solutions lose stability, the period-adding solutions in the number of sleep episodes per circadian cycle start to appear. Such bistability between these types of solutions has not been observed in two-state sleep-wake models. The first return map eventually deforms so that the six-REM-branch vanishes, as at $\chi = 0.7165$ (Figure E.1B in Appendix E), while the two neighboring five-REM branches merge into a single branch. As a result, stable or transient solutions involving sleep episodes with six REM bouts are not predicted by the map for this value of χ.

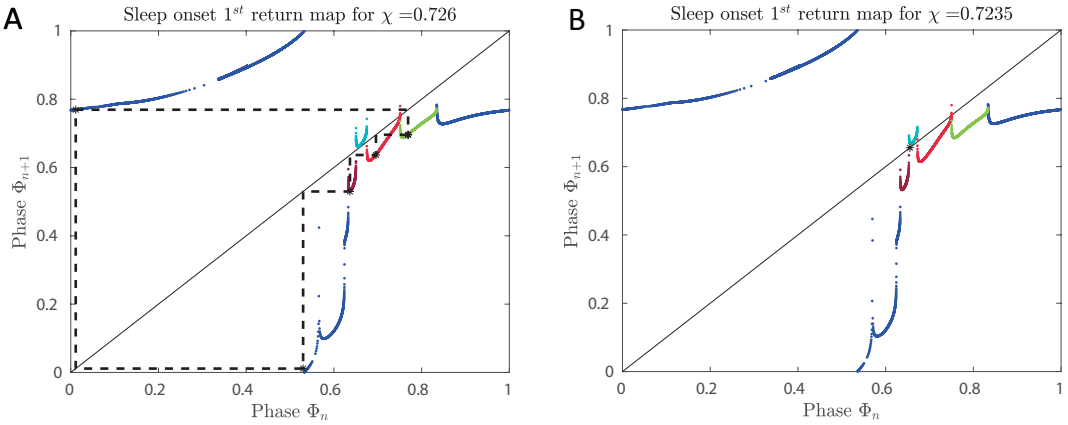

Figure 4.5: First return maps toward the end of the χ range for the stable $\rho = 1$ solution. The green, red, light blue map, and purple branches correspond to circadian phases of sleep episodes involving 4, 5, 6, and 5 REM bouts, respectively. A. The first return map for $\chi = 0.726$ showing the cobwebbing of the stable solution with $\rho < 1$ ($\{1_5, 1_5, 1_3, 2_{(4,3)}\}^\infty$) in a bistable regime with the $\{1_6\}^\infty$ solution (stable fixed point on the light blue branch). The stable solution with $\rho < 1$ visits the five-REM (purple and red), four-REM (green) and three-REM (dark blue) branches. B. The first return map for $\chi = 0.7235$. The $\rho = 1$ solution ceases to exist in a saddle-node bifurcation on the six-REM branch (light blue).

4.3.2 Effects of NREM-REM cycling on the monophasic to biphasic sleep transition

The loss of existence of the $\rho = 1$ solution designates the appearance of circadian cycles with two sleep episodes. As χ decreases through the transition from stable monophasic to stable biphasic sleep, the ρ bifurcation diagram reflects an underlying period adding structure (Figure 4.1B and 4.6A). However, in some χ intervals the

monotonic change in ρ characterizing the period adding structure is disrupted (Figure 4.6A). Specifically, the sequence of rotation numbers ρ is irregular and non-monotonic at high values of χ in this region ($\chi \in (0.7015, 0.7235)$) and exhibits jumps within particular ρ-intervals resulting in bistability. For example, at $\chi = 0.6305$ stable solutions $\rho = \frac{2}{3}$ and $\rho = \frac{13}{19}$ both exist. Additionally, bistability is observed at the transition between distinct ρ values. For example, for $\chi \in [0.659, 0.661]$ stable solutions with $\rho = \frac{7}{10}$ (with $\rho_{REM} = 3.4$) and $\rho = \frac{2}{3}$ (with $\rho_{REM} = 3$) coexist (right end of pink shaded region in Figure 4.6A).

Variations in NREM-REM cycling contribute to the irregularity of variation in ρ as χ decreases, as illustrated in the ρ_{REM} bifurcation diagram (Figure 4.6B). In this section, we qualitatively describe characteristics of the diversity of solutions in the transition from monophasic to biphasic sleep. Since stable solutions with $\rho \in (\frac{1}{2}, 1)$ are represented in higher order return maps that are quite complex, we discuss bifurcation sequences more quantitatively and show second return maps for the $\rho = \frac{1}{2}$ solutions in the next section.

Diversity of NREM-REM cycling for solutions with constant ρ

In χ intervals of constant ρ for $\rho \in (\frac{1}{2}, 1)$, changes in ρ_{REM} may or may not follow a monotonic period-adding type sequence with decreasing χ as observed for $\rho = 1$ solutions. For example, for $\chi \in [0.5685, 0.5875]$ (red box in Figures 4.6A,B) all stable solutions have $\rho = \frac{3}{5}$ and $\rho_{REM} = 3$ corresponding to the pattern $\{1_3, 2_{(2,4)}, 2_{(3,3)}\}^\infty$. In fact, for all solutions in $\chi \in (0.542, 0.606)$, all solutions with the same ρ value have a consistent ρ_{REM} value. In contrast, for solutions with $\rho = \frac{3}{4}$, for $\chi \in [0.6875, 0.7015]$ (green box in Figures 4.6A,B), ρ_{REM} jumps from 3.75 to 4 for $\chi \in [0.6935, 0.695]$ indicating a difference in NREM-REM cycling patterns in solutions with the same ρ.

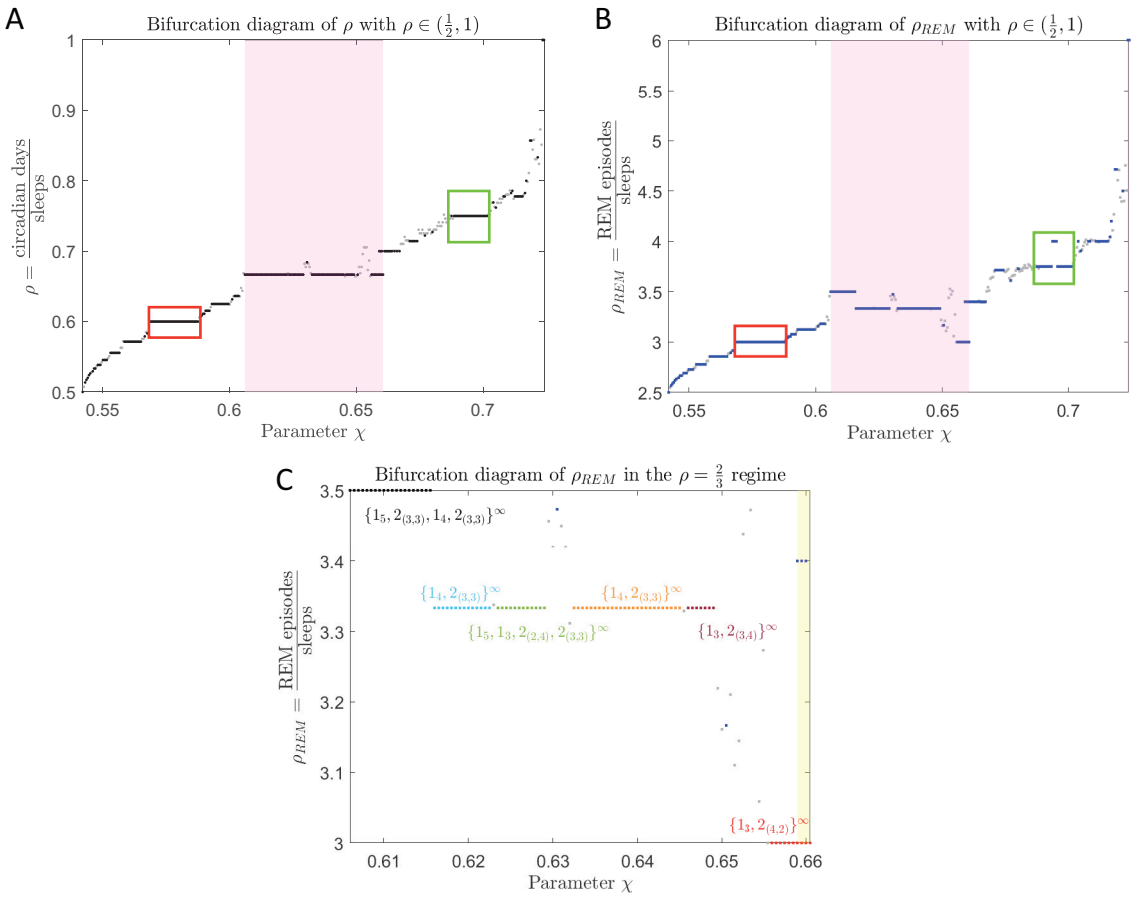

Figure 4.6: Bifurcation diagrams of ρ and ρ_{REM} in the transition from monophasic to polyphasic sleep. A,B: Bifurcation diagram of ρ (A) and ρ_{REM} (B) with $\rho \in (\frac{1}{2}, 1)$. Pink shaded regions indicate the χ interval where the majority of solutions have $\rho = \frac{2}{3}$. Green and red boxes correspond to stable solutions with $\rho = \frac{3}{4}$ for $\chi \in [0.6875, 0.7015]$ and with $\rho = \frac{3}{5}$ for $\chi \in [0.5685, 0.5875]$, respectively. These χ intervals illustrate the diversity of ρ and ρ_{REM} variations as χ decreases caused by variations in NREM-REM cycling. C: ρ_{REM} bifurcation diagram for $\chi \in [0.606, 0.6605]$ corresponding to an average sleep pattern of three sleeps per two days (i.e. $\rho = \frac{2}{3}$). The light yellow shaded region indicates an interval of bistability of stable solutions with $\rho = \frac{7}{10}$ and $\rho = \frac{2}{3}$. Intervals of constant ρ_{REM} are colored and labelled appropriately with the particular sleep pattern. Each subinterval may involve a period doubling bifurcation which is not labelled.

$\underline{\rho = \frac{2}{3}}$

As a further example, the bifurcation diagram of ρ_{REM} over the interval $\chi \in [0.606, 0.6605]$ (Figure 4.6C) illustrates the diversity of NREM-REM cycling patterns that occur in $\rho = \frac{2}{3}$ solutions. Here, ρ_{REM} values generally increase in a period-adding

type sequence. In the range $\chi \in [0.617, 0.649]$, $\rho_{REM} = \frac{10}{3}$ and reflects a stable pattern with an average number of 10 REM bouts per 3 sleep episodes. However, the distribution of REM bouts across the 3 sleep episodes varies with χ and results in four distinct stable sleep patterns across this range. At $\chi = 0.649$, the stable sleep pattern is $\{1_3, 2_{(4,3)}\}^\infty$, but at $\chi = 0.645$ the pattern changes to $\{1_4, 2_{(3,3)}\}^\infty$. This change occurs due to a phase advance of the second sleep episode with 3 REM bouts that eventually shifts it to the previous circadian day. For lower χ values, NREM-REM cycling patterns shift, leading to variable ρ_{REM} that then re-stabilizes at $\chi = 0.6235$ where the stable sleep pattern is $\{1_5, 1_4, 2_{(4,2)}, 2_{(3,3)}\}^\infty$. A period doubling bifurcation takes place for $\chi \in [0.6235, 0.6245]$ and at $\chi = 0.6225$ the pattern becomes $\{1_4, 2_{(3,3)}\}^\infty$.

This representative example emphasizes the great range of NREM-REM cycling patterns generated by the 3-state model. As the rates of build-up and dissipation of the homeostatic sleep drive modulate the timing and duration of sleep onsets, sleep onsets occur at different circadian phases that then affect the number and duration of REM bouts. Thus, small differences in homeostatic and circadian modulation can produce large variability in sleep-wake behavior. Thus, ρ, ρ_{REM}, NREM-REM cycling patterns, and, when feasible, corresponding maps should be considered simultaneously to characterize the solutions exhibiting this variability.

It is worth noting that as χ decreases, some ρ_{REM} values reoccur over different χ intervals (e.g. $\rho_{REM} = 3$). In this case, the sleep patterns are characterized by distinct ρ values, thereby allowing for the same average number of REM bouts per sleep cycle. Reoccurrence of ρ_{REM} values can take place even within the same ρ interval. This phenomenon as well as the map structure leading to it is illustrated in the next section.

4.3.3 NREM-REM cycling bifurcations in biphasic sleep

Stable biphasic sleep ($\rho = \frac{1}{2}$) solutions occur for $\chi \in [0.41, 0.542]$. NREM-REM cycling changes across this regime, with ρ_{REM} varying non-monotonically in $\rho_{REM} \in [2, 2.5]$ (Figure 4.7A). This non-monotonic variation in ρ_{REM} with χ is due to more variability in NREM-REM cycling patterns across the two daily sleep episodes, as described in the previous section for $\rho = \frac{2}{3}$ solutions. To analyze the bifurcation sequences occurring in this regime, we employ second return maps and follow the ρ_{REM} bifurcation diagram (Figure 4.7A) as χ is reduced from 0.542.

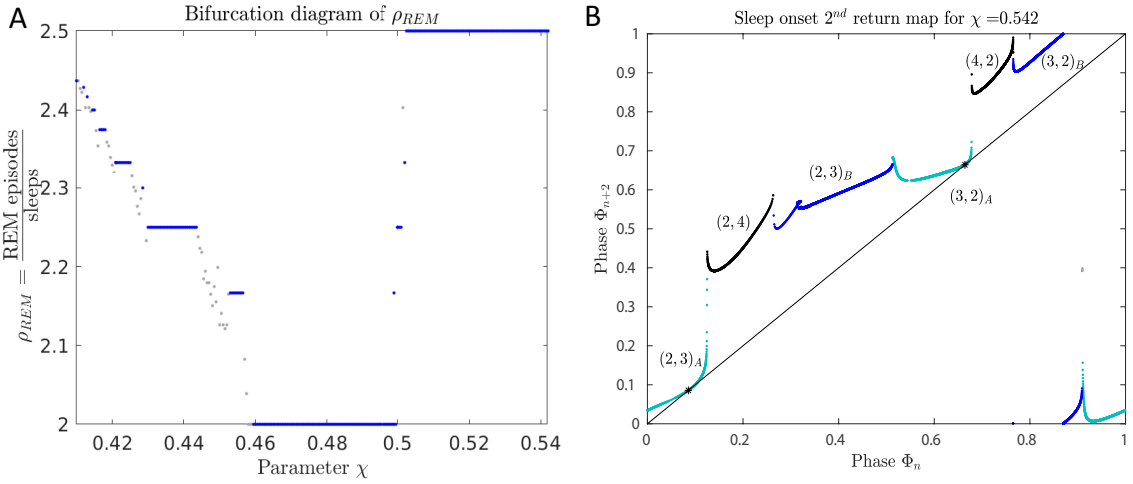

Figure 4.7: The biphasic sleep ($\rho = \frac{1}{2}$) regime. A. The bifurcation diagram of ρ_{REM} in the $\rho = \frac{1}{2}$ regime. B. The second return map for $\chi = 0.542$ introducing the $\rho = \frac{1}{2}$ solution in a saddle-node bifurcation. The stable solution has $\rho_{REM} = 2.5$. The map branches are colored and labelled according to the number of REM bouts involved in the sleep onsets with phase Φ_n and Φ_{n+1}. The dark blue and light blue branches correspond to model solutions having 2 and 3 REM bouts during the two sleep episodes, respectively. The black branches correspond to solutions with 2 and 4 REM bouts during the two sleep episodes, respectively.

Note that the second return map can be thought of as consisting of two similar copies of the same curves (Figure 4.7B). Each pair of associated curves involves the same set of model trajectories that produce two sleep cycles during their first circadian day. One curve represents the sleep onset phases of the first sleep episode of the day, while the associated curve represents the sleep onset phase of the second sleep episode

of the day .

$\underline{\rho_{REM} = 2.5}$

The $\rho = \frac{1}{2}$ regime is initiated at $\chi = 0.542$ in a saddle-node bifurcation illustrated in the second return map (Figure 4.7B). This map has two fixed points at phases about (0.0857,0.0857) and (0.6641,0.6641) formed by map curves (light blue) making tangential intersections with the diagonal. Thus, at the start of this regime, the stable periodic orbit consists of a sleep episode with two REM bouts occurring at the early rise of the circadian rhythm (near $\Phi_n = 0.0857$) followed by a sleep episode with three REM bouts occurring a little after the peak of the circadian rhythm (near $\Phi_n = 0.6641$). This results in a REM rotation number, ρ_{REM}, of 2.5. We refer to the branches on which the fixed points lie as the $(2,3)_A$ (near $\Phi_n = 0.0857$) and $(3,2)_A$ (near $\Phi_n = 0.6641$) branches. The first number in the $2-$tuple of a map branch refers to the number of REM bouts occurring in the sleep episode with onset phase, Φ_n. The second number refers to the number of REM bouts in the subsequent sleep episode with onset phase, Φ_{n+1}. The subscripted letters distinguish between multiple, but distinct, map branches corresponding to model solutions exhibiting the same numbers of NREM-REM cycles.

As χ decreases from this saddle-node point, the map attains two pairs of fixed points, one pair from each saddle-node, a stable and an unstable fixed point in each pair. The slope of the map branches at the stable fixed points is initially positive and less than 1, but as χ decreases, it becomes negative and eventually decreases through -1 at approximately $\chi = 0.503$, indicating a period-doubling bifurcation. The stable fixed points lose stability and a stable 4-cycle emerges with the pattern $\{2_{(2,3)}, 2_{(2,3)}\}^{\infty}$ at $\chi = 0.5025$. On the second return map (Figure 4.8A), the 4-cycle appears as two 2-cycles, one with sleep onset phases on the $(2,3)_A$ branch (light blue) near $\Phi_n \approx 0$ and the other with phases on the $(3,2)_A$ branch (light blue) near $\Phi_n \approx 0.6$. The

sleep onset phases of the sleep episodes are almost equal. Note that the unstable fixed points still exist at the right side of these map curves. This period-doubling bifurcation does not change ρ_{REM}.

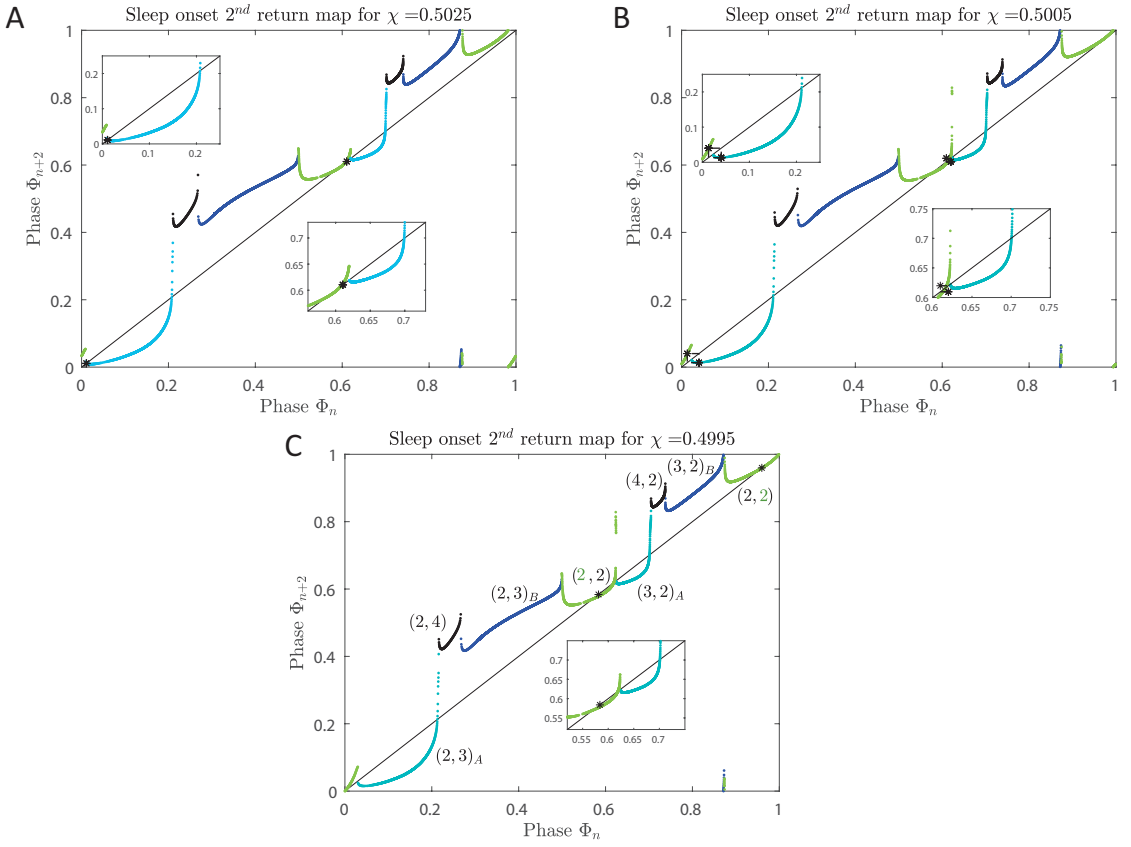

Figure 4.8: Higher order cycling solutions in the $\rho = \frac{1}{2}$ regime represented in the second return maps. The two insets in panels B and C show the 2-cycles associated with the sleep onsets in the stable solution occurring at earlier and later circadian phases. The behavior is qualitatively the same, thus we show only one inset in the remaining figures. The map branches are labelled according to the number of REM bouts involved in the sleep onsets with phase Φ_n and Φ_{n+1} in panel C. The light and dark blue, black and green branches correspond to model solutions involving 2 and 3, 2 and 4, and 2 and 2 REM bouts during their first two sleep episodes, respectively. A. Second return map for $\chi = 0.5025$ in the $\rho_{REM} = 2.5$ regime. The stable solution is characterized by higher order cycles after a period doubling bifurcation. B. Second return map for $\chi = 0.5005$ in the $\rho_{REM} = 2.25$ regime. The stable solution participates in a higher order cycle involving neighboring map branches. C. Second return map for $\chi = 0.4995$ in the $\rho_{REM} = 2$ regime. A saddle-node bifurcation introduces the stable solution with pattern $\{2_{(2,2)}\}^{\infty}$.

$\underline{\rho_{REM} = 2.25}$

As χ decreases a little further, ρ_{REM} decreases to 2.25 as the stable solution transitions to the pattern $\{2_{(2,2)}, 2_{(2,3)}\}^{\infty}$ for $\chi \in [0.5005, 0.501]$. In this solution, sleep onset phases alternate between neighboring map branches $(2,3)_A$ (or $(3,2)_A$, light blue) and $(2,2)$ (green) which appeared during the evolution of the map with χ (Figure 4.8B). Unlike the bifurcation sequences seen in the $\rho = 1$ regime, where higher order cycle solutions consisting of sleep onset phases on two distinct map branches follow a period-adding-type sequence, here only the $\{2_{(2,2)}, 2_{(2,3)}\}^{\infty}$ pattern persists with an abrupt transition to the $\{2_{(2,2)}\}^{\infty}$ solution (Figure 4.7A). This abrupt transition occurs in a border collision bifurcation at $\chi = 0.5005$ when the $(2,3)_A$ and $(3,2)_A$ (light blue) map branches intersect the diagonal, $\Phi_{n+2} = \Phi_n$, at the unstable fixed points lying on their leftmost side (Figure 4.8B).

$\underline{\rho_{REM} = 2}$

The stable $\{2_{(2,2)}\}^{\infty}$ solution is found at approximately $\chi = 0.4995$ as a result of a pair of saddle-node bifurcations via a tangent intersection of both $(2,2)$ (green) map curves with the diagonal (Figure 4.8C).

The saddle-node bifurcation creates two pairs of stable and unstable fixed points, one pair on each $(2,2)$ map branch. As before, as χ decreases further, the slope of map branches at the stable fixed points eventually decreases through -1 at $\chi = 0.462$ leading to a period-doubling bifurcation.

Evolution of map branches

Note that during this evolution of decreasing χ, the shape of the second return map has significantly changes compared to its structure at $\chi = 0.542$ (Figure 4.7B). In particular, for $\chi = 0.542$ the (2,4) and (4,2) branches existing on phase intervals $\Phi_n \in (0.1242, 0.2624)$ and $\Phi_n \in (0.6778, 0.764)$, respectively, correspond to trajectories

that generate sleep episodes involving four REM bouts (Figure 4.7B, black curves). As χ is reduced, and the homeostatic sleep drive varies at a higher rate affecting the total sleep time, the total number of REM bouts during a sleep episode decreases as well. The map reflects this phenomenon as the (2,4) and (4,2) branches exist over narrower Φ_n intervals and are eventually annihilated, while their neighboring $(2,3)_A$, $(2,3)_B$, $(3,2)_A$, $(3,2)_B$ branches on either side merge into continuous S-shaped (2,3) and (3,2) curves (Figure 4.9).

Reoccurrence of solutions with $\rho_{REM} > 2$

For $\chi <\approx 0.4875$, the second return map comprises curves that correspond to sleep cycles that involve only two or three REM bouts (Figure 4.9A). Stable period doubling orbits are obtained on the (2,2) (green) branches of the map for $\chi \in [0.4595, 0.462]$ (Figure 4.9B). For lower χ values, we obtain more stable higher order cycle solutions with sleep onset phases alternating between distinct map branches. Specifically, at $\chi = 0.4565$, a stable 6-cycle with the pattern of $\{2_{(2,3)}, 2_{(2,2)}, 2_{(2,2)}\}^{\infty}$ is observed with sleep onset phases on the $(2,2)$ (green) and on the S-shaped $(2,3)$ (or (3,2)) (blue) branches (Figure 4.9C). This pattern corresponds to $\rho_{REM} = \frac{13}{6}$ and loses stability at $\chi = 0.453$ where the higher order pattern $\{2_{(2,3)}, 2_{(2,2)}, 2_{(2,2)}, 2_{(2,3)}, 2_{(2,2)}, 2_{(2,2)}\}^{\infty}$ occurs. As χ decreases further, the stable sleep patterns visit the (2,2) (green) map branches less, and thus, the REM rotation number starts increasing incrementally from 2 in a period-adding type fashion.

As χ values approach the lower end of the $\rho = \frac{1}{2}$ regime, the $\rho_{REM} = 2.25$ solution with pattern $\{2_{(2,3)}, 2_{(2,2)}\}^{\infty}$ is introduced once more for $\chi \in [0.43, 0.4435]$ (Figure 4.9D).

In this occurrence of the solution, the phases of sleep episodes have shifted to the second half of the circadian day. That is, the earlier sleep onsets occur close the peak of the circadian rhythm and the later ones occur close to the trough of the circadian

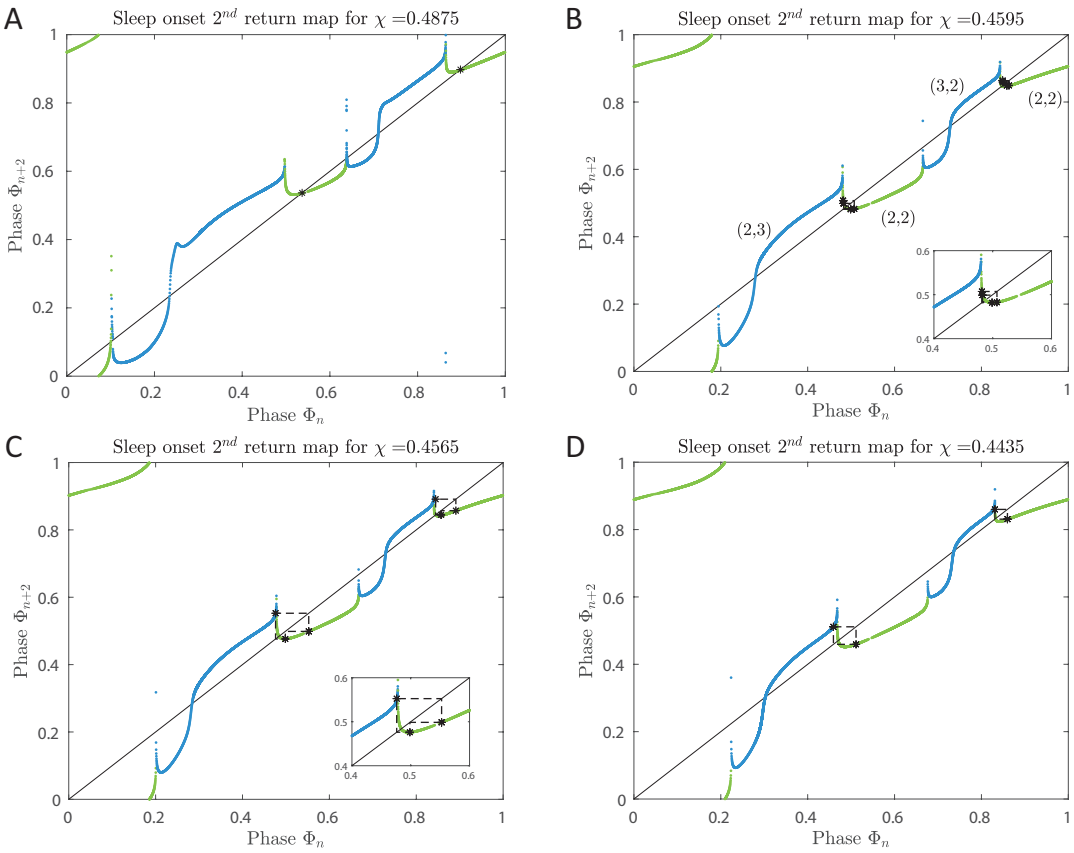

Figure 4.9: Second return maps capturing $\rho = \frac{1}{2}$ solutions with only two or three REM bouts per sleep episode. The maps deform and comprise only four branches corresponding to a distinct number of REM bouts. The map branches are labelled and colored according to the number of REM bouts involved in the sleep onsets with phase Φ_n and Φ_{n+1} in panel B. The light blue and green branches correspond to model solutions involving 2 and 3, and 2 and 2 REM bouts during the two sleep episodes, respectively. A. Second return map for $\chi = 0.4875$ exhibiting the annihilation of the branches involving sleep onset phases with four REM bouts. B. Second return map for $\chi = 0.4595$. The stable solution has $\rho_{REM} = 2$ and follows a period-doubling bifurcation. C. Second return map for $\chi = 0.4565$. The stable solution has $\rho_{REM} = \frac{13}{6}$ manifesting the monotonic increase of ρ_{REM} as χ is reduced. D. Second return map for $\chi = 0.4435$. The stable solution has $\rho_{REM} = \frac{9}{4}$ and alternates between the $(2,3)$ (or $(3,2)$) and $(2,2)$ map branches.

rhythm. As χ decreases further, a period doubling cascade from the $\{2_{(2,3)}, 2_{(2,2)}\}^{\infty}$ pattern occurs for $\chi \in [0.43, 0.431]$ (Figure E.2A in Appendix E).

Finally, as χ decreases out of the $\rho = \frac{1}{2}$ regime, the REM rotation number, ρ_{REM}, keeps increasing incrementally reflecting a period-adding-type sequence as more days with $2_{(2,3)}$ sleep cycles are added to the pattern with $2_{(2,2)}$ days. In the map, this

translates to more phase onsets in the higher order cycles lying on the S-shaped (2,3) and (3,2) (blue) branches.

At $\chi = 0.41$, a border collision at the unstable fixed points on each of the (2,2) (green) map branches designates the loss of stability of the $\rho = \frac{1}{2}$ solution (Figure E.2B in Appendix E). Given the structure of the map branches, no stable fixed points exist in the second return map and no higher order cycles can be created. As a result, sleep patterns with days involving three sleep episodes emerge.

Summary

In summary, the bifurcation sequence in the $\rho = \frac{1}{2}$ regime displays similarities with the $\rho = 1$ regime, including period doubling when fixed points lose stability due to a change in the slope of the map branch at the fixed point, creation of stable fixed points through saddle-node bifurcations, and higher order cycling solutions with period-adding-type patterns in ρ_{REM} involving sleep onset phases on distinct map branches. A large portion of this regime supports the existence of the $\rho = \frac{1}{2}$ solution not through fixed points, but higher order cycles around unstable fixed points. Thus, this regime shows more occurrences of the loss of unstable fixed points through border collision bifurcations that lead to transitions in solution patterns. Additionally, certain ρ_{REM} solutions in the interval [2,2.5] reoccur at different χ values. However, the size of the χ-interval for each occurrence of ρ_{REM} differs due to the asymmetrical shape of the map branches. Specifically, the higher order cycling solutions exist over larger χ values when the unstable fixed point that they surround lies on the left side of the map branch that has a longer vertical distance from its border associated with the cusp.

4.3.4 Loss of NREM-REM cycling in polyphasic sleep limit

The loss of existence of the $\rho = \frac{1}{2}$ solution initiates the appearance of circadian cycles with three sleep episodes. As χ decreases through these regimes ($\chi \in [0.2, 0.41]$), similar bifurcations, bistability regimes and disruptions of the ρ_{REM} period-adding structure take place leading up to the $\rho = \frac{1}{4}$ solution regime (Figure 4.1C). We note that NREM-REM cycling is restricted in the small χ limit because the timings of REM activation and REM bout duration do not scale with χ and the homeoestatic sleep drive time constants. However, we want to point out how model dynamics and map structure evolve as NREM-REM cycles are shortened when sleep episodes have shorter durations. We expect that these same trends would occur for faster time scales of NREM-REM cycling which would be more appropriate when sleep episodes get too short. But, we do not expect these results to be representative of actual polyphasic sleep patterns in other species where REM episodes can be very short.

As χ decreases and sleep episodes become shorter, the loss of multiple NREM-REM cycles weakens the influence of this cycling on sleep-wake dynamics. For example, the average number of REM bouts per sleep reduces to 1 for $\chi \in [0.099, 0.226]$ which encompasses the regime where $\rho = \frac{1}{4}$ solutions are stable ($\chi \in [0.205, 0.2185]$). When solutions have only one REM bout per sleep episode, it always occurs at the end of the sleep episode at the transition from the sleep and to the wake state. In this way, the timing of the REM bout is constrained within the sleep episode, and the occurrence of REM sleep is influenced primarily by the timing of wake onset. In this regime, the map becomes continuous, and gain and loss of stability of the $\rho = \frac{1}{4}$ solution occurs due to saddle-node bifurcations at $\chi = 0.2185$ and 0.205, respectively (Figure 4.10A,B).

In both the two- and three-state models, a significant reduction in the homeostatic time constants leads to the transition to a regime where the map is continuous [147, 14, 10], resulting in a regime where no border collision bifurcations can occur.

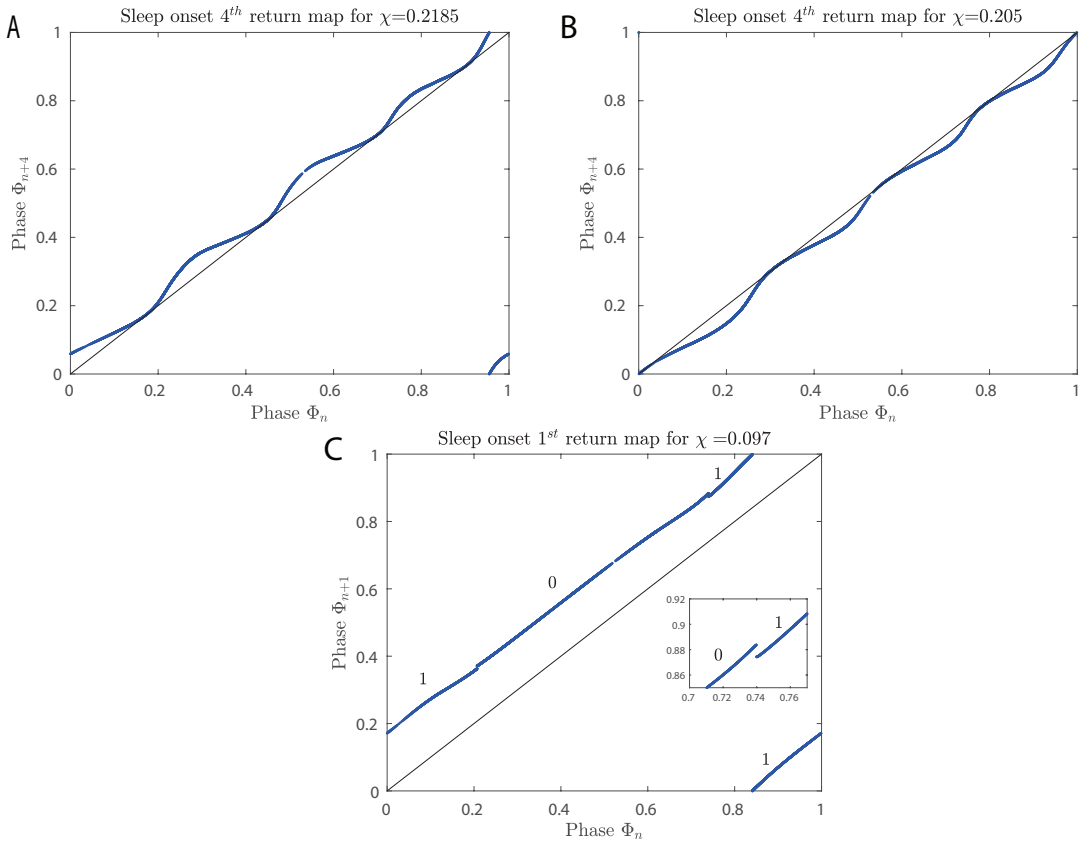

Figure 4.10: Maps showing the transition from a continuous to a discontinuous regime. A. The fourth return map for $\chi = 0.2185$ designates the beginning of the $\rho = \frac{1}{4}$ solution. The map is continuous in this regime, and thus, the stable solution emerges in a saddle-node bifurcation. B. The fourth return map for $\chi = 0.205$ demonstrating the loss of existence of the $\rho = \frac{1}{4}$ solution. The map remains continuous and thus, the stable solution ceases to exist in a saddle-node bifurcation. C. The first return map for $\chi = 0.097$. Occurrence of solutions with one or no REM bouts due to the fast time scales of the homeostatic sleep drive lead to the reappearance of discontinuities in the map. Each discontinuity exists to differentiate between map branches that correspond to sleep episodes with different number of REM bouts. The branches are labelled according to the number of REM bouts involved in the initial sleep occurring at phase, Φ_n.

In this continuous regime, the homeostatic sleep drive time scale is faster than the time scale of the circadian drive at all phases. Thus, grazing bifurcations that led to discontinuities in the map at phases when the circadian drive was evolving faster than the sleep homeostat, do not occur anymore. In the three-state model, there is an additional requirement for the map to be continuous; the average number of REM bouts per sleep should not differ between distinct sleep episodes. Therefore, in the three-state model discontinuities can reappear in the map as χ is decreased further when the number of REM bouts at different circadian phases is distinct. Here, this occurs due to the occurrence of sleep episodes with either 1 or 0 REM bouts (Figure 4.10C). This is in contrast to studies analyzing two-state models that suggest that once the map becomes continuous, continuity is preserved as model parameters are further varied in the same fashion.

4.4 Discussion

In this chapter, we investigated the role of NREM-REM cycling in sleep patterning generated by varying homeostatic time constants in a sleep-wake network model that simulates three states: wake, NREM sleep, and REM sleep. We found that increasing the rates of growth and decay of homeostatic sleep need resulted in a transition from monophasic to polyphasic sleep suggesting that more frequent sleep periods are associated with more rapid build up of sleep need. This finding is consistent with the experimental characterization of the time constants of the homeostat in multiple mammalian species [124, 155] and in different human life stages [2, 84, 86]. The Two-Process Model and other physiologically-based models that simulate only two states, wake and sleep, without differentiating between REM and NREM sleep [124, 147, 10] (see Chapter III) have also analyzed the transition from monophasic to polyphasic sleep patterns, as the homeostatic time constants were reduced (or an equivalent parameter varied). As this transition takes place, an underlying period

adding structure in the average number of sleep cycles per day was observed. Results in the two-state models suggest a strict monotonic change associated with this structure. We have shown, however, that this monotonic change is disrupted when the dynamics associated with NREM-REM cycling are included in the model. Specifically, the three-state model allows for more complicated transitions as solutions evolve from monophasic to biphasic sleep patterns, including intervals of bistability, as well as diversity of solutions with varied patterns of NREM-REM cycling across the same number of daily sleep episodes.

Bifurcations in sleep onset maps

We presented a computationally-based analysis of changes in sleep patterning and investigated the bifurcations that produce these changes using a piecewise continuous one-dimensional circle map. The map was constructed numerically from a high-dimensional, physiologically-based sleep-wake regulatory network model for human sleep [53]. The map is non-monotonic, noninvertible and characterized by discontinuities separating branches that correspond to solutions with distinct REM bout patterns. The particular map structure predicts the transitions in the numbers of average sleep cycles per day as homeostatic time constants are varied. Simultaneously, one can determine the number of REM bouts associated with stable solutions by cobwebbing on the map and tracking which map branches are visited by the solution. Changes in the average number of sleep cycles per day and the associated REM patterns result from sequences of period doubling, saddle-node and border collision bifurcations.

Specifically, we have shown that decreasing the homeostatic time constants in the model causes the stable fixed point corresponding to entrained monophasic ($\rho = 1$) sleep-wake behavior to first lose stability and then lose existence by moving through a discontinuity of the map. The change in stability of the fixed point results in the

emergence of higher-order cycles in a period doubling bifurcation and a transition in the REM patterns (quantified by ρ_{REM}) is observed. Saddle-node bifurcations initiate the existence of stable solutions with fixed daily numbers of REM bouts, and border collisions lead to the destruction of unstable fixed points and higher order cycles. The solutions obtained in saddle-node bifurcations correspond to monophasic sleep-wake behavior with incrementally increased number of REM bouts. These can coexist with higher order cycles whose REM patterns can be determined by cobwebbing on the associated neighboring map branches around the cusps of the map branches.

Our results show that generally similar bifurcation sequences take place in regimes with multiple sleeps per day (ρ less than 1) as homeostatic time constants decrease. However, NREM-REM cycling can be more variable and not show an incremental period-adding type increase in the number of daily REM episodes, quantified by ρ_{REM}. Specifically, when multiple daily sleep episodes occur the distribution of the number of REM bouts across the sleep episodes can vary, leading to multiple patterns of NREM-REM cycling exhibiting the same ρ_{REM} value. Additionally, as we analyzed for biphasic ($\rho = \frac{1}{2}$) sleep, the number of daily REM bouts can show incremental decreases and incremental increases in different ranges of the homeostatic time constant caused by sequences of bifurcations in higher order cycling solutions and saddle-node bifurcations.

Contrast with two-state sleep-wake models

The observed nested hierarchy of bifurcations that take place in sleep patterns with homeostatic variation under the scaling parameter, χ, is a consequence of accounting for the NREM-REM cycling that occurs during sleep. Circle maps have been employed in two-state models to analyze bifurcation phenomena associated with the transition to consolidated sleep. In particular, the dynamics of the Two-Process model have been reduced to a one-dimensional map that is piecewise smooth and may be monotonic or

non-monotonic depending on parameter regimes [118, 147, 14]. Similarly-structured maps have been computed numerically for other two-state models [10]. However, these maps mainly account for the circadian effect on the timing of sleep onset, which may result in a large time separation of nearby solutions. This phenomenon is reflected in a large discontinuity close to peak values of the circadian rhythm, which is also captured in the maps computed for the three state model, e.g at $\Phi_n \approx 0.5$ for $\chi = 1$ (Figure 2.6).

Studies in two-state models have reported border collision and saddle-node bifurcations as a mechanism of creating or destroying stable and unstable fixed points in the map and thus, causing the transition in sleep patterning. However, to our knowledge, regimes of bistability or period doubling solutions have not been reported in the two-state models. In our three-state model, the existence of these regimes is associated with the increased complexity of the map structure caused by differences in NREM-REM cycling at distinct circadian phases. This suggests that there may be important aspects of the transition from polyphasic to monophasic sleep that are not captured by two-state models.

For example, in our model, a change in the number of REM bouts leads to a change in the duration of the sleep episode and its circadian onset phase. Additionally, the propensity for REM bouts to occur varies with the circadian rhythm [71], consistent with experimental characterizations of REM sleep propensity [37]. Thus, as χ varies, the interaction between circadian and homeostatic processes leads to changes in the timing and duration of sleep episodes which, in turn, interact with the NREM-REM cycling dynamics within the sleep episode. The distribution of REM bouts in each sleep episode varies for different values of χ, leading to patterns with different average numbers of REM bouts per sleep (that is different REM rotation numbers, ρ_{REM}), but same average numbers of sleep cycles per day, ρ. In some cases, we found patterns with the same ρ and ρ_{REM}, but distinct NREM-REM cycling sequences. This dependence

of NREM-REM cycling on circadian phase is consistent with experimental evidence examining NREM-REM cycling in preschool children [102].

Implications, limitations and future considerations

Our modeling approach also incorporates the effect of light on sleep timing during the transition from monophasic to polyphasic regimes. In our analysis, the map construction requires that we assume a fixed light:dark schedule based on environmental light in order to maintain a rigorous definition of circadian phase. However, the light exposure of most humans does not occur at a constant intensity and is not strictly dependent on the environmental light cycle. Instead, individuals experience a wide range of light intensities, and artificial light enables a significant level of self-selection in light exposure that may result in variable daily schedules of both light exposure and sleep-wake behavior [148, 149, 105]. In the model, manipulations of light levels, such as those arising from behavioral gating of light as occurs when eyes are closed, give rise to feedback between sleep timing and light input to the circadian clock, which then can affect circadian phase. In previous work we have shown that the map maintains a good approximation of the dynamics of the full model even when behaviorally-gated light input is included [128]. Thus, we expect that results reported here are qualitatively similar to those that would be obtained if light:dark schedules were allowed to vary with simulated behavioral state.

In adults, REM sleep is gated by the circadian system [37], but circadian and other features of REM sleep differ across species and in humans at different life stages [121, 145, 154]. Therefore, the role of REM sleep should be considered when analyzing sleep-wake dynamics, particularly during transitions from biphasic to monophasic sleep as occur with the dropping of naps in early childhood. Future work is needed to assess model predictions by characterizing concurrent changes in REM sleep and the dynamics of homeostatic sleep need across qualitative transitions in sleep-wake

behavior. In addition, the reciprocal interaction hypothesis incorporated to capture the REM sleep dynamics is one of multiple proposed mechanisms for REM generation and therefore, should be reassessed as sleep research makes steps in determining appropriate mechanisms.

Since changes in homeostatic time constants may not be uniform for the increase and dissipation of sleep need [87], it will also be important to investigate the consequences of separately altering the rates of homeostatic growth and decay to provide physiological constraints for model parameters and allow assessment of the contribution of homeostat dynamics to changes in sleep patterning. Other factors, including circadian influences on sleep and on ultradian cycling between NREM and REM sleep, likely also impact observed changes in sleep-wake patterning. Future modeling work investigating the relative contributions of these factors would complement ongoing experimental studies of sleep across development.

CHAPTER V

Data-driven Modeling of Sleep Patterns in Preschool Children

5.1 Introduction

Early childhood is characterized by a transition from highly variable polyphasic to monophasic sleep behaviors (see Chapter I for more details). By the age of 2 years most children exhibit a biphasic pattern that includes a long nocturnal sleep and a short nap in the middle of the day [84]. As children develop, the duration and frequency of the naps may decrease until they adopt a sleep schedule that involves a single nighttime sleep. The majority of 5 year old children exhibits a monophasic sleep pattern [2].

This transition is mediated developmentally. Properties of the homeostatic sleep drive, one of the main processes dictating the timing and types of sleep patterns, change with development. In particular, experimental studies have shown a change with age in the values of the time constants associated with the rise and decline of the sleep homeostat, as well as differences between lower and upper asymptotes of the homeostat [101]. For example, the rise time constant of the sleep homeostat increases between the ages of 2 and 5 years old, and can lead to longer wake bouts. Behaviorally, however, the transition from a non-napping to a napping sleep schedule

is highly variable and can be rather challenging. Additionally, caregivers may influence the transition. Namely, they might promote a non-napping behavior or maintain a napping behavior if children show signs of sleepiness or mood changes [21].

In Chapters III and IV, we considered a scaling of the homeostatic time constants which was a sufficient mechanism for generating a transition between polyphasic and monophasic sleep patterns in our physiologically-based sleep-wake models. More specifically, we found regimes of the scaling parameter that capture the transition from biphasic to monophasic sleep. However, the sleep episodes of the patterns produced may not occur at phases appropriate to characterize sleep behavior in early childhood. Here, we we incorporate the experimentally estimated values of homeostatic parameters determined for 2-year and 5-year old children reported in [101] into our SWFF model and determine parameter sets that generate biphasic and monophasic sleep patterns consistent with experimental data on sleep timings in young children [4].

Although homeostatic parameters have been estimated for these age groups, the manner at which they vary between the ages of 2 and 5 years is not known and may differ across individuals. In this work, we consider a subset of model parameters that are developmentally regulated, including the homeostatic parameters, and investigate the effects of different variations of the parameters that produce distinct transitions from biphasic to monophasic sleep. Furthermore, we investigate the effect of external light schedules on sleep patterns that may promote or suppress napping in this transition process.

This chapter[1] is organized as follows: in Section 5.2 we introduce the experimental data employed to determine the light schedules and characteristics of sleep patterns for the 2- and 5-year olds, as well as how these will be incorporated in the SWFF model. In Section 5.3 we present our findings. Finally, in Section 5.4 we give a brief overview of our results and discuss future directions.

[1]This work is joint with Shelby Stowe, Department of Applied Mathematics & Statistics, Colorado School of Mines.

5.2 Experimental data and mathematical model

We employ the sleep-wake flip-flop (SWFF) model described in detail in Chapter II to produce sleep patterns in early childhood consistent with metrics based on [4]. Akacem et al. provide detailed statistics for circadian and sleep measures in toddlers that exhibit a napping and a non-napping behavior (Figure 5.1). Our primary measures for comparing characteristics of model solutions to the data are the durations of sleep and wake episodes, as well as the circadian phases of their onsets and offsets. The circadian phase, Φ, of an event of interest (e.g. sleep onset) is defined as follows:

$$\Phi = \frac{\text{Time of event (min)} - \text{Time of preceding circadian minimum (min)}}{1440 \text{ (min)}}$$

To compute the circadian phases associated with the data, we use the published relationship between the dim light melatonin onset (DLMO) and the minimum of the circadian rhythm which is based on core body temperature (CBT) measurements: DLMO=CBT_{min}-7 (hours) [32, 19]. This calculation provides ranges of circadian phases based on the data (Table 5.1). Note that all phases have been computed using the mean values of DLMO times in Figure 5.1. The nap onset (offset) time was computed by subtracting (adding) half of the mean nap duration from (to) the range of nap midpoint times.

	Napping	**Non-Napping**
Sleep onset	0.7521± 0.0299	0.7375±0.0208
Wake onset	0.1736±0.0208	0.2063±0.0285
Nap onset	0.4604±0.032	x
Nap offset	0.5313±0.0319	x

Table 5.1: Ranges of circadian phases for sleep behaviors based on the data computed using the relationship DLMO=CBT_{min}-7 to establish the time of the circadian minimum.

An additional motivation for this work is to investigate how exposure to different

	Napping	Non-Napping	Statistics		
	(n = 15)	(n = 5)	*t*	*d*	*p*
Circadian Variables					
Dim Light Melatonin Onset Time	19:48 ± 0:42	19:10 ± 0:33	1.81	0.93	0.044
Bedtime Phase Difference (min)§	30.4 ± 33.9	25.0 ± 41.1	-0.29	0.15	0.773
Sleep Onset Phase Difference (min) §	63.9 ± 32.5	42.0 ± 42.0	-1.22	0.63	0.240
Midsleep Phase Difference (min) §	367.0 ± 28.6	379.6 ± 25.3	-0.87	0.45	0.394
Wake Time Phase Difference (min) §	670.1 ± 39.9	717.1 ± 33.1	-2.37	1.23	0.029
Sleep Variables					
Bedtime	20:18 ± 0:36	19:35 ± 0:30	2.42	1.24	0.014
Sleep Onset Time	20:51 ± 0:43	19:52 ± 0:30	2.84	1.46	0.006
Midsleep Time	1:54 ± 0:30	1:30 ± 0:23	1.65	0.85	0.058
Wake Time§	6:58 ± 0:30	7:07 ± 0:41	-0.57	0.30	0.575
Sleep Onset Latency (min)	33.0 ± 16.6	17.1 ± 10.2	-2.01	1.03	0.030
Nighttime Time in Bed (min)	656.9 ± 38.9	705.6 ± 51.9	-2.24	1.16	0.019
Nighttime Sleep Duration (min)	606.3 ± 43.9	675.0 ± 56.2	-2.84	1.47	0.006
24-h Sleep Duration (min) §	708.9 ± 40.2	675.0 ± 56.2	1.48	0.76	0.156
Days Napping (of 5)	3.6 ± 1.2	-	-	-	-
Nap Midpoint Time	14:43 ± 0:46	-	-	-	-
Nap Duration (min)	102.6 ± 20.1	-	-	-	-

Statistics are shown for independent t-tests (napping versus non-napping participants).
§ indicates a two-tailed test.

doi:10.1371/journal.pone.0125181.t001

Figure 5.1: Statistics regarding circadian and sleep measures in napping and non-napping toddlers shown in Table 1 of [4].

external light schedules or photoperiods may influence sleep-wake behavior. Here, we consider two forced light schedules which we refer to as the napping and the non-napping light schedule.

The non-napping light schedule reflects a monophasic sleep pattern. In particular, lights are on (1000 lux) during the wakefulness period, while lights are off (0 lux) at bedtime. The napping schedule includes an additional period during which the lights are dimmed (10 lux) to reflect a nap in the middle of the day. In Figure 5.2, we show a graphical representation of the non-napping (top panel) and napping (bottom panel) light schedules. The timing and duration of the different light intensities are based on the sleep behavior data from Table 1 in [4] (Figure 5.1). Specifically, to compute the onset and offset of the dim lights (10 lux) in the napping light schedule, we subtract and add half of the mean nap duration from the mean nap midpoint, respectively.

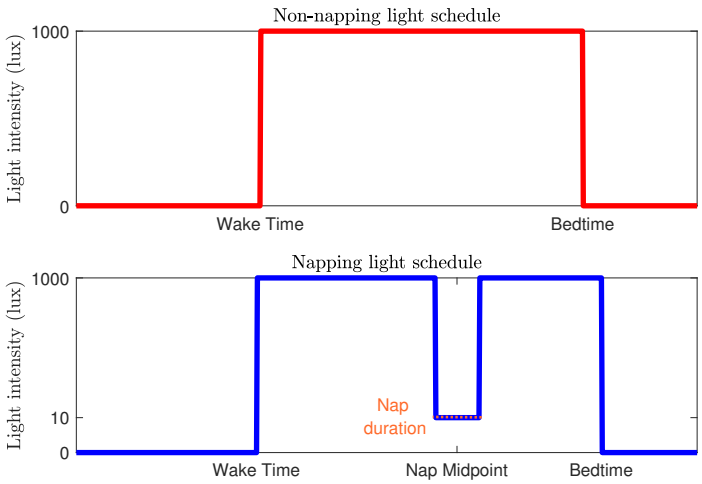

Figure 5.2: Graphical representation of the non-napping (top) and napping (bottom) light schedules. The y-axis indicates the range of light intensity values (in lux) for each schedule. Timings and durations of light are based on the sleep behavior measures in Table 1 of [4] as labeled on the x-axis.

We have modified the circadian component of the SWFF model as follows:

1. The steady state response function equation for the firing rate of the neurons in the Suprachiasmatic Nucleus (SCN) population is:

$$SCN_{\infty}(c) = SCN_{max} \cdot 0.5 \cdot \left(\mathbf{1.21} + \tanh\left(\frac{c - \beta_{SCN}}{\alpha_{SCN}} \right) \right) . \tag{5.1}$$

2. The circadian drive c (the input of equation 5.1) is the output of the Forger et. al limit cycle model [64] introduced in Chapter II. This allows us to incorporate the effect of light exposure, since light intensity is the primary input to this circadian oscillator model.

5.3 Results

For our analysis, we first identify the parameter sets that appropriately capture the napping and non-napping behavior in early childhood described in [4]. The two parameter sets employ the napping and non-napping light schedules for the biphasic

and monophasic sleep-wake behavior, respectively, described in Section 5.2. We then consider various ways in which model parameters can vary between their values associated with the two behaviors and investigate the effect of the light schedules in the transition from biphasic to monophasic sleep patterns.

Properties of the homeostatic sleep drive have been implicated to vary with development [101, 87]. In particular, the time constants and asymptotes for homeostatic sleep pressure have been estimated in adults and children [101]. Additionally, previous mathematical analysis has established that scaling the time constants associated with the rates of increase and dissipation of homeostatic sleep pressure can lead to the transition from polyphasic to monophasic sleep (see Chapters III, IV and [14]). For our model parameter sets, we constrain the values of sleep-homeostat associated parameters (h_{max}, h_{min}, τ_{hw}, τ_{hs}) to experimental values estimated for children of age 2 (nappers) and 5 (non-nappers) years old [101]. In addition, parameters that determine the model's response to the sleep homeostat, i.e. k_1 and k_2, were optimized to capture napping and non-napping behavior. All other parameters were fixed.

5.3.1 Napping and non-napping parameter sets

For our SWFF model, we identified the parameter sets shown in Table 5.2 that generate stable biphasic and monophasic sleep patterns that are comparable to the experimental data in [4] regarding the timing of sleep and wake cycles in 2- and 5-year olds (see Figure 5.1 and Table 5.1).

Specifically, the parameter values shown in black color for the parameters in bold font in Table 5.2 with the napping light schedule generates a stable model solution of a biphasic sleep pattern (Figure 5.3A,C,E). We will refer to this parameter set as the "2-year old parameter set". The SWFF model generates a nap during the dim light period (gray bars in panels A,C,E of Figure 5.3) and a longer nighttime sleep during the dark (lights off) period (black bars in panels A,C,E of Figure 5.3). In particular,

the wake, nap and sleep onset phases are 0.1620, 0.4668 and 0.7378, respectively. The nap offset phase is 0.542. The nighttime sleep duration is 611 minutes, while the nap lasts 108 minutes. The early wake episode duration is 439 minutes, while the late wake episode (after the nap) duration is 282 minutes. These values compare well with the phases and durations calculated from the data in Table 5.1.

On the other hand, choosing the parameter set with values in blue color for the parameters in bold font, and the non-napping light schedule generates a monophasic sleep pattern that corresponds to 5-year old sleep, called the "5 year old parameter set" (Figure 5.3B,D,F). The SWFF model generates a nighttime sleep during the dark (lights off) period (black bars in panels B,D,F of Figure 5.3) and the system transitions to wake during the lights on period (white background in panels B,D,F of Figure 5.3). The wake and sleep onset phases are 0.2066 and 0.7368, respectively. The durations of the corresponding wake and sleep episodes are 764 and 676 minutes, respectively. These values of phases and durations are close to the means of the corresponding data values shown in Table 5.1.

$W_{max} = 6$ Hz	$\tau_W = 23$	$\alpha_W = 0.5$	$\beta_W = -0.34$
$S_{max} = 6$ Hz	$\tau_S = 10$	$\alpha_S = 0.175$	
$SCN_{max} = 5.95$ Hz	$\tau_{SCN} = 0.5$	$\alpha_{SCN} = 0.25$	$\beta_{SCN} = -0.05$
$g_{sw} = 0.32$	$g_{scnw} = 0.08$	$g_{ws} = 0.12$	$g_{scns} = 0.1$
$\boldsymbol{h_{max}} = 320$ 413	$\boldsymbol{h_{min}} = 8$ 20	$\boldsymbol{\tau_{hw}} = 7.95$ 14.4 hr	$\boldsymbol{\tau_{hs}} = 2.15$ 1.9 hr
$\boldsymbol{k_1} = -0.04$	$\boldsymbol{k_2} = -0.0065$ -0.0048	$\theta_W = 2$ Hz	

Table 5.2: Parameter sets that generate napping (2 year old) and non-napping (5 year old) behavior in the SWFF model. Parameters that may vary across the two sets are in bold and the 2- and 5-year old values are given in black and blue, respectively (if distinct). For $X = W, S, SCN$, τ_X are the time constants of the neuronal firing rates in minutes, and α_X and β_X are in units of effective synaptic input. Additionally, for $Y = W, S$, g_{XY} (where $X \neq Y$) has units of (effective synaptic input / Hz). Units for h_{max} and h_{min} are percentage mean SWA. The parameters k_1 and k_2 are measured in effective synaptic input and effective synaptic input/(% mean SWA), respectively. The remaining units are included in the table.

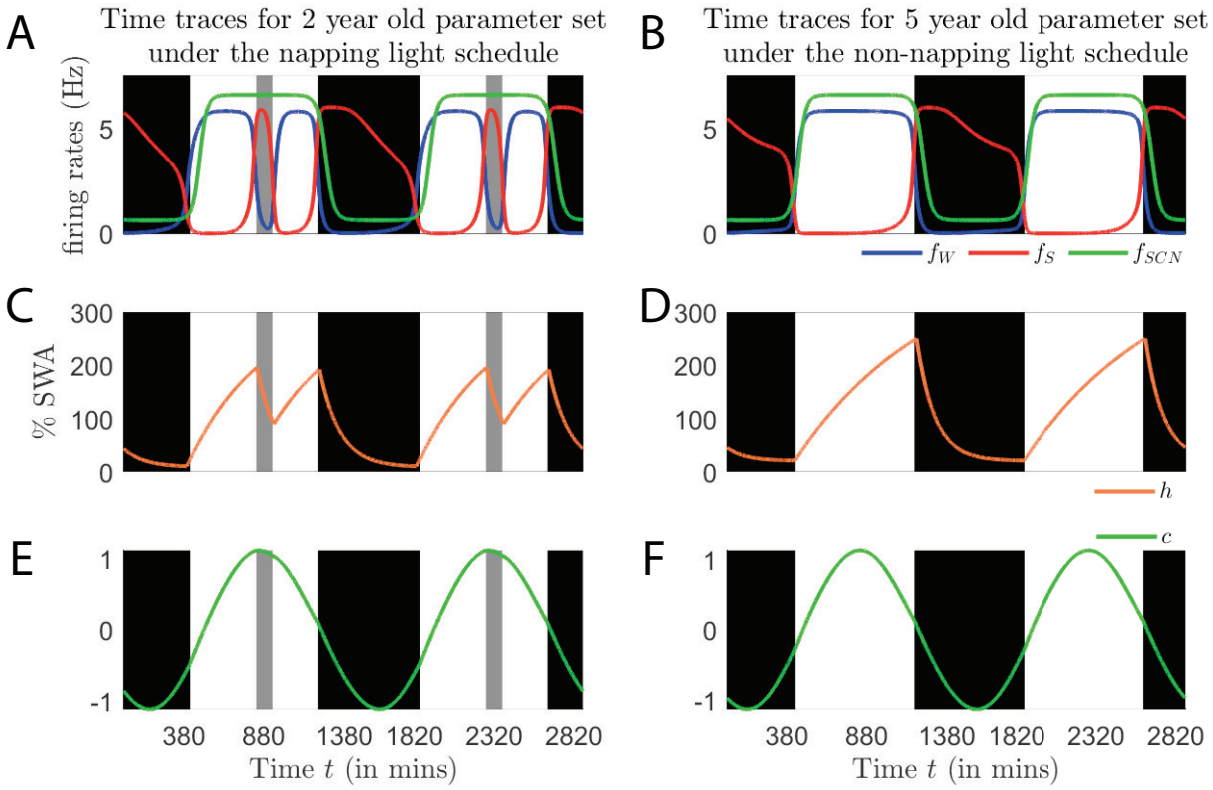

Figure 5.3: Time traces of the SWFF model for the 2-year and 5-year old parameter sets. A,C,E: Time traces of the neuronal populations f_W (blue), f_S (red), f_{SCN} (green) (A), homeostatic sleep drive h (C) and circadian drive c (E) using the 2-year old parameter set and the napping light schedule. The SWFF model generates a sleep pattern involving a nap during the dim light period (gray bar) and a longer nighttime sleep during the dark period (black bar). B,D,F: Time traces of the neuronal populations f_W (blue), f_S (red), f_{SCN} (green) (B), homeostatic sleep drive h (D) and circadian drive c (F) using the 5-year old parameter set and the non-napping light schedule. The SWFF model generates a monophasic sleep pattern involving a nighttime sleep during the dark period (black bar).

5.3.2 Transitioning between the two parameter sets

As toddlers age, features of sleep homeostasis may vary [101]. This variation may be distinct across individuals making the transition from biphasic to monophasic sleep more or less challenging. Motivated by expected developmental changes, we first study how transitioning from the 2-year old (napping) to the 5-year old (non-napping) parameter sets (parameters in bold font in Table 5.2) affects the sleep patterns generated by the SWFF model. We describe the evolution of h_{max}, h_{min},

τ_{hw}, τ_{hs}, and k_2 between the 2- and the 5-year old parameter sets using quadratic or sigmoid functions, since it is unknown how these parameters may actually vary (Figure 5.4). Moreover, we incorporate values for the homeostatic parameters in the range estimated in 3-year old children [101]. In particular, for a homeostatic parameter with values p_2 and p_5 in the 2- and the 5-year old parameter set, respectively, and p_3 in the estimated range at the age of 3 years, we define $F(\lambda; p_2, p_3, p_5)$, so that when $\lambda = 0$, we obtain the 2-year old, napping parameter set, and when $\lambda = 1$, we obtain the 5-year old, non-napping parameter set. Moreover, at $\lambda = 1/3$, we obtain p_3. This is an arbitrary choice, but it allows us to associate the parameter λ with age, as we ensure that at $\lambda = 1/3$ the homeostatic parameters will attain values corresponding to 3-year old children.

For each homeostatic parameter, we choose p_3 from representative values in their 3-year old range [101]. In particular, we choose three values corresponding to the mean and mean $\pm$ one standard deviation, when these values do not exceed the 2- and 5-year old parameter values. Otherwise, we choose values in the intersection of the 3-year old data and the interval defined by the 2- and 5-year old parameter set, so that we preserve the trend in which the homeostatic parameters vary.

To our knowledge, the way in which the sensitivity to the homeostatic sleep drive, which is captured by the parameter k_2 in our model, varies across development has not been established. Therefore, we model k_2 as a sigmoid function that increases from its 2- to its 5-year old value with λ, namely $k_2(\lambda) = A_{k_2} \tanh\left(\frac{\lambda}{\alpha_{k_2}}\right) + B_{k_2}$ (Figure 5.4D). The parameter α_{k_2} modulates how fast k_2 saturates to the value in the 5-year old parameter set.

To quantify the sleep patterns produced as λ varies from 0 to 1, we use the rotation number $\rho = \frac{q}{p}$, where p is the number of sleeps that occur in q circadian days. The algorithm and properties of this rotation number are described in detail in Chapter III (and IV). The λ interval [0,1] is divided in subintervals of size 0.002. We, then,

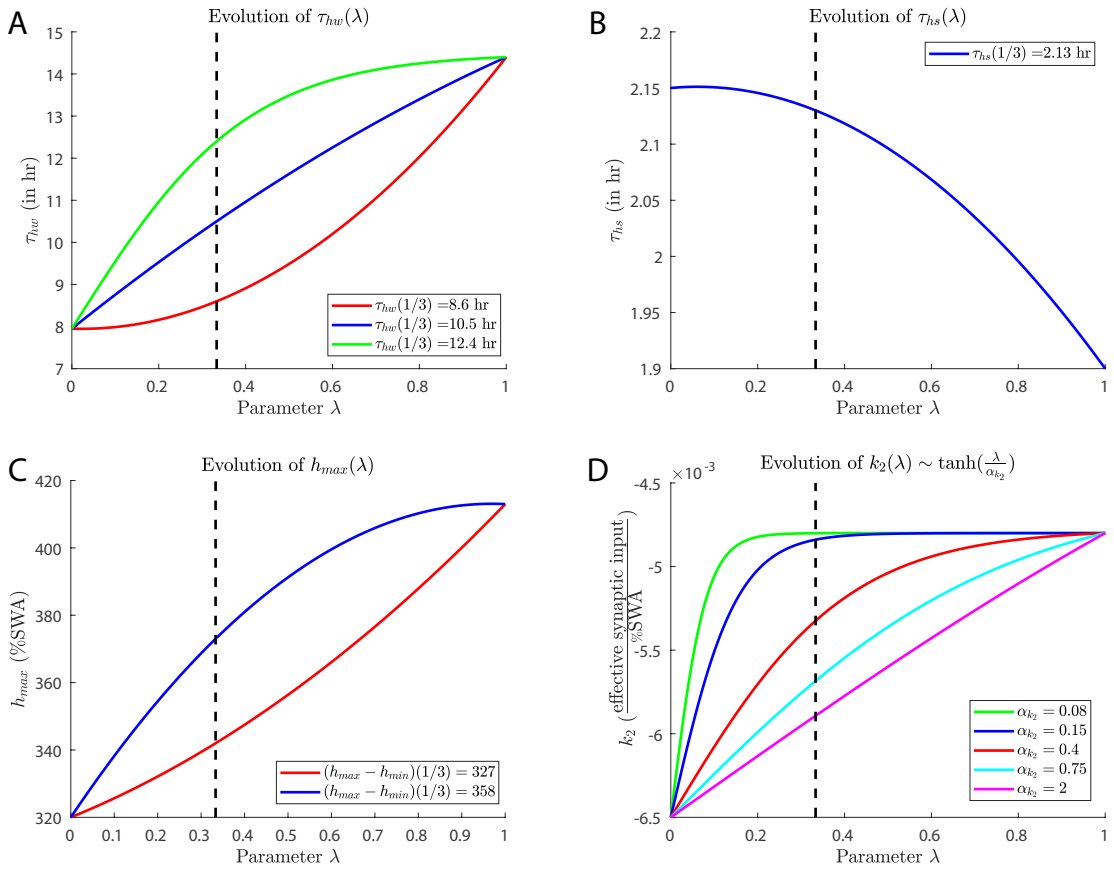

Figure 5.4: Evolution trajectories of homeostatic parameters, τ_{hw}, τ_{hs}, h_{max}, and the sensitivity to the homeostatic sleep drive, k_2 with respect to λ. The black dashed line corresponds to $\lambda = 1/3$. A. Evolution of τ_{hw} as a function of λ. As λ increases τ_{hw} increases from its 2-year old to its 5-year old value, while at $\lambda = 1/3$ it attains the values 8.6 hr (red curve), 10.5 hr (blue curve) and 12.4 hr (green curve) in the 3-year old range. B. Evolution of τ_{hs} as a function of λ. As λ increases τ_{hs} increases from its 2-year old to its 5-year old value, while at $\lambda = 1/3$ it attains the values 2.13 hr in the 3-year old range. C. Evolution of h_{max} as a function of λ. As λ increases h_{max} increases from its 2-year old to its 5-year old value, while at $\lambda = 1/3$ it attains the values 327 % SWA (red curve) and 358 % SWA (blue curve) in the 3-year old range. D. Evolution of k_2 as a function of λ. As λ increases k_2 increases from its 2-year old to its 5-year old value. Different values of α_{k_2} dictate the rate at which k_2 saturates to its 5-year old value. Smaller values of α_{k_2} correspond to a more rapid saturation.

compare the bifurcation diagrams for ρ produced under the napping and non-napping light schedules to determine how they influence the changes in sleep patterning.

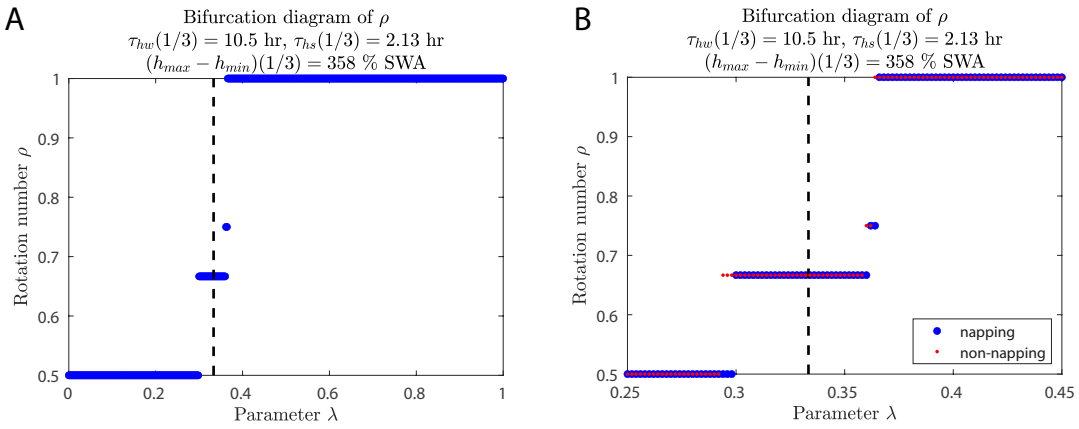

Figure 5.5: Bifurcation diagrams of ρ demonstrating the evolution of the rotation number as parameters are varied with respect to λ under different light schedules, so that at $\lambda = 1/3$, $\tau_{hw} = 10.5$ hr, $\tau_{hs} = 2.13$ hr, and $h_{max} - h_{min} = 358$ % SWA, all in the 3-year old range. The value of α_{k_2} is 0.15. A. The bifurcation diagram of ρ under the napping light schedule shows that the $\rho = \frac{1}{2}$ solution loses stability for $\lambda = 0.33$ and the $\rho = 1$ solution gains stability for $\lambda = 0.342$. During the transition from biphasic to monophasic sleep, not many intermediate solutions are attained. B. The bifurcation diagrams of ρ under the napping (blue) and non-napping (red) light schedules for $\lambda \in [0.3, 0.4]$. Imposing the non-napping light schedule leads to a similar transition from biphasic to monophasic sleep as λ increases. However, the value of λ at which the $\rho = \frac{1}{2}$ ceases to exist is smaller, namely 0.326. Additionally, the $\rho = 1$ solution also gains stability at a smaller value of λ, namely 0.34.

As shown in Figure 5.5A, increasing λ from 0 to 1 leads to the transition from biphasic to monophasic sleep patterns. Specifically, the rotation number, ρ increases from $\frac{1}{2}$ (2 sleeps per day) to 1 (1 sleep per day), and attains the $\rho = \frac{2}{3}$ solution in the Farey sequence for $\lambda \in (0.298, 0.366)$. The napping light schedule was applied during this simulation. Therefore, changes in the features of the homeostatic sleep drive, h, and the sensitivity of the model to it (k_2) manifest a change in sleep-wake behavior, although the light schedule promotes a napping behavior. At $\lambda = \frac{1}{3}$, corresponding to the the 3-year old range of homeostatic parameters, the sleep pattern generated alternates between days with a nap and days without a nap.

Light schedules may influence the transition from biphasic to monophasic sleep

A similar bifurcation diagram of the rotation number, ρ is obtained when simulating the model using the non-napping light schedule for $\lambda \in [0, 1]$ (Figure 5.5B). However, the value of λ at which the $\rho = \frac{1}{2}$ solution ceases to exist is slightly smaller, namely 0.292. Additionally, the $\rho = 1$ solution gains stability at a smaller value of λ, namely 0.364. This implies that imposing a different forced light schedule may slightly influence the transition from biphasic to monophasic sleep. In particular, $\lambda \in [0.292, 0.366]$ corresponds to an interval, in which our sleep-wake model could converge to a different stable solution, and thus, capture a different sleep pattern, depending on the light schedule we choose to enforce. Our results indicate that the non-napping light schedule promotes the transition to the monophasic regime, while a forced napping light schedule maintains a pattern with an average number of two sleeps per day for longer, as λ increases.

5.3.3 Homeostatic dynamics influence the transition from napping to non-napping behavior

Interindividual differences play an important role in the changes observed in sleep patterns with development. Mathematically, a different choice for the values of the homeostatic parameter at $\lambda = 1/3$, denoting the 3-year old age mark, may generate a different transition scenario. In this section, we consider the different τ_{hw} trajectories (see Figure 5.4A), while we choose a single variation for the remaining parameters. In particular, we let $\alpha_{k_2} = 0.15$ (blue trajectory in Figure 5.4D) and set h_{max} to follow the blue curve in Figure 5.4C. Figure 5.6 shows the bifurcation diagrams of ρ under these conditions for the different τ_{hw} evolution curves.

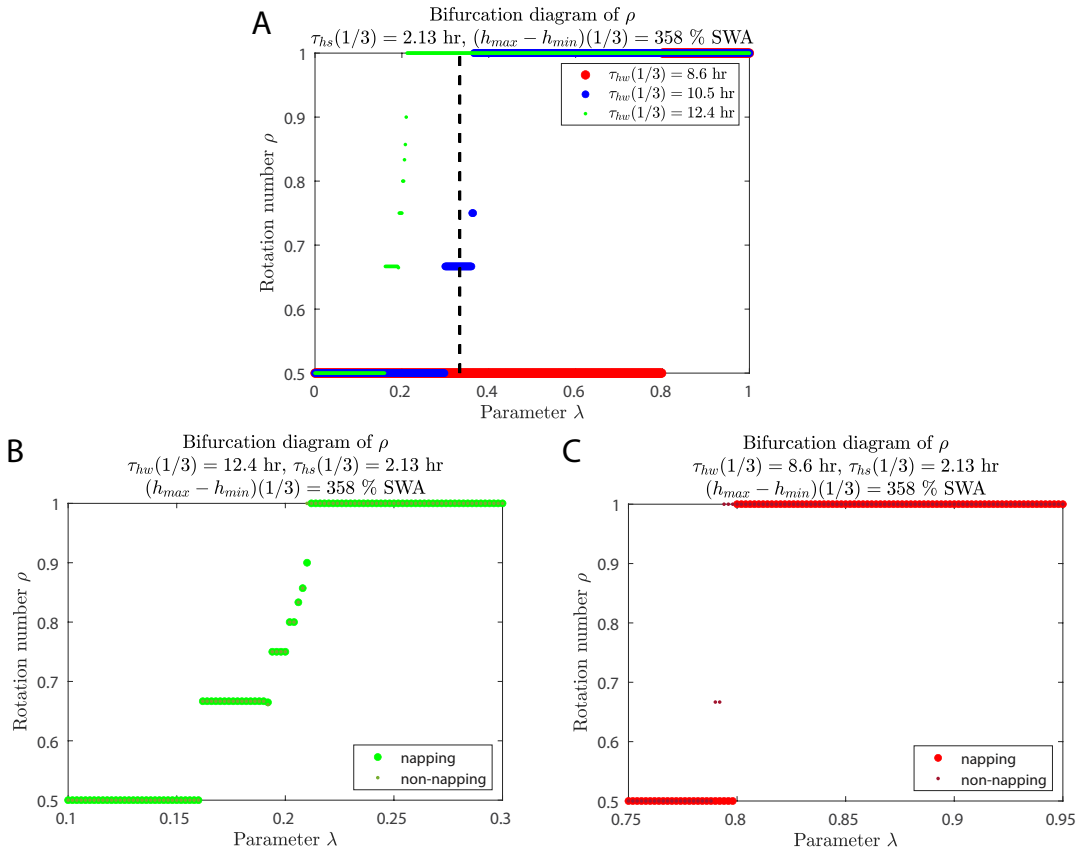

Figure 5.6: Bifurcation diagrams of ρ demonstrating the evolution of the rotation number for distinct τ_{hw} variations and comparison of the napping and non-napping light schedules. We have $\alpha_{k_2} = 0.15$ dictating the variation of k_2 (blue trajectory in Figure 5.4D), while h_{max} follows the blue curve in Figure 5.4C. A. Bifurcation diagrams of ρ demonstrating the evolution of the rotation number for distinct τ_{hw} variations. A faster evolution to the 5-year old parameter of τ_{hw} promotes an earlier transition to monophasic sleep (green) and produces more intermediate patterns. B. Comparison of bifurcation diagrams of ρ for $\tau_{hw}(1/3) = 12.4$ hr under the forced napping (light green) and non-napping (dark green) light schedules. The bifurcation diagrams contain more patterns between the $\rho = 1$ and $\rho = 1/2$ solutions, but the light schedules do not influence this transition so that the patterns obtained are distinct. C. Comparison of bifurcation diagrams of ρ for $\tau_{hw}(1/3) = 8.6$ hr under the forced napping (light red) and non-napping (dark red) light schedules. The bifurcation diagrams transition almost immediately from the $\rho = 1/2$ to the $\rho = 1/2$ solution. However, there exists an interval of λ values, namely $\lambda \in [0.788, 0.8]$, in which distinct light schedules lead to distinct sleep patterns.

As λ is increased from 0 to 1, the bifurcation diagrams of ρ exhibit an increase from $\frac{1}{2}$ to 1 under the napping light schedule (Figure 5.6A). When τ_{hw} evolves more slowly to its 5-year old value ($\tau_{hw}(1/3) = 8.6$ hr, red curve in Figure 5.4A), the loss

of stability of the $\rho = \frac{1}{2}$ solution occurs at $\lambda = 0.798$. However, the bifurcations are shifted to smaller λ values when τ_{hw} varies more rapidly towards its 5-year old value. Moreover, more patterns between biphasic and monophasic sleep are generated. This representative example indicates that homeostatic dynamics may strongly affect the transition process in sleep patterning. For example, an increase of τ_{hw} dictates a slower build up of the homeostatic sleep drive. As a result, sleepiness is experienced at a later phase, which in turn promotes the transition to consolidated sleep.

Light schedules compete with higher order patterns

When $\tau_{hw}(1/3) = 8.6$ hr (τ_{hw} traces the red curve in Figure 5.4B), the non-napping light schedule (dark red in Figure 5.6C) produces a similar increase of ρ as the napping light schedule, but promotes the transition to consolidated sleep at a smaller value of λ. However, when $\tau_{hw}(1/3) = 12.4$ hr (τ_{hw} traces the green curve in Figure 5.4B) the non-napping light schedule (dark green in Figure 5.6B) produces a similarly dense bifurcation diagram of ρ as the napping light schedule. Interestingly, in this case, the values of λ at which the $\rho = \frac{1}{2}$ solution ceases to exist and the $\rho = 1$ solution gains stability are the same as in the napping light schedule. This indicates that modifying the light schedule to promote monophasic behavior does not have a significant influence in this parameter regime. Further, this result suggests that the occurrence of these complex higher order patterns suppress the ability of light to significantly influence this transition process.

5.3.4 Sensitivity to the sleep homeostat influences the transition from napping to non-napping behavior

Interindividual differences may manifest in an individual's response to the evolution of the homeostatic sleep drive. In this section, we analyze how the evolution of the parameter k_2, denoting how sensitive or how resistant to changes in sleep pressure

one may be, affects the transition between biphasic and monophasic sleep, when the manner in which the homeostatic sleep drive evolves is maintained. In particular, we choose τ_{hw} and h_{max} to trace values on the blue trajectories in Figure 5.4 (panels A and C, respectively) and allow α_{k_2} to vary.

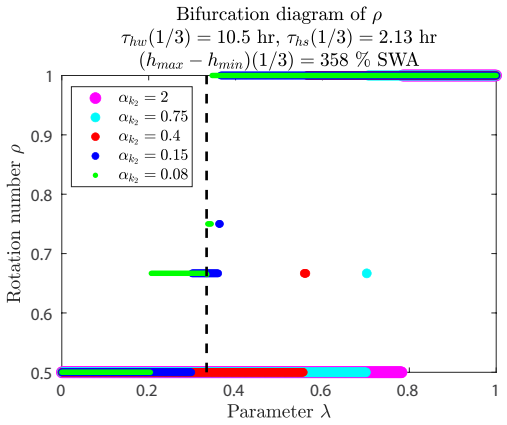

Figure 5.7: Bifurcation diagrams of ρ demonstrating the evolution of the rotation number for distinct k_2 variations dictated by α_{k_2}. A faster evolution to the 5-year old value of k_2 promotes an earlier transition to monophasic sleep (green). By contrast, a slower evolution to the 5-year old value of k_2 maintains biphasic sleep for a longer interval of λ values (red, cyan, magenta).

Figure 5.7 shows that the parameter k_2, controlling the sensitivity to the sleep homeostat, has a strong effect on the transition from biphasic to monophasic sleep. In particular, when k_2 saturates faster (smaller α_{k_2}) to the value in the 5-year old parameter set, it promotes an earlier transition to consolidated sleep. However, during this transition more intermediate sleep patterns are obtained. Higher values of k_2 generate patterns involving fewer naps, as the model is more resistant to changes in the homeostatic sleep drive. As α_{k_2} increases, and therefore, k_2 increases more slowly with λ, we observe a monotonic decrease in the λ-intervals bounding the transition region between biphasic and monophasic sleep, as well as a reduction in the types of intermediate patterns produced. In all the transition scenarios, the alternating pattern with rotation number $\frac{2}{3}$ is the most dominant.

5.3.5 Varying α_{k_2} and homeostatic parameters simultaneously

To illustrate the evolution of sleep patterns over a range of homeostatic parameters and sensitivity, we constructed a two-parameter bifurcation diagram with respect to λ and α_{k_2} (Figure 5.8A). The dark blue, lilac and cyan areas in the figure indicate parameter regions (or tongues) where the stable, phase-locked $\rho = \frac{1}{2}$ (dark blue), $\frac{2}{3}$ (lilac), and 1 (cyan) solutions exist, respectively, for $\tau_{hw}(1/3) = 10.5$ hr (blue curve in Figure 5.4A). For larger values of α_{k_2}, the $\rho = \frac{1}{2}$ and $\rho = 1$ entrainment regions abut each other, indicating an abrupt transition from a biphasic to a monophasic sleep pattern as λ is increased. As α_{k_2} is decreased, the distance between these tongues increases, as more intermediate sleep patterns are generated. The most prominent interval corresponds to the alternating pattern with $\rho = \frac{2}{3}$.

The dark red, magenta and red lines indicate the boundaries of the $\rho = \frac{1}{2}$, $\frac{2}{3}$ and $\rho = 1$ solutions, respectively, for $\tau_{hw}(1/3) = 8.6$ hr (red curve in Figure 5.4A). Similarly, the dark green, yellow and light green lines indicate the boundaries of the $\rho = \frac{1}{2}$, $\frac{2}{3}$ and $\rho = 1$ solutions, respectively, when $\tau_{hw}(1/3) = 12.4$ hr (green curve in Figure 5.4A). As explained in the representative bifurcation diagrams above (Figure 5.5), the manner in which the time constant associated with the build-up of the homeostatic sleep drive evolves across development modulates these transition processes. In particular, if τ_{hw} evolves more slowly to its 5-year old value ($\tau_{hw}(1/3) = 8.6$ hr), the boundaries of these tongues are shifted to larger λ values. However, these bifurcations are shifted to smaller λ values when τ_{hw} varies more rapidly towards its 5-year old value ($\tau_{hw}(1/3) = 10.4$ hr), and therefore, homeostatic dynamics promote consolidated sleep earlier.

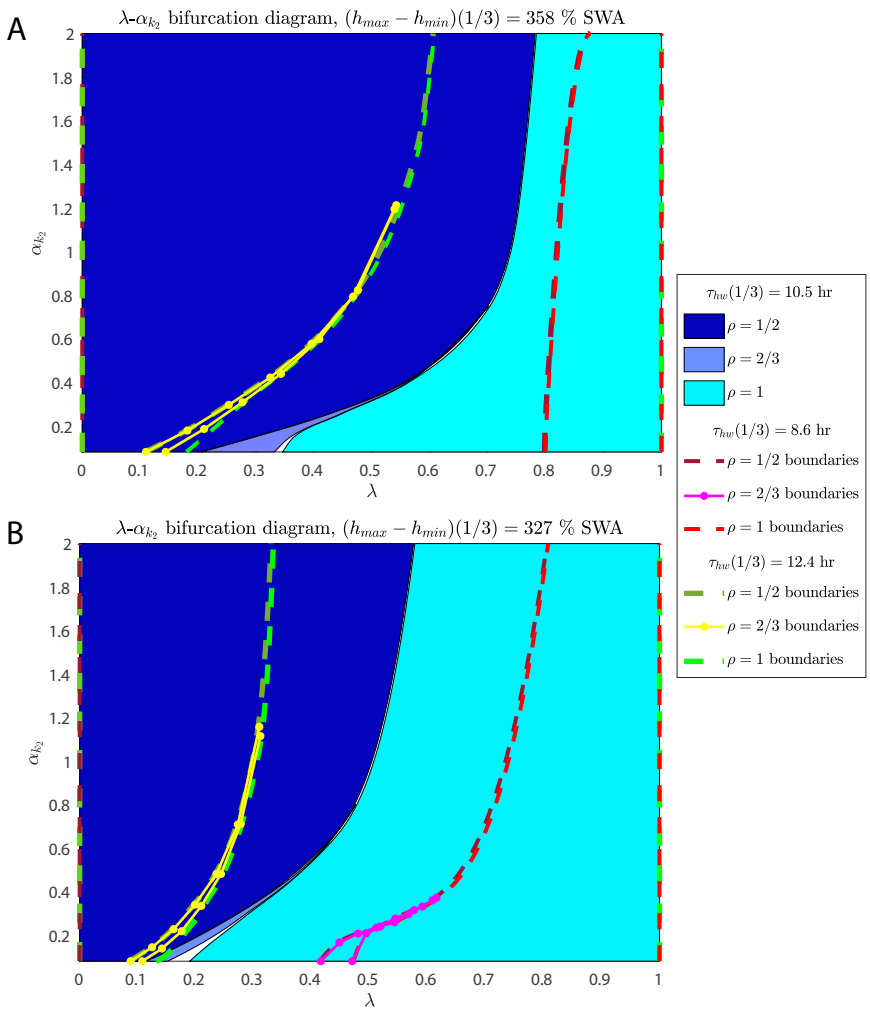

Figure 5.8: Two-parameter bifurcation diagrams with respect to λ and α_{k_2} for $(h_{max} - h_{min})(1/3) = 358\%$ SWA (top) and $(h_{max} - h_{min})(1/3) = 327\%$ (bottom). Colored areas indicate parameter regions (or tongues) where the following stable, phase-locked solutions exist (from left to right) for $\tau_{hw}(1/3) = 10.5$ hr: $\rho = \frac{1}{2}$ (dark blue), $\frac{2}{3}$ (lilac), 1 (cyan). Dark red, magenta and red lines indicate the boundaries of the $\rho = \frac{1}{2}$, $\frac{2}{3}$ and $\rho = 1$ solutions, respectively, when $\tau_{hw}(1/3) = 8.6$ hr. Dark green, yellow and light green lines indicate the boundaries of the $\rho = \frac{1}{2}$, $\frac{2}{3}$ and $\rho = 1$ solutions, respectively, when $\tau_{hw}(1/3) = 12.4$ hr.

We performed the same analysis and compiled the two-parameter bifurcation diagram with respect to λ and α_{k_2} when the difference of the asymptotes at $\lambda = 1/3$ is smaller, namely 327% SWA (Figure 5.8B). Similar trends are observed in this case. That is, more intermediate solutions are produced when the sensitivity to the homeostatic sleep drive, k_2, increases more rapidly (α_{k_2} is small). Furthermore, the evolution

of the accumulation rate of the sleep homeostat promotes earlier ($\tau_{hw}(1/3) = 12.4$ hr) or later ($\tau_{hw}(1/3) = 8.6$ hr) transitions to consolidated sleep as λ is increased. The two bifurcation diagrams (Figure 5.8A, B) exhibit quantitative differences, suggesting that the evolution of the distance between the upper and lower asymptotes characterizing the homeostatic sleep drive may also influence the age at which transitions from biphasic to monophasic sleep patterns occur.

5.4 Discussion

In this work, we employed a physiologically-based model to capture transitions in sleep patterns during early childhood. We utilized our two-state sleep-wake model and identified parameter sets that reflect the napping behavior of most 2 year old children and the non-napping behavior of most 5 year old children. We incorporated values of the homeostatic parameters estimated in experimental studies [101] for the 2- and the 5-year old parameter sets.

We showed that varying a small subset of model parameters can produce the transition from biphasic to monophasic sleep patterns which is quantified by the increase of the rotation number. During this transition, we let the homeostatic time constants and difference of the homeostatic asymptotes vary differently while attaining values estimated in 3-year old children. We also let the parameter k_2, reflecting the sensitivity to the homeostatic sleep drive, saturate faster or more slowly to its 5-year old value by modulating the parameter α_{k_2}. Considering various relationships regarding the variation of these parameters may account for interindividual differences in the response to the developmental changes of the sleep homeostat, and therefore, the transition process to consolidated monophasic sleep behavior.

We found that the homeostatic dynamics characterized by the time constants and asymptotes influence the transition from biphasic to monophasic sleep. In particular, if the sleep pressure accumulates more slowly (larger τ_{hw} values), it promotes the

transition to consolidated monophasic sleep. Our results indicate that different individuals may exhibit distinct transition processes, if the homeostatic sleep drive properties evolve towards the 5-year old values more quickly.

Moreover, these transitions are additionally modulated by the sensitivity to the homeostatic sleep drive. The interaction of the sleep homeostat values and the parameter k_2 may contribute to distinct transition behaviors. Specifically, transitions may occur at distinct λ intervals, corresponding to different ages. A slower rise of the parameter k_2 (larger α_{k_2}) maintains biphasic sleep for higher λ values. The evolution of k_2 may also modulate the number and types of intermediate sleep patterns produced during the transition from napping to non-napping behavior. A more abrupt rise of the parameter k_2 (smaller α_{k_2}) generates more patterns, namely a denser bifurcation diagram of ρ, in most parameter regimes.

Sleep timing is influenced by the circadian rhythm [35, 51, 150], whose strongest modulator is light exposure. In this study, we found that certain individuals may be sensitive to light during their transition from biphasic to monophasic sleep. That is, forcing a period of dim light in the middle of the day may contribute to the persistence of napping sleep behavior, whereas eliminating that dim light period may promote the transition to consolidated monophasic sleep. The effect of light schedules is evident when the bifurcation diagrams obtained are sparse; namely, only a few higher order sleep patterns are generated in the transition between biphasic and monophasic sleep patterns. In contrast, when the model predicts a transition through various intermediate patterns between the biphasic and monophasic regimes, enforcing the napping or the non-napping light schedule does not significantly affect the sleep pattern. Future work will consider light schedules with a range of durations, light intensities and timing of the dim light period to investigate whether and how they may affect the transition to monophasic sleep.

Our work emphasizes the need to further understand the manner in which pa-

rameters associated with the sleep homeostat vary across development. Furthermore, individual characteristics may lead to differences in these parameters, and therefore, to a smoother or more challenging transition to consolidated sleep. Incorporating additional data to inform the trend of how these parameters change with development will provide a more robust classification of sleep patterns and association of our bifurcation parameter with age. Future work will aim to create charts of percentile curves that illustrate the distribution of sleep patterns in preschool children across the transition from napping to non-napping behavior. We further aim to analyze the effect of various light schedules and propose possible light interventions to promote desired sleep behaviors.

CHAPTER VI

Mapping Recovery of Sleep Deprivation

6.1 Introduction

Under typical adult human sleep-wake schedules, the circadian and homeostatic processes work together to promote consolidated waking during the day and consolidated sleep during the night. However, when sleep schedules are disrupted, for example due to sleep deprivation, these processes may compete and affect the timing and duration of sleep episodes. For example, recovery sleep following sleep deprivation may be shorter or longer than habitual sleep duration depending on the circadian phase (time of day) of the onset of recovery sleep [167]. Furthermore, while nocturnal sleep typically includes both REM and NREM sleep states, with cyclic alternation between the two states over the course of the night, sleep deprivation may affect the duration and timing of both NREM and REM sleep [133].

Mathematical models of sleep-wake regulation have been previously used to understand and predict changes in sleep not only after sleep deprivation but also as a result of other perturbations including shift work, travel across time zones, sleep disorders such as narcolepsy, and pharmacological interventions [39, 130, 74, 17, 53]. While the classic two-process model [26, 104] accounts for sleep deprivation by considering interactions between the homeostatic sleep drive (Process S) and the circadian rhythm (Process C) [39, 3], more recent physiologically-based models consider the effects

of extended wakefulness on connections between neuronal populations that govern sleep-wake dynamics [100, 134, 131, 126]. In previous work, Piltz et al. used the three-state physiologically-based model described in Chapter II, to investigate the variation of sleep deprivation responses in individuals with different habitual sleep durations (e.g., long and short sleepers) [129]. In this chapter[1], we apply circle maps computed from the three-state sleep-wake network model to predict responses to acute sleep deprivation and validate model results with both experimental data and numerical simulations of the model [71] that incorporate behaviorally-appropriate light schedules.

This chapter is organized as follows: in Section 6.2, we first review dynamics of the three-state sleep-wake network model under baseline and sleep deprivation conditions, and then summarize the numerical computation of the map representing the dynamics of the model in Section 6.2.2. In addition, we decompose the map and use it to compute the length of recovery sleep following sleep deprivation. In Section 6.3, we present predictions obtained from the map for (i) the length and (NREM–REM) composition of recovery sleep and (ii) the duration of recovery sleep from 0 to 24 hours of sleep deprivation. Furthermore, we compare these predictions with experimental data and numerical simulations of the full model. Finally, we discuss our findings and their implications in Section 6.4.

6.2 Methods

6.2.1 Physiologically-based model for human sleep and wake dynamics

In this study, we consider the three-state sleep-wake regulatory network model described in Section 2.2 incorporating the Forger et al. circadian model (Figure 6.1; see Chapter II). To simulate sleep deprivation, we impose a wake-promoting input that

[1]This work was conducted jointly with Sofia Piltz and a manuscript on these results is published in *Communications in Nonlinear Science and Numerical Simulation*.

is excitatory to the wake population and inhibitory to the NREM sleep population. Under regular conditions, we simulate a 14-hour:10-hour environmental light:dark cycle with light intensity $I = 5000$:$I = 0$ lux. In simulations of sleep deprivation (see Figures 6.2, 6.4, and 6.5), we mimic the light environment used in experimental sleep deprivation studies (e.g., [3]). That is, if the model's state is "awake" during the environmental dark period, $I = 300$ lux to represent indoor light intensity for light activity such as reading. By contrast, if the model is "asleep" during the environmental light period, $I = 100$ lux to represent light penetrating the eyelids.

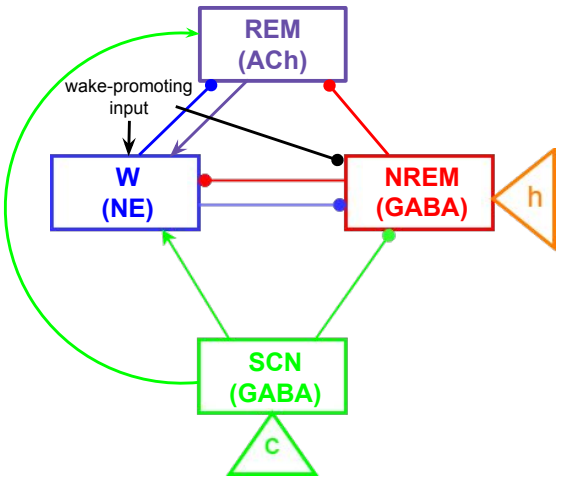

Figure 6.1: Model schematic. The physiologically-based model [71] for human sleep incorporates equations for the average firing rate of the neuronal populations promoting states of Wake, NREM and REM sleep, and the SCN (boxes; NE, GABA, and ACh indicate the primary neurotransmitters for each population), the homeostatic sleep drive (h, orange triangle), and the circadian clock oscillator (c, green triangle). Excitatory (inhibitory) effects of neurotransmitter-mediated projections among populations are indicated by arrows (circles). To simulate sleep deprivation, we impose a wake-promoting input (black) that is excitatory to the wake population and inhibitory to the NREM sleep population.

We use values of model parameters identified in previous work [129] (described in Table 2.2) where Piltz et al. computed an ensemble of $\sim 20,000$ parameter sets that were fit to replicate the baseline wake, REM and NREM sleep timing and durations experimentally measured from humans exhibiting typical (and habitual) sleep behavior

[20]. Results shown here were derived using a parameter set corresponding to median values of the ensemble, with variability between the 25th and 75th percentile values of the ensemble shown in Figures 6.3, 6.4 and 6.6.

Time traces of the activity of the neuronal populations (top), h (middle), and c (bottom) for two example simulations of sleep deprivation where sleep onset occurs 8 and 20 hours past the usual sleep onset (indicated by a vertical dotted line) are shown in Figure 6.2, panels A and C, respectively. Model trajectories evolve on a Z-shaped surface (obtained by a fast-slow decomposition, see Chapter II) where the top (blue) manifold indicates the stable steady "wake" state and the bottom (red) manifold indicates an unstable steady state associated with the stable periodic solution representing NREM–REM cycling during the "sleep" state (Figure 6.2B and D).

During simulations of sleep deprivation (purple and orange curves in Figure 6.2B and D, respectively), the trajectory continues to evolve along the "wake" manifold, close to the curve of saddle-node points instead of dropping to the "sleep" state as occurs under typical sleep-wake conditions (black filled circles on blue trajectory in Figure 6.2B and D). When sleep onset eventually occurs (leftmost purple and orange filled circles in Figure 6.2B and D), the trajectories exhibit different paths on the "sleep" manifold than the baseline (blue) trajectory reflecting differences in sleep durations and timing. These perturbed trajectories obtain higher than baseline values in h as h increases during the extended "wake" state of the model (Figure 6.2A and C, middle panels) and have slightly varied c values due to differences in light exposure (Figure 6.2A and C, bottom panels). Over the following few sleep-wake cycles, these trajectories approach the baseline trajectory for the stable sleep-wake pattern (Figure 6.2B and D).

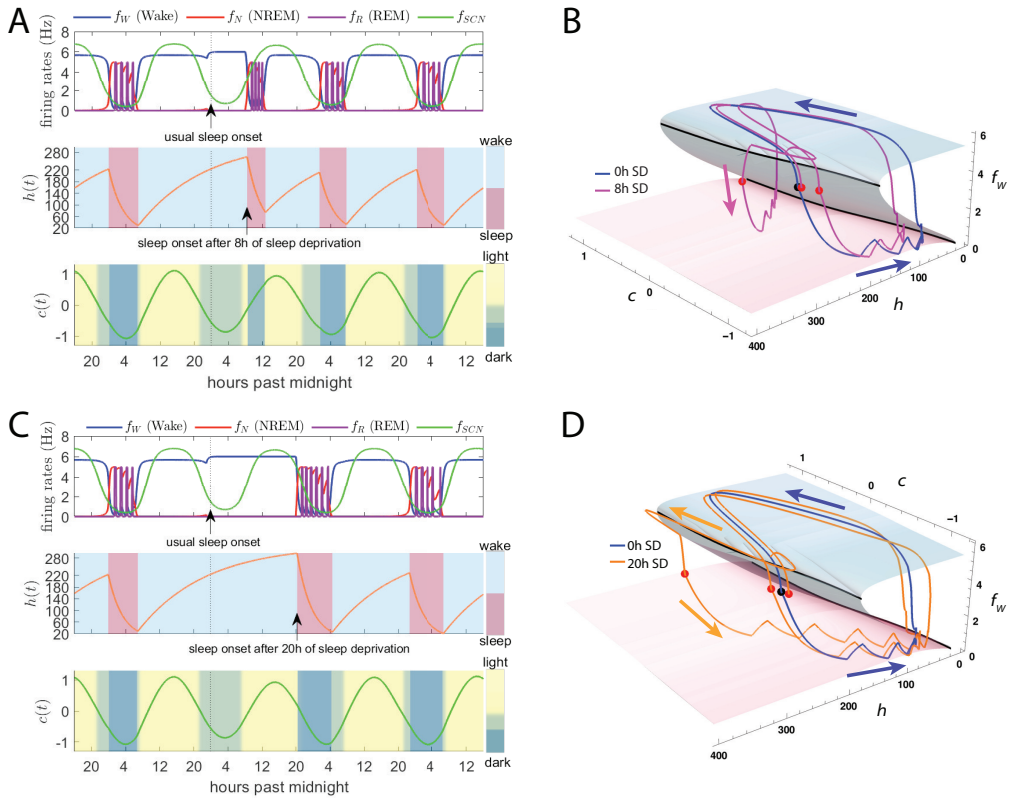

Figure 6.2: Example model simulations for sleep deprivation of 8 and 20 hours. A,C: Time traces of population firing rates (top), homeostatic sleep drive h (middle) and circadian drive c (bottom) for four days with sleep deprivation of 8h (A) and 20h (C) from usual sleep onset occurring on the 2nd day (usual sleep onset indicated with black arrows and vertical dotted line). Light intensity input to the circadian clock oscillator varies with simulated model behavior (background colors in bottom panels, see also Section 6.2). B,D: Surface of steady state solutions revealed by a fast-slow decomposition of the model when h and c are taken as fixed parameters. The top (blue) surface represents the stable wake state and the bottom (red) surface represents the unstable solution surrounded by the stable periodic solution (e.g., see blue trajectory) exhibiting NREM–REM cycles. Trajectories for the full model when h and c are allowed to vary show how the steady state "wake" and "sleep" manifolds influence solutions of the full model [blue trajectory shows the stable, baseline sleep model solution while the purple (orange) trajectory is the model solution for 8 hours (20 hours) of sleep deprivation B (D)]. We indicate sleep onsets on the trajectories with filled circles.

6.2.2 Circle maps and computing the length of sleep (wake) time

The dynamics of the sleep-wake model can be described by a circle map for successive circadian phases of sleep onset. The map represents the relationship between the sleep onset at a given circadian phase on the nth sleep cycle (consisting of one sleep and one wake episode) and the successive sleep onset, occurring on the $n+1$st sleep cycle (described in detail in Chapter II). In order to maintain a consistent definition of circadian phase to compute the map, during the numerical simulations of the model the light cycle is fixed to the environmental 14:10h L:D cycle (i.e., $I = 500$ ($I = 0$) lux during the light (L) (dark, D) period as in [25]). This fixed light schedule used for computing the map contrasts with the behaviorally-gated light schedule used to simulate sleep deprivation in the full model where we mimic the light exposure schedules during the experimental conditions (see Section 6.2).

The one-dimensional map, Φ_{ss}, gives the circadian phase for sleep onset on sleep cycle $n+1$, ϕ_{n+1}, as a function of the circadian phase of sleep onset on sleep cycle n, ϕ_n (see Figure 6.3A):

$$\phi_{n+1} = \Phi_{\text{ss}}(\phi_n)\,. \tag{6.1}$$

The $n+1$st sleep onset may occur during the same circadian cycle as the nth sleep onset (day i in Figure 6.3) or during the following circadian cycle (day $i+1$). In this work, we decompose Φ_{ss} into two maps (Figure 6.3C and D, respectively): (1) Φ_{sw} which gives the circadian phase of wake onset as a function of the circadian phase of the preceding sleep onset and (2) Φ_{ws} which gives the circadian phase of sleep onset as a function of the circadian phase of the preceding wake onset at sleep cycle n. Thus,

$$\phi_{n+1} = \Phi_{\text{ss}}(\phi_n) = (\Phi_{\text{ws}} \circ \Phi_{\text{sw}})(\phi_n) = \Phi_{\text{ws}}[\Phi_{\text{sw}}(\phi_n)]\,. \tag{6.2}$$

Decomposing the sleep onset-sleep onset map Φ_{ss} into a composition of Φ_{ws} and Φ_{sw} allows us to determine the length of time asleep (awake) for a given sleep (wake)

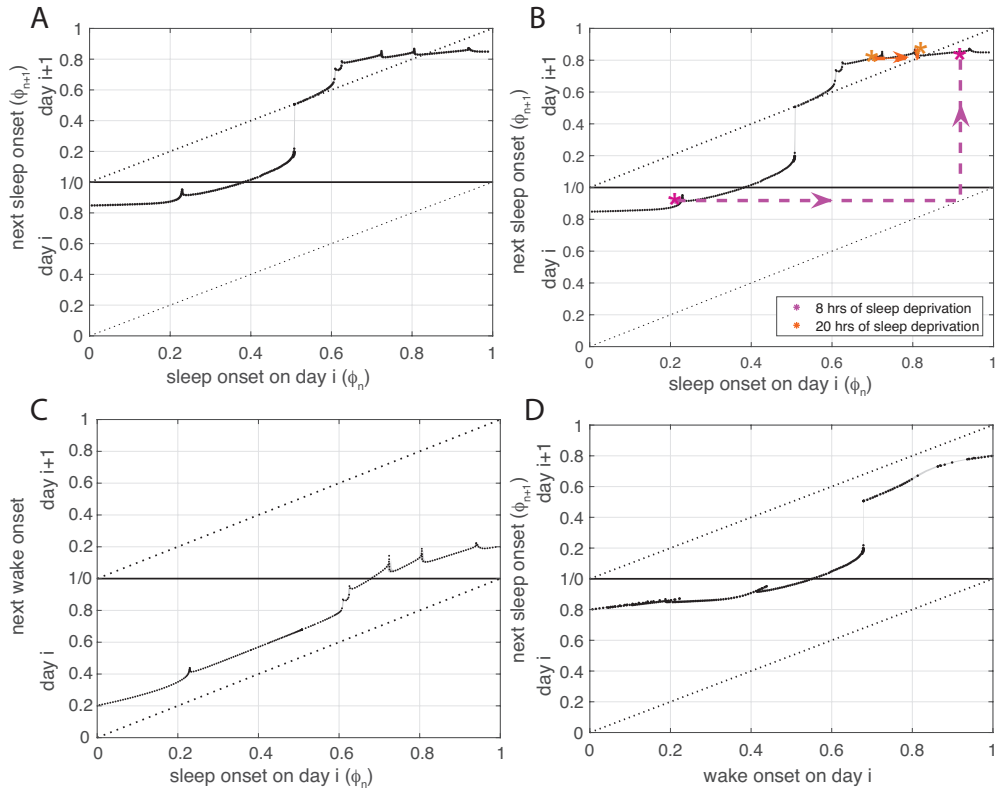

Figure 6.3: Circle maps representing the dynamics of the sleep-wake network model. A,B: Map Φ_{ss} gives the circadian phase of the $n+1$st sleep onset (ϕ_{n+1}) on day (circadian cycle) i (bottom panel) or $i+1$ (top panel) as a function of the circadian phase of the nth sleep onset on day (circadian cycle) i (ϕ_n). B: Cobwebbing of sleep onset phases during simulations of 8h (purple) and 20h (orange) of sleep deprivation as shown in Figure 6.2. C: Map Φ_{sw} gives the circadian phase of the next wake onset [on day i (bottom) or $i+1$ (top)] as a function of the circadian phase of the nth sleep onset ϕ_n on day i. D: Map Φ_{ws} gives the circadian phase of the next sleep onset [ϕ_{n+1} on day i (bottom) or $i+1$ (top)] as a function of the circadian phase of the wake onset on day i. Phase 0/1 indicates the minimum of the circadian variable c. The black dots are map point values computed from the model using the median values of the parameter ensemble for typical adult sleep-wake behavior and the gray bands indicate variability in the maps computed using parameter values at the 25th and 75th percentile of the ensemble (for more details, see [129]).

onset phase predicted by the map. Thus, if the phase of the next wake (sleep) onset is above the $y = x$ –line, the time spent asleep (awake) is (in hours)

$$\Delta S = 24(y - x)\,. \tag{6.3}$$

If a point is below the $y = x$ –line, the time spent asleep (awake) is (in hours)

$$\Delta S = 24(1 - x) + y\,. \tag{6.4}$$

In what follows, we show that these predictions for the duration of recovery sleep obtained from the map are consistent with both experimental data associated with 8- and 24-hours of sleep deprivation and our simulations of a range of sleep deprivations from 0- to 24-hours in the full sleep-wake model which incorporates features of sleep deprivation such as realistic patterns of light exposure and increases in homeostatic sleep drive above typical values (see Figures 6.4 and 6.5).

6.3 Results

The one-dimensional sleep onset-to-sleep onset map Φ_{ss} (Figure 6.3 A) represents the dynamics of the three-state sleep-wake network model (see Section II). The stable periodic solution is indicated by the fixed point of Φ_{ss} (sleep onset near $0.83 \approx$ at 11:58pm) corresponding to a typical human baseline sleep onset on the descending phase of the circadian cycle. The map Φ_{ss} also has an unstable fixed point (near $0.54 \approx$ 4:58pm) with a slope slightly larger than 1. A distinctive feature of Φ_{ss} is the vertical discontinuity for initial sleep onsets occurring just past the circadian peak ($0.5 \leq \phi_n \leq 0.6$). This discontinuity reflects a large increase in the phase (time) of succeeding sleep onsets for only small differences in the phase (time) of the initial sleep onsets [and is due to a tangency of the trajectory with the saddle-node bifurcation points of the steady state solution surface (Figure 6.2B and D)].

The map Φ_{ss} also illustrates variations in the number of REM bouts per sleep episode depending on the circadian phase of sleep onset, with cusps over the interval $0.6 \leq \phi_n \leq 1$ demarcating the regions of the map associated with different characteristic numbers of REM bouts. For example, sleep onsets near the stable fixed point result

in 4 REM bouts per sleep episode while sleep onsets at earlier and later phases (and past the respective cusps) contain 5 and 3 REM bouts, respectively. The decomposed maps Φ_{sw} and Φ_{ws} lack fixed points but maintain features of Φ_{ss} (Figure 6.3C, D), such as the vertical discontinuity for wake onset phases in the interval $(0.6, 0.8)$ in Φ_{ws} (Figure 6.3D) (which indicates that the discontinuity in Φ_{ss} near $\phi_n = 0.5$ is due to a discontinuous change in wake episode duration). The map Φ_{sw} (Figure 6.3C) contains cusps that demarcate regions of Φ_{ss} associated with different numbers of REM bouts within the sleep episode.

Above all, Φ_{ss} can be used to approximate sleep-wake patterns of recovery sleep following sleep deprivation. As a result of sleep deprivation, sleep onset occurs at different circadian phases (times) and the evolution of model trajectories back to the stable sleep-wake solution represents recovery sleep and can be tracked on Φ_{ss} by the usual cobwebbing technique. For example, recovery from 8 and 20 hours of sleep deprivation are indicated with cobwebbing in Figure 6.3B where the asterisks show the sleep onset phases computed from the sleep deprivation simulations shown in Figure 6.2.

Predictions for the length of recovery sleep computed from Φ_{ss} (using Equations (6.3)–(6.4), Figure 6.4) indicate that sleep episodes starting 0–19 hours after the usual sleep onset time result in shorter total and REM sleep durations compared to the baseline sleep. For longer periods of sleep deprivation, the map predicts a sharp increase in the duration of recovery sleep. This pattern agrees with results observed in human experimental data [167] and in simulations of the two-process model [39]. In addition, recovery sleep durations computed from Φ_{ss} are consistent with durations obtained from simulations of the full model (compare black dots with red crosses in Figure 6.4) despite the inability of the map to account for the increases in homeostatic sleep drive h accrued during the deprivation period or the altered light conditions during extended wakefulness. Furthermore, both the map predictions and the sleep

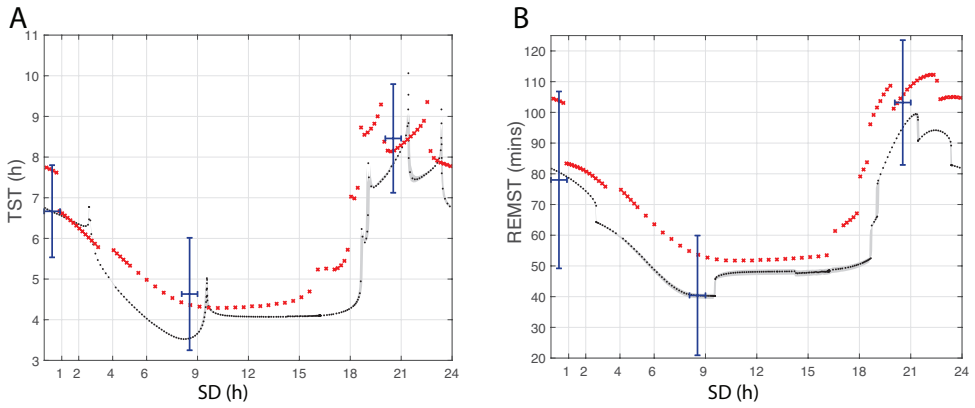

Figure 6.4: Predicted durations of recovery sleep following 0–24 hours of sleep deprivation. Comparison of the total sleep time (TST, panel A) and REM sleep time (REMST, panel B) predicted by the map Φ_{sw} for sleep onsets at circadian phases associated with 0 to 24h of sleep deprivation (SD) (i.e., sleep onset occurs 0–24h after the usual (baseline) sleep onset) (black dots and gray shading) and model simulations of 0 to 24h of sleep deprivation (red crosses). The model simulations are computed with median parameter values and the gray shading represents the 25th and 75th percentiles of the parameter ensemble (for more details, see [129]). Experimentally-measured durations of recovery TST and REMST for 0h, $\approx$ 8h and $\approx$ 20h of sleep deprivation have been reported in [20] (blue markers including $\pm$ standard deviation for sleep onset phases and durations).

deprivation simulations for total sleep time and REM sleep time are consistent with experimental data for recovery following 8 and 20 hours of sleep deprivation [20] (see blue dots and error bars in Figure 6.4). The durations of total sleep and REM sleep during recovery show discrete jumps for increasing hours of sleep deprivation due to changes in the number of REM bouts, with the shortest sleep episodes containing 3 REM bouts and the longest sleep episodes containing 6 REM bouts.

A comparison between the map and sleep deprivation simulations shows that for the first recovery sleep episode (R1), the sleep durations predicted by Φ_{ss} differ by less than an hour (half an hour) for total (REM) sleep time from the model simulations for most sleep deprivation hours (see blue triangles in Figure 6.5A and C). This suggests that the circadian effects on the duration of total sleep and REM sleep during recovery that are represented by the map dominate other factors contributing to the length of recovery sleep in the model. For most sleep deprivation hours, the map

predictions agree with the simulations by the fifth recovery episode (R5, see yellow circles in Figure 6.5A and C). However, for sleep onsets that occur 15–16 hours past the usual sleep onset (i.e., during the afternoon and near the vertical gap of the map), the simulated solutions have not returned to the baseline sleep by the fifth recovery episode. The discrepancy between the map and model simulations is also larger for these (and nearby) sleep deprivation hours due to the large vertical gap in the map. These long-lasting effects of sleep deprivations of 15–16 hours can be explained by the unstable fixed point on the map as illustrated in a representative sleep deprivation simulation where sleep onset phases remain in the region of the unstable fixed point of the map for many iterations (see Figure 6.6A). Similarly, recovery sleep episodes simulated with the full model exhibit an approximately 12-day transient (during which sleep of about 4.3 hours with 4 REM bouts occurs in the afternoon and early evening) before returning to the baseline (see Figure 6.6B).

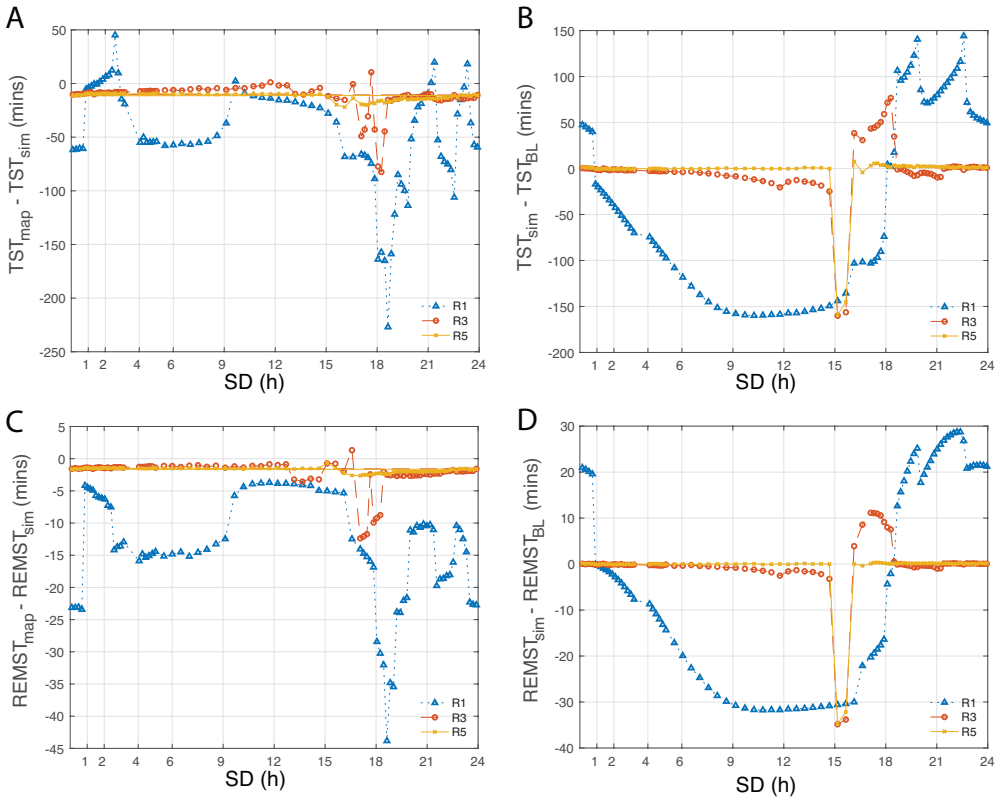

Figure 6.5: Differences between predictions based on the map and model simulations. A,C: Difference in total sleep time (A) and REM sleep time (C) during the first (R1, blue triangles), third (R3, red circles) and fifth (R5, yellow crosses) recovery sleep episodes following 0 to 24h of sleep deprivation predicted by the map ($\mathrm{TST_{map}}$, $\mathrm{REMST_{map}}$) and by model simulations of sleep deprivation ($\mathrm{TST_{sim}}$, $\mathrm{REMST_{sim}}$). B,D: Difference between usual (baseline) TST ($\mathrm{TST_{BL}}$, B) and (baseline) REMST ($\mathrm{REM_{BL}}$, D) in the first (R1, blue triangles), third (R3, red circles) and fifth (R5, yellow crosses) recovery sleep episodes following 0 to 24h of sleep deprivation predicted by model simulations ($\mathrm{TST_{sim}}$, $\mathrm{REMST_{sim}}$). The x-axis indicates the sleep onset in 0–24h after the usual (baseline) sleep onset (SD). For panels A and C, the usual sleep onset is considered as the sleep onset of the fixed point of the map Φ_{ss}, while for panels C and D, the usual sleep onset is that of the stable periodic solution in the model simulations. We note that because of the differences in light schedules, there is a (negligible) difference between the circadian phase of the fixed point and that of the stable periodic solution.

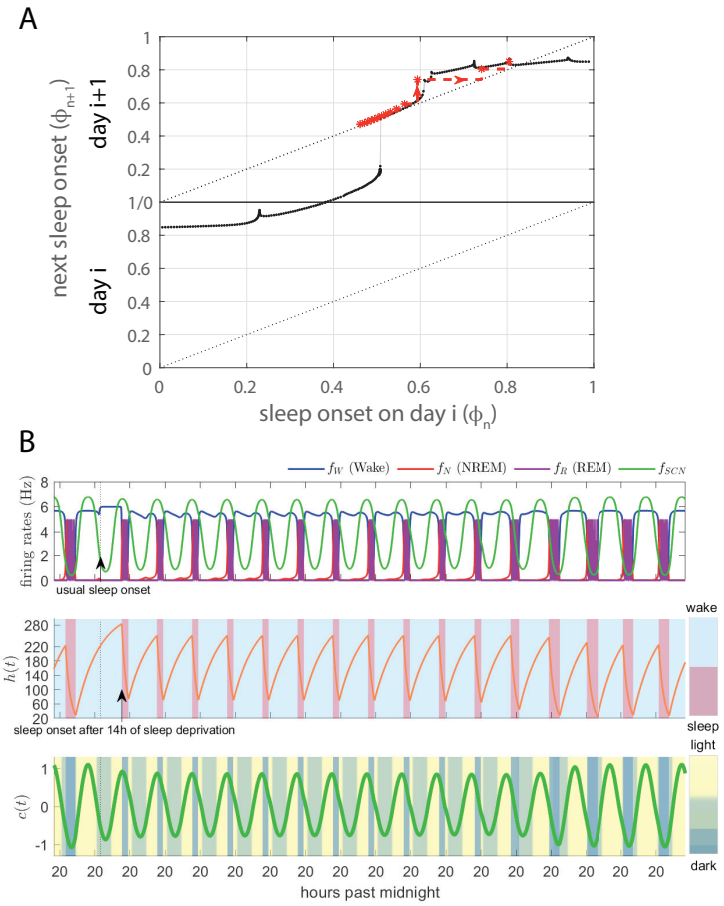

Figure 6.6: An example of long-lasting effects of acute sleep deprivation A: A model simulation for approximately 15h of sleep deprivation (asterisks) generates an initial sleep onset near the region of the unstable fixed point of the map (black dots and gray shading). B: Similarly, simulation of the full model predicts a long transient (of about 12 days) before returning to the baseline sleep solution. During this transient, sleep episodes are short (about 2.7 h less than baseline sleep) and desynchronized from the circadian rhythm with sleep onsets occurring in the afternoon and early evening (approximately 3:05 pm to 6:20 pm). Following the transient, sleep-wake behavior re-entrains to the circadian rhythm, and the timing and duration of baseline sleep are re-established.

6.4 Discussion

In this chapter, we applied a circle map describing the dynamics of an 8-dimensional, physiologically-based, ordinary differential equation model for human sleep-wake regulation to predict the effects of acute (i.e., one-time, less than 24-hour) sleep deprivation. The map reproduces patterns in the durations of recovery sleep observed

in both experimental data and simulations of sleep deprivation using the full model. In addition, the accuracy of the predictions computed from the map suggests that the circadian rhythm and its influences are stronger than the effect of the homeostatic sleep drive on the duration of recovery sleep.

Although the map is a simplification of the sleep-wake regulation model, it helps to explain sleep deprivation simulations in three principal ways. First, the map describes the effects of circadian phase on the duration of recovery sleep and establishes a lower bound for recovery sleep durations. This is because the map does not account for additional aspects of sleep deprivation that would increase the duration of recovery sleep (such as increased homeostatic sleep drive and prolonged light exposure during sleep deprivation which are considered in the full sleep-wake model). Second, the map predicts that the duration of sleep deprivation, and the resulting circadian phase of the sleep onset, can affect the time course of recovery sleep over multiple days (which is consistent with simulation results using the full model). In particular, sleep onsets at circadian phases near the large, vertical discontinuity of the map (i.e., when $\phi_n = 0.5$ near the peak of the circadian rhythm) result in a long recovery to baseline sleep. Finally, cobwebbing on the map can be used to estimate and illustrate the evolution of sleep-wake behavior during recovery from sleep deprivation and return to the baseline sleep. Thus, the map provides a computationally-efficient tool for predicting features of recovery sleep that follows sleep deprivation.

Both total sleep and REM sleep time are increasingly recognized as important for cognitive performance and physical and mental health (e.g., [97, 158, 153, 73, 146]). This awareness has led to the development of multiple mobile applications and electronic monitoring systems that track sleep and promote healthy sleep habits (e.g., [160, 16]). Many of these programs rely on mathematical models to predict sleep durations and responses to disrupted sleep schedules. We propose that one-dimensional maps can provide a computationally-efficient means to predict the effects of acute

sleep deprivation. A map, such as the one presented here, that predicts the timing and duration of total and REM sleep during recovery sleep, may be leveraged to design optimal recovery strategies for individuals exposed to acute sleep deprivation. Moreover, these strategies may be designed to account for constraints such as limited recovery sleep time or repeated sleep deprivations. Previously, map-based approaches have been applied to represent entrainment of the circadian oscillator following perturbations such as transmeridian travel [46, 47]. Thus, computationally-efficient representations of sleep and circadian dynamics may be used to simulate a range of sleep perturbation and recovery scenarios. However, inter-individual differences in baseline sleep may also affect responses to sleep deprivation [156, 129] and jet lag [8]. Therefore, future work is needed to identify the key parameters necessary for representing interindividual variability in sleep-wake responses and, thereby, enable the derivation of maps that provide real-time, personalized predictions for recovery sleep.

CHAPTER VII

Conclusions and Future Work

In the chapters of this dissertation we used mathematical modeling to investigate how sleep-wake dynamics are affected by different perturbations. Specifically, we established a mathematical framework for characterizing the dynamics of sleep patterns in physiologically-based models of human sleep-wake regulation. We employed circle maps to analyze sleep-wake dynamics under variation of the circadian and homeostatic sleep drives (Chapters III,IV) or perturbations due to sleep deprivation (Chapter VI). Additionally, we conducted a detailed bifurcation analysis to describe changes in sleep patterns mediated by developmental changes (Chapters III-V).

We showed that varying the time constants and asymptotes of the homeostatic sleep drive produces a transition from polyphasic to monophasic sleep, a process observed from infancy to preschool years. This transition process may be strongly modulated by properties of the circadian drive waveform (Chapter III). In particular, steeper temporal profiles of the SCN firing rate lead to a more abrupt transition between certain sleep patterns (e.g. biphasic to monophasic). Light exposure influences the circadian drive and may play an important role in promoting napping or non-napping behavior (Chapter V). The transition from biphasic to monophasic sleep patterns can be distinct depending on how properties of the sleep homeostat vary across development (Chapter V).

Mathematically, varying the properties of the circadian waveform and the sleep homeostat simultaneously generates a rich set of bifurcation sequences illustrated through the use of circle maps as described in detail in Chapter III. Furthermore, we found that the ultradian dynamics due to NREM-REM alternation gives rise to non-monotonic, noninvertible and nonsmooth maps. This structure disrupts the period-adding trend of the average number of sleeps per day, and allows for more complicated phenomena to occur influenced by the number of REM bouts involved in a sleep-wake pattern (Chapter IV). The maps capture responses to sleep deprivation (Chapters VI) or more generally, desynchrony between the sleep-wake network and the circadian rhythm, and can be used to determine the reentrainment process.

Our work to date has provided insight on important mechanisms modulating sleep patterns and created avenues for future work. Some future projects are briefly discussed below.

7.1 Circadian modulation of the transition from polyphasic to monophasic sleep in the three-state sleep-wake model

Our work in Chapter III established a dependence of the transition from polyphasic to monophasic sleep mediated by the homeostatic sleep drive on the steepness of the circadian waveform. We conducted our analysis using the two-state SWFF model. Future work will perform a similar analysis in the three-state model to understand the role of NREM-REM cycling in the sleep patterns generated under homeostatic and circadian variation.

7.2 Data-driven modeling of sleep in preschool children in the three-state sleep-wake model

In Chapter V, we focused on the transition from napping to non-napping sleep behavior in preschool children. We found parameter sets for the two-state SWFF model that capture the timing, duration and type of patterns for 2-year and 5-year old children based on experimental data. We aim to extend our results in the three-state model and obtain parameter sets that capture the distribution of REM sleep in preschool children and understand transitions to consolidated sleep due to homeostatic variation.

7.3 Canards in models of sleep-wake regulation

Canards are a special type of solution trajectory of fast-slow dynamical systems that remain close to a repelling region of the solution phase space for an extended amount of time. Canards have been observed in models of single neurons, and act to separate trajectories with distinct excitability behaviors. Numerical solutions in our SWFF model when we impose a steeper circadian waveform (studied in Chapter III) have exhibited canard-like behavior that could be a contributing factor to the bifurcations occurring in the systems. Therefore, we wish to investigate whether canards indeed emerge in the models described here, and understand the physiological implications of such phenomena for sleep-wake regulation.

BIBLIOGRAPHY

BIBLIOGRAPHY

[1] E. E. Abrahamson, R. K. Leak, and R. Y. Moore. The suprachiasmatic nucleus projects to posterior hypothalamic arousal systems. *Neuroreport*, 12:435–440, 2001.

[2] C. Acebo, A. Sadeh, R. Seifer, O. Tzischinsky, A. Hafer, and M.A. Carskadon. Sleep/wake patterns derived from activity monitoring and maternal report for healthy 1- to 5-year old children. *Sleep*, 28:1568–1577, 2005.

[3] D. Aeschbach, C. Cajochen, H. Landolt, and A. A. Borbély. Homeostatic sleep regulation in habitual short sleepers and long sleepers. *American Journal of Physiology-Regulatory, Integrative and Comparative Physiology*, 270(1):R41–R53, 1996. PMID: 8769783.

[4] L. D. Akacem, C. T. Simpkin, M. A. Carskadon, K. P. Wright, Jr., O. G. Jenni, P. Achermann, and M. K. LeBourgeois. The timing of the circadian clock and sleep differ between napping and non-napping toddlers. *PLOS ONE*, 10(4):1–12, 04 2015.

[5] R. Allada, C. Cirelli, and A. Sehgal. Molecular mechanisms of sleep homeostasis in flies and mammals. *Cold Spring Harbor Perspectives in Biology*, 9:a027730, 04 2017.

[6] V. I Arnold. Cardiac arrhythmias and circle mappings a. *Chaos (Woodbury, N.Y.)*, 1(1):20–24, 7/1991.

[7] E. Aserinsky and N. Kleitman. Regularly occurring periods of eye motility, and concomitant phenomena, during sleep. *Science*, 118(3062):273–274, 1953.

[8] I. E. Ashkenazi, A. E. Reinberg, and Y. Motohashi. Interindividual differences in the flexibility of human temporal organization: Pertinence to jet lag and shiftwork. *Chronobiology International*, 14(2):99–113, 1997.

[9] G. Aston-Jones, S. Chen, Y. Zhu, and M. L. Oshinsky. A neural circuit for circadian regulation of arousal. *Nat Neurosci*, 4:732–738, 2001.

[10] C. Athanasouli, S. H. Piltz, C. Diniz Behn, and V. Booth. Bifurcations of sleep patterns due to homeostatic and circadian variation in a sleep-wake flip-flop model. 2021.

[11] V. Avrutin, L. Gardini, I. Sushko, and F. Tramontana. *Continuous and Discontinuous Piecewise-Smooth One-Dimensional Maps: Invariant Sets and Bifurcation Structures*. World Scientific Publishing, 2014.

[12] V. Avrutin and I. Sushko. A gallery of bifurcation scenarios in piecewise smooth 1d maps. In G.I. et al. Bischi, editor, *Global Analysis of Dynamic Models in Economics and Finance*. Springer-Verlag, 2013.

[13] C. Baesens and R. MacKay. Analysis of a scenario for chaotic quantal slowing down of inspiration. *J. Math. Neurosci.*, 3:18, 2013.

[14] M. P. Bailey, G. Derks, and A. C. Skeldon. Circle maps with gaps: Understanding the dynamics of the two-process model for sleep–wake regulation. *European Journal of Applied Mathematics*, 29(5):845–868, 2018.

[15] R Basheer, RE Strecker, MM Thakkar, and RW McCarley. Adenosine and sleep-wake regulation. *Prog Neurobiol*, 73:379–396, 2004.

[16] J. Behar, A. Roebuck, J. S. Domingos, E. Gederi, and G. D. Clifford. A review of current sleep screening applications for smartphones. *Physiological Measurement*, 34(7):R29–R46, jun 2013.

[17] C. G. Diniz Behn, E. N. Brown, T. E. Scammell, and N. J. Kopell. Mathematical model of network dynamics governing mouse sleep–wake behavior. *Journal of Neurophysiology*, 97(6):3828–3840, 2007. PMID: 17409167.

[18] J. Belair and L. Glass. Universality and self-similarity in the bifurcations of circle maps. *Physica D*, pages 143–154, 1985.

[19] S. Benloucif, M. J. Guico, K. J. Reid, L. F. Wolfe, M. L'Hermite-Balériaux, and P. C. Zee. Stability of melatonin and temperature as circadian phase markers and their relation to sleep times in humans. *Journal of Biological Rhythms*, 20(2):178–188, 2005. PMID: 15834114.

[20] O Benoit, J Foret, G Bouard, B Merle, J Landau, and M.E Marc. Habitual sleep length and patterns of recovery sleep after 24 hour and 36 hour sleep deprivation. *Electroencephalography and Clinical Neurophysiology*, 50(5):477–485, 1980.

[21] R H. Berger, A. L. Miller, R. Seifer, S. R. Cares, and M. K. LeBourgeois. Acute sleep restriction effects on emotion responses in 30- to 36-month-old children. *Journal of Sleep Research*, 21(3):235–246, 2012.

[22] T. Blackwell, S. Redline, S. Ancoli-Israel, J. L. Schneider, S. Surovec, N. L. Johnson, J. A. Cauley, K. L. Stone, and Study of Osteoporotic Fractures Research Group. Comparison of Sleep Parameters from Actigraphy and Polysomnography in Older Women: The SOF Study. *Sleep*, 31(2):283–291, 02 2008.

[23] M S Blumberg, A J Gall, and W D Todd. The development of sleep-wake rhythms and the search for elemental circuits in the infant brain. *Behavioral neuroscience*, 128(3):250–263, 6/2014.

[24] V. Booth and C. G. Diniz Behn. Physiologically-based modeling of sleep/wake regulatory networks. *Math Biosci*, 250:54–68, 2014.

[25] V. Booth, I. Xique, and C. G. Diniz Behn. One-dimensional map for the circadian modulation of sleep in a sleep-wake regulatory network model for human sleep. *SIAM J App Dyn Systems*, 16:1089–1112, 2017.

[26] A. A. Borbély. A two process model of sleep regulation. *Human Neurobiology*, 1(3):195–204, 1982.

[27] A. Borbély and P Achermann. Sleep homeostasis and models of sleep regulation. *Journal of Biological Rhythms*, 14:559–570, 1999.

[28] A. A. Borbély, S. Daan, A. Wirz-Justice, and T. Deboer. The two-process model of sleep regulation: a reappraisal. *Journal of Sleep Research*, 25(2):131–143, 2016.

[29] AA Borbély, P Achermann, MH Kryger, T Roth, and WC Dement. Principles and practice of sleep medicine. *Kryger, MH*, pages 405–417, 2000.

[30] P. Boyland. Bifurcations of circle maps: Arnold tongues, bistability and rotation intervals. *Comm. Math. Phys.*, 106:353–381, 1986.

[31] P.C. Bressloff and J. Stark. Neuronal dynamics based on discontinuous circle maps. *Physics Letters A*, 150(3):187–195, 1990.

[32] E. N. Brown, Y. Choe, T. L. Shanahan, and C. A. Czeisler. A mathematical model of diurnal variations in human plasma melatonin levels. *American Journal of Physiology-Endocrinology and Metabolism*, 272(3):E506–E516, 1997. PMID: 9124558.

[33] M. Calvo, J. I. Montijano, and L. Rández. Algorithm 968: Disode45: A matlab runge-kutta solver for piecewise smooth ivps of filippov type. *ACM Trans. Math. Softw.*, 43(3), December 2016.

[34] M. Carskadon and W. Dement. Normal human sleep: an overview. In M. Kryger, T. Roth, and W. Dement, editors, *Principles and Practice of Sleep Medicine*. Elsevier Saunders, 2011.

[35] C. A. Czeisler and O. M. Buxton. The human circadian timing system and sleep/wake regulation. In M. Kryger, T. Roth, and W. Dement, editors, *Principles and Practice of Sleep Medicine*. Elsevier Saunders, 2011.

[36] C. A. Czeisler, E. Weitzman, M. C. Moore-Ede, J.C. Zimmerman, and R.S. Knauer. Human sleep: its duration and organization depend on its circadian phase. *Science*, 210(4475):1264–1267, 1980.

[37] C. A. Czeisler, J. C. Zimmerman, J. M. Ronda, M. C. Moore-Ede, and E. D. Weitzman. Timing of REM sleep is coupled to the circadian rhythm of body temperature in man. *Sleep*, 2(3):329–346, 1980.

[38] C.A Czeisler, M Dumont, J.F Duffy, J.D Steinberg, G.S Richardson, E.N Brown, R Sánchez, C.D Ríos, and J.M Ronda. Association of sleep-wake habits in older people with changes in output of circadian pacemaker. *The Lancet*, 340(8825):933 – 936, 1992. Originally published as Volume 2, Issue 8825.

[39] S. Daan, D. G. M. Beersma, and A. A. Borbély. Timing of human sleep: Recovery process gated by a circadian pacemaker. *Am. J. Physiol.*, 246:R161–R178, 1984.

[40] P. Dayan and L.F. Abbott. *Theoretical Neuroscience: Computational and Mathematical Modeling of Neural Systems*. The MIT Press, 2001.

[41] G. Deco, V. K. Jirsa, P. A. Robinson, M. Breakspear, and K. Friston. The dynamic brain: from spiking neurons to neural masses and cortical fields. *PLoS Comput Biol*, 4:e1000092, 2008.

[42] G. Derks, P. A. Glendinning, and A. C. Skeldon. Creation of discontinuities in circle maps. *Proceedings of the Royal Society A: Mathematical, Physical and Engineering Sciences*, 477(2251):20200872, 2021.

[43] R. Devaney. *An Introduction to Chaotic Dynamical Systems*. Perseus Books, 1989.

[44] M. di Bernardo, C. J. Budd, and A. R. Champneys. Normal form maps for grazing bifurcations in n-dimensional piecewise-smooth dynamical systems. *Physica D*, 160:222–254, 2001.

[45] M. Di Bernardo, C. J. Budd, A. R. Champneys, and P. Kowalczyk. *Piecewise-smooth dynamical systems: Theory and Applications*. Applied Mathematical Sciences. Springer, January 2008.

[46] C. O. Diekman and A. Bose. Entrainment maps: A new tool for understanding properties of circadian oscillator models. *J Biol Rhythms*, doi:10.1177/0748730416662965, 2016.

[47] C. O. Diekman and A. Bose. Reentrainment of the circadian pacemaker during jet lag: East-west asymmetry and the effects of north-south travel. *Journal of Theoretical Biology*, 437:261–285, 2018.

[48] D. J. Dijk, D. G. M. Beersma, and G. M. Bloem. Sex differences in the sleep eeg of young adults: Visual scoring and spectral analysis. *Sleep*, 12(6):500–507, 1989.

[49] D. J. Dijk, D. G. M. Beersma, and S. Daan. Eeg power density during nap sleep: Reflection of an hourglass measuring the duration of prior wakefulness. *Journal of Biological Rhythms*, 2(3):207–219, 1987. PMID: 2979661.

[50] D. J. Dijk and S. W. Lockley. Invited review: integration of human sleep-wake regulation and circadian rhythmicity. *J Appl Physiol*, 92:852–862, 2002.

[51] D.J. Dijk and C. A. Czeisler. Contribution of the circadian pacemaker and the sleep homeostat to sleep propensity, sleep structure, electroencephalographic slow waves, and sleep spindle activity in humans. *Journal of Neuroscience*, 15(5):3526–3538, 1995.

[52] C. Diniz Behn, A. Ananthasubramaniam, and V. Booth. Contrasting existence and robustness of REM/NREM cycling in physiologically based models of REM sleep regulatory networks. *SIAM J on App Dyn Systems*, 12:279–314, 2013.

[53] C. Diniz Behn and V. Booth. Simulating microinjection experiments in a novel model of the rat sleep-wake regulatory network. *J Neurophysiol*, 103:1937–1953, 2010.

[54] C. Diniz Behn and V. Booth. A fast-slow analysis of the dynamics of REM sleep. *SIAM J on App Dyn Systems*, 11:212–242, 2012.

[55] J. R. Dunmyre, G. A. Mashour, and V. Booth. Coupled flip-flop model for rem sleep regulation in the rat. *PLOS ONE*, 9(4):1–16, 04 2014.

[56] D. Edgar, W. Dement, and C. Fuller. Effect of SCN lesions on sleep in squirrel monkeys: evidence for opponent processes in sleep-wake regulation. *J Neurosci*, 13:1065–1079, 1993.

[57] A.R. Ekirch. *At day's close: a history of nighttime*. W.W. Norton & Company, 2005.

[58] G. B. Ermentrout. Neural networks as spatio-temporal pattern-forming systems. *Rep. Prog. Phys.*, 61:353–430, 1998.

[59] G. B. Ermentrout. *Simulating, analyzing, and animating dynamical systems: a guide to XPPAUT for researchers and students*. Society for Industrial and Applied Mathematics, Philadelphia, 2002.

[60] I. Feinberg and T.C. Floyd. Systematic trends across the night in human sleep cycles. *Psychophysiology*, 16:283–291, 1979.

[61] I Feinberg, J.D March, G Fein, T.C Floyd, J.M Walker, and L Price. Period and amplitude analysis of 0.5–3c/sec activity in nrem sleep of young adults. *Electroencephalography and Clinical Neurophysiology*, 44(2):202–213, 1978.

[62] A. F. Filippov and F. M. Arscott. *Differential equations with discontinuous right-hand sides*. Mathematics and its applications (Soviet series). Kluwer Academic Publishers, 1988.

[63] M. Fleshner, V. Booth, D.B. Forger, and C.G. Diniz Behn. Circadian regulation of sleep-wake behavior in nocturnal rats requires multiple signals from suprachiasmatic nucleus. *Phil. Trans. R. Soc. A*, 369:3855–3883, 2011.

[64] D. B. Forger, M. E. Jewett, and R. E. Kronauer. A simpler model of the human circadian pacemaker. *J Biol Rhythms*, 14:532–537, 1999.

[65] M. G. Frank and H. C. Heller. *The Function(s) of Sleep*, pages 3–34. Springer International Publishing, Cham, 2019.

[66] H. Gaudreau, J. Carrier, and J. Montplaisir. Age-related modifications of NREM sleep EEG: from childhood to middle age. *J Sleep Res*, 10:165–172, 2001.

[67] L. Glass. Cardiac arrhythmias and circle maps-a classical problem. *Chaos*, 1:13–19, 1991.

[68] L. Glass, M. R. Guevara, J. Belair, and A. Shrier. Global bifurcations of a periodically forced biological oscillator. *Phys. Rev. A*, 29:1348–1357, Mar 1984.

[69] L. Glass, M. R. Guevara, A. Shrier, and R. Perez. Bifurcation and chaos in a periodically stimulated cardiac oscillator. *Physica D: Nonlinear Phenomena*, 7:89–101, 1983.

[70] L. Glass and M. C. Mackey. A simple model for phase locking of biological oscillators. *J. Math. Biol.*, 7:339–352, 1979.

[71] R. D. Gleit, C.G. Diniz Behn, and V. Booth. Modeling interindividual differences in spontaneous internal desynchrony patterns. *J. Biol. Rhythms*, 28(5):339–355, 2013.

[72] P. Glendinning. Bifurcations and rotation numbers for maps of the circle associated with flows on the torus and models of cardiac arrhythmias. *Dynamics and Stability of Systems*, 10(4):367–386, 1995.

[73] A. N. Goldstein and M. P. Walker. The role of sleep in emotional brain function. *Annual Review of Clinical Psychology*, 10(1):679–708, 2014. PMID: 24499013.

[74] C. J. Gordon, M. Comas, S. Postnova, C. B. Miller, D. Roy, D. J. Bartlett, and R. R. Grunstein. The effect of consecutive transmeridian flights on alertness, sleep–wake cycles and sleepiness: A case study. *Chronobiology International*, 35(11):1471–1480, 2018. PMID: 29993295.

[75] A. Granados, L. Alseda, and M. Krupa. The period adding and incrementing bifurcations: from rotation theory to applications. *SIAM Review*, 59(2):225–292, 2017.

[76] J. Guckenheimer. Symbolic dynamics and relaxation oscillations. *Physica D: Nonlinear Phenomena*, 1(2):227 – 235, 1980.

[77] J. Guckenheimer and P. Holmes. *Local Bifurcations*, pages 117–165. Springer New York, New York, NY, 1983.

[78] M. R. Guevara and L. Glass. Phase locking, period doubling bifurcations and chaos in a mathematical model of a periodically driven oscillator: A theory for the entrainment of biological oscillators and the generation of cardiac dysrhythmias. *Journal of Mathematical Biology*, 14(1):1–23, Mar 1982.

[79] MR Guevara, L Glass, and A Shrier. Phase locking, period-doubling bifurcations, and irregular dynamics in periodically stimulated cardiac cells. *Science*, 214(4527):1350–1353, 1981.

[80] E. Hartmann. The 90-Minute Sleep-Dream Cycle. *Archives of General Psychiatry*, 18(3):280–286, 03 1968.

[81] JA Hobson, RW McCarley, and PW Wyzinski. Sleep cycle oscillation: reciprocal discharge by two brainstem neuronal groups. *Science*, 189(4196):55–58, 1975.

[82] F. C. Hoppensteadt and J. P. Keener. Phase locking of biological clocks. *J. Math. Biology*, 15:339–349, 1982.

[83] ZL Huang, Y Urade, and O Hayaishi. Prostaglandins and adenosine in the regulation of sleep and wakefulness. *Curr Opin Pharmacol*, 7:33–38, 2007.

[84] I. Iglowstein, O.G. Jenni, L. Molinari, and R.H. Largo. Sleep duration from infancy to adolescence: reference values and generational trends. *Pediatrics*, 111:302–307, 2003.

[85] C. L. Jackson, S. Redline, and K. M. Emmons. Sleep as a potential fundamental contributor to disparities in cardiovascular health. *Annual Review of Public Health*, 36(1):417–440, 2015. PMID: 25785893.

[86] O Jenni and M LeBourgeois. Understanding sleep–wake behavior and sleep disorders in children: the value of a model. *Curr Opin Psychiatry*, 19:282–287, 2006.

[87] O. G. Jenni, P. Achermann, and M. A. Carskadon. Homeostatic sleep regulation in adolescents. *Sleep*, 28(11):1446–1454, 2005.

[88] O. G. Jenni, A. A. Borbély, and P. Achermann. Development of the nocturnal sleep electroencephalogram in human infants. *American Journal of Physiology-Regulatory, Integrative and Comparative Physiology*, 286(3):R528–R538, 2004. PMID: 14630625.

[89] O. G. Jenni and M. A. Carskadon. Sleep behavior and sleep regulation from infancy through adolescence: Normative aspects. *Sleep Medicine Clinics*, 2(3):321–329, 2007. Sleep in Children and Adolescents.

[90] D. Joseph, N. W Chong, M. E Shanks, E. Rosato, N. A Taub, S. A Petersen, M. E Symonds, W. P Whitehouse, and M. Wailoo. Getting rhythm: how do babies do it? *Archives of Disease in Childhood - Fetal and Neonatal Edition*, 100(1):F50–F54, 2015.

[91] D. Kaplan and L. Glass. *Understanding Nonlinear Dynamics*. Springer Science Business Media, 2012.

[92] A. Katok and B. Hasselblatt. *Introduction to the Modern Theory of Dynamical Systems*. Cambridge University Press, New York, NY, 1995.

[93] M. Kawato, K. Fujita, R. Suzuki, and A. T. Winfree. A three-oscillator model of the human circadian system controlling the core temperature rhythm and the sleep-wake cycle. *J. Theor. Biol.*, 98:369–392, 1982.

[94] J. P. Keener. Chaotic behavior in piecewise continuous difference equations. *Trans. Amer. Math. Soc.*, 261:589–604, 1980.

[95] J. P. Keener and L. Glass. Global bifurcations of a periodically forced nonlinear oscillator. *Journal of Mathematical Biology*, 21(2):175–190, Dec 1984.

[96] J. P. Keener, F. C. Hoppensteadt, and J. Rinzel. Integrate-and-fire models of nerve membrane response to oscillatory input. *SIAM J. Appl. Math.*, 41:503–517, 1981.

[97] K. L. Knutson, K. Spiegel, P. Penev, and E. Van Cauter. The metabolic consequences of sleep deprivation. *Sleep Medicine Reviews*, 11(3):163–178, 2007.

[98] R. E. Kronauer, C. A. Czeisler, S. F. Pilato, M. C. Moore-Ede, and E. D. Weitzman. Mathematical model of the human circadian system with two interacting oscillators. *Am. J. Physiol.*, 242:R3–R17, 1982.

[99] R. E. Kronauer, D. B. Forger, and M. E. Jewett. Errata: Quantifying human circadian pacemaker response to brief, extended, and repeated light stimuli over the photopic range. *J Biol Rhythms*, 15:184–186, 2000.

[100] R. Kumar, A. Bose, and B. N. Mallick. A mathematical model towards understanding the mechanism of neuronal regulation of wake-nrems-rems states. *PLoS One*, 7(8):e42059, 2012.

[101] MK LeBourgeois, T Rusterholtz, OG Jenni, MA Carskadon, and P Achermann. Do the dynamics of sleep homeostasis (process s) change across early childhood? In *SLEEP*, volume 35, pages A21–A21, 2012.

[102] S. Lopp, W. Navidi, P. Achermann, M. LeBourgeois, and C. Diniz Behn. Developmental changes in ultradian sleep cycles across early childhood: Preliminary insights. *Journal of Biological Rhythms*, 32(1):64–74, 2017. PMID: 28088873.

[103] J. Lu, D. Sherman, M. Devor, and C. B. Saper. A putative flip–flop switch for control of rem sleep. *Nature*, 441:589–594, 2006.

[104] M. M. Mallis, S. Mejdal, T. T Nguyen, and D. F. Dinges. Summary of the key features of seven biomathematical models of human fatigue and performance. *Aviation, space, and environmental medicine*, 75 3 Suppl:A4–14, 2004.

[105] A. Martinez-Nicolas, E. Ortiz-Tudela, J. Antonio Madrid, and M. Angeles Rol. Crosstalk between environmental light and internal time in humans. *Chronobiology International*, 28(7):617–629, 2011.

[106] R. W. McCarley and J. A. Hobson. Neuronal excitability modulation over the sleep cycle: a structural and mathematical model. *Science*, 189:58–60, 1975.

[107] R. W. McCarley and S. G. Massaquoi. A limit-cycle mathematical-model of the REM-sleep oscillator system. *Am J Physiol*, 251:R1011–R1029, 1986.

[108] D. McGinty, H. Gong, N. Suntsova, N. Alam, M. Methippara, R. Guzman-Marin, and R. Szymusiak. Sleep-promoting functions of the hypothalamic median preoptic nucleus: inhibition of arousal systems. *Arch It Biol*, 142:501–509, 2004.

[109] J. H. Meijer, S. Michel, H. T. VanderLeest, and J. H. T. Rohling. Daily and seasonal adaptation of the circadian clock requires plasticity of the scn neuronal network. *European Journal of Neuroscience*, 32(12):2143–2151.

[110] J. H. Meijer, K. Watanabe, J. Schaap, H. Albus, and L. Détári. Light responsiveness of the suprachiasmatic nucleus: Long-term multiunit and single-unit recordings in freely moving rats. *Journal of Neuroscience*, 18(21):9078–9087, 1998.

[111] L. J. Meltzer, L. S. Hiruma, K. Avis, H. Montgomery-Downs, and J. Valentin. Comparison of a Commercial Accelerometer with Polysomnography and Actigraphy in Children and Adolescents. *Sleep*, 38(8):1323–1330, 08 2015.

[112] B. Miner and M. H. Kryger. Sleep in the aging population. *Sleep Medicine Clinics*, 12(1):31–38, 2017. Social and Economic Dimensions of Sleep Disorders.

[113] R. E. Mistlberger. Circadian regulation of sleep in mammals: role of the suprachiasmatic nucleus. *Brain Res Rev*, 49:429–454, 2005.

[114] R. Y. Moore. Circadian rhythms: basic neurobiology and clinical applications. *Ann Rev Med*, 48:253–266, 1997.

[115] M. C. Moore-Ede and C. A. Czeisler, editors. *Mathematical models of the circadian sleep-wake cycle*. Raven Press, New York, NY, 1984.

[116] L. P. Morin. Neuroanatomy of the extended circadian rhythm system. *Experimental Neurology*, 243:4–20, 2013. Circadian rhythms and sleep disorders.

[117] M. Mrugala, P. Zlomanczuk, A. Jagota, and W. J. Schwartz. Rhythmic multiunit neural activity in slices of hamster suprachiasmatic nucleus reflect prior photoperiod. *American Journal of Physiology-Regulatory, Integrative and Comparative Physiology*, 278(4):R987–R994, 2000.

[118] M. Nakao, H. Sakai, and M. Yamamoto. An interpretation of the internal desynchronizations based on dynamics of the two-process model. *Meth Inform Med*, 36:282–285, 1997.

[119] M. Nakao and M. Yamamoto. Bifurcation properties of the two process model. *Psychiatry Clin Neurosci.*, 52(2):131–133, 1998.

[120] A. B. Nordmark. Non-periodic motion caused by grazing incidence in an impact oscillator. *J Sound Vibration*, 145:279–297, 1991.

[121] M. Ohayon, M. Carskadon, C. Guilleminault, and M. Vitiello. Meta-analysis of quantiative sleep parameters from childhood to old age in healthy individuals: developing normative sleep values across the human lifespan. *SLEEP*, 27:1255–1273, 2004.

[122] M. Patel. A simplified model of mutually inhibitory sleep-active and wake-active neuronal populations employing a noise-based switching mechanism. *Journal of Theoretical Biology*, 394:127 – 136, 2016.

[123] A. J. K. Phillips, C. A. Czeisler, and E. B. Klerman. Revisiting spontaneous internal desynchrony using a quantitative model of sleep physiology. *J Biol Rhythms*, 26:441–453, 2011.

[124] A. J. K. Phillips, B. D. Fulcher, P. A. Robinson, and E. B Klerman. Mammalian rest/activity patterns explained by physiologically based modeling. *PLoS Comput Biol*, 9(9), 2013.

[125] A. J. K. Phillips and P. A. Robinson. A quantitative model of sleep-wake dyamics based on the physiology of the brainstem ascending arousal system. *Journal of Biological Rhythms*, 22(2):167–179, 2007.

[126] A. J. K. Phillips and P. A. Robinson. Sleep deprivation in a quantitative physiologically based model of the ascending arousal system. *J Theor Biol*, 255:413–423, 2008.

[127] A. J. K. Phillips, P. A. Robinson, D. J. Kedziora, and R. G. Abeysuriya. Mammalian sleep dynamics: How diverse features arise from a common physiological framework. *PLOS Computational Biology*, 6(6):1–9, 06 2010.

[128] S. H. Piltz, C. Athanasouli, C. G. Diniz Behn, and V. Booth. Mapping recovery from sleep deprivation. *Communications in Nonlinear Science and Numerical Simulation*, 96:105686, 2021.

[129] S. H. Piltz, C. G. Diniz Behn, and V. Booth. Habitual sleep duration affects recovery from acute sleep deprivation: A modeling study. *Journal of Theoretical Biology*, 504:110401, 2020.

[130] S. Postnova, A. Layden, P. A. Robinson, A. J.K. Phillips, and R. G. Abeysuriya. Exploring sleepiness and entrainment on permanent shift schedules in a physiologically based model. *Journal of Biological Rhythms*, 27(1):91–102, 2012. PMID: 22306977.

[131] S. Postnova, S. W. Lockley, and P. A. Robinson. Prediction of cognitive performance and subjective sleepiness using a model of arousal dynamics. *Journal of Biological Rhythms*, 33(2):203–218, 2018. PMID: 29671707.

[132] S. R. Pring and C. J. Budd. The dynamics of a simplified pinball machine. *IMA Journal of Applied Mathematics*, 76(1):67–84, Feb 2011.

[133] A. Rechtschaffen, B. M. Bergmann, M. A. Gilliland, and K. Bauer. Effects of Method, Duration, and Sleep Stage on Rebounds from Sleep Deprivation in the Rat. *Sleep*, 22(1):11–31, 01 1999.

[134] M. J. Rempe, J. Best, and D. Terman. A mathematical model of the sleep/wake cycle. *J Math. Biol.*, 60(5):615–644, 2010.

[135] F. Rhodes and C. L. Thompson. Rotation numbers for monotone functions on the circle. *Journal of the London Mathematical Society*, s2-34(2):360–368, 1986.

[136] T. Rusterholz, R. Durr, and P. Achermann. Inter-individual differences in the dynamics of sleep homeostasis. *SLEEP*, 33:491–498, 2010.

[137] S. Sahar and P. Sassone-Corsi. Metabolism and cancer: the circadian clock connection. *Nat Rev Cancer*, 9:886–896, 2009.

[138] P Salzarulo and I Fagioli. Post-natal development of sleep organization in man: speculations on the emergence of the 's process'. *Neurophysiologie Clinique/Clinical Neurophysiology*, 22(2):107–115, 1992.

[139] C B Saper, T C Chou, and T E Scammell. The sleep switch: hypothalamic control of sleep and wakefulness. *Trends in Neurosciences*, 24(12):726 – 731, 2001.

[140] C. B. Saper, T. E. Scammell, and J. Lu. Hypothalamic regulation of sleep and circadian rhythms. *Nature*, 437:1257–1263, 2005.

[141] T. E. Scammell, E. Arrigoni, and J. O. Lipton. Neural circuitry of wakefulness and sleep. *Neuron*, 93(4):747–765, 2017.

[142] F. A. J. L. Scheer, M. F. Hilton, C. S. Mantzoros, and S. A. Shea. Adverse metabolic and cardiovascular consequences of circadian misalignment. *PNAS*, 106:4453–4458, 2009.

[143] F. A.J.L. Scheer and C. A. Czeisler. Melatonin, sleep, and circadian rhythms. *Sleep Medicine Reviews*, 9(1):5–9, 2005.

[144] K. Serkh and D. B. Forger. Optimal schedules of light exposure for rapidly correcting circadian misalignment. *PLoS Comput Biol*, 10:e1003523, 2014.

[145] J. Siegel. REM sleep. In M. Kryger, T. Roth, and W. Dement, editors, *Principles and Practice of Sleep Medicine*. Elsevier Saunders, 2011.

[146] S. L. Simon, C. Diniz Behn, M. Cree-Green, J. L. Kaar, L. Pyle, S. M.M. Hawkins, H. Rahat, Y. Garcia-Reyes, K. P. Wright, and K. J. Nadeau. Too late and not enough: School year sleep duration, timing, and circadian misalignment are associated with reduced insulin sensitivity in adolescents with overweight/obesity. *The Journal of Pediatrics*, 205:257–264.e1, 2019.

[147] A. Skeldon, D. J. Dijk, and G. Derks. Mathematical models for sleep-wake dynamics: Comparison of the two-process model and a mutual inhibition neuronal model. *PLoS One*, 9:e103877, 2014.

[148] A. C. Skeldon, A. J. K. Phillips, and D. J. Dijk. The effects of self-selected light-dark cycles and social constraints on human sleep and circadian timing: a modeling approach. *Scientific Reports*, 7:45158 EP –, 03 2017.

[149] E. R. Stothard, A. W. McHill, C. M. Depner, B. R. Birks, T. M. Moehlman, H. K. Ritchie, J. R. Guzzetti, E. D. Chinoy, M. K. LeBourgeois, J. Axelsson, and K. P. Wright. Circadian entrainment to the natural light-dark cycle across seasons and the weekend. *Current Biology*, 27(4):508 – 513, 2017.

[150] S. Strogatz, R. E. Kronauer, and C. A. Czeisler. Circadian pacemaker interferes with sleep onset and specific times each day: role in insomnia. *Am J Physiol - Reg, Int, and Comp Physiol*, 253:R172–R178, 1987.

[151] S.H. Strogatz. Human sleep and circadian rhythms: A simple model based on two coupled oscillators. *J. Math. Biology*, 25:327–347, 1987.

[152] Y. Tamakawa, A. Karashima, Y. Koyama, N. Katayama, and M. Nakao. A quartet neural system model orchestrating sleep and wakefulness mechanisms. *Journal of Neurophysiology*, epub:2055–2069, 2006.

[153] For the Osteoporotic Fractures in Men (MrOS) Study Group. Relationships Between Sleep Stages and Changes in Cognitive Function in Older Men: The MrOS Sleep Study. *Sleep*, 38(3):411–421, 03 2015.

[154] I. Tobler. Is sleep fundamentally different between mammalian species? *Behavioral Brain Research*, 69:35–41, 1995.

[155] I. Tobler, P. Franken, L. Trachsel, and A. Borbély. Models of sleep regulation in mammals. *Journal of Sleep Research*, 1:125–127, 1992.

[156] H. P. A. van Dongen, K. M. Vitellaro, and D. F. Dinges. Individual Differences in Adult Human Sleep and Wakefulness: Leitmotif for a Research Agenda. *Sleep*, 28(4):479–498, 04 2005.

[157] H. T. VanderLeest, T. Houben, S. Michel, T. Deboer, H. Albus, M. J. Vansteensel, G. D. Block, and J. H. Meijer. Seasonal encoding by the circadian pacemaker of the scn. *Current Biology*, 17(5):468 – 473, 2007.

[158] G. W. Vogel. A Review of REM Sleep Deprivation. *Archives of General Psychiatry*, 32(6):749–761, 06 1975.

[159] A. Voultsios, D. J. Kennaway, and D. Dawson. Salivary melatonin as a circadian phase marker: Validation and comparison to plasma melatonin. *Journal of Biological Rhythms*, 12(5):457–466, 1997. PMID: 9376644.

[160] O. J. Walch, A. Cochran, and D. B. Forger. A global quantification of "normal" sleep schedules using smartphone data. *Science Advances*, 2(5):e1501705, 2016.

[161] T. A. Wehr. In short photoperiods, human sleep is biphasic. *J Sleep Res*, 1:103–107, 1992.

[162] D K Welsh, D E Logothetis, M Meister, and S M Reppert. Individual neurons dissociated from rat suprachiasmatic nucleus express independently phased circadian firing rhythms. *Neuron*, 14(4):697–706, 1995.

[163] H. R. Wilson and J. D. Cowan. Excitatory and inhibitory interactions in localized populations of model neurons. *Biophys J*, 12:1–24, 1972.

[164] A. T. Winfree. Impact of a circadian clock on the timing of human sleep. *Am. J. Physiol.*, 245:R497–R504, 1983.

[165] A. R. Wolfson. Sleeping patterns of children and adolescents: Developmental trends, disruptions, and adaptations. *Child and Adolescent Psychiatric Clinics of North America*, 5(3):549–568, 1996. Sleep Disorders.

[166] Y. Zhang, A. Bose, and F. Nadim. The influence of the a-current on the dynamics of an oscillator-follower inhibitory network. *SIAM J Applied Dynamical Systems*, 8:1564–1590, 2009.

[167] T. Åkerstedt and M. Gillberg. The Circadian Variation of Experimentally Displaced Sleep. *Sleep*, 4(2):159–169, 09 1981.

[168] P. Östborn, G. Ohlén, and B. Wohlfart. Simulated sinoatrial exit blocks explained by circle map analysis. *Journal of Theoretical Biology*, 211(3):219–227, 2001.

APPENDICES

APPENDIX A

The Structure of the Map as k and α_{SCN} Vary

The first return circle maps we have presented are characterized by at least one discontinuity. The discontinuity associated with the bifurcations leading to loss of stability of (p, q) periodic solutions is the one caused by tangencies on the upper saddle-node curve of the fast-slow surface. In this appendix we explain that in the regime of rotation number $\rho = \frac{q}{p}$, the p^{th} return map has p discontinuities associated with the appropriate discontinuity of the first return map. Let $\Pi : [0, 1] \to [0, 1]$ represent the first return map that demonstrates a discontinuity because of a tangency on a saddle-node curve. Then $\Pi([0, 1]) = [0, 1] \setminus I$, where I is some interval and the backslash, $\setminus$, indicates that I is excluded from the interval $[0, 1]$. According to our results, the discontinuity occurs close to the peak of the circadian oscillator for $k = 1$ and starts shifting towards later phases as k decreases. The interval I that is excluded from the range of the map is associated with the rising phase of the circadian oscillator. As mentioned in [25], during the rising phase of c, and hence f_{SCN}, the dynamics close to the upper-saddle node curve strongly promote the consolidation of wake. This leads to a horizontal gap in the map, where we force sleep onset by following the eigenvector associated with the unstable manifold at those saddle-node points. This is extensively analyzed in [25]. This horizontal gap overlaps in large part with the interval I.

The discontinuity in terms of our discrete circle map can be described as follows: Assume that the discontinuity of the map occurs between the points $(x_1, \Pi(x_1))$ and $(y_1, \Pi(y_1))$. Then $\forall\ \delta > 0$, $\exists\ \epsilon > 0$ such that for $|x - y| < \delta$ for x, y around the discontinuity, then $|\Pi(x) - \Pi(y)| > \epsilon$. In the regime close to the occurrence of a bifurcation, there is one stable periodic orbit of period p and the map is increasing on either side of the discontinuity.

If the first return map has a discontinuity between x_1 and y_1, with $x_1 < y_1$, then by a "backwards" cobwebbing on the map we can find x_2, y_2, so that $x_1 = \Pi(x_2)$ and $y_1 = \Pi(y_2)$. Since the map is continuous everywhere else and invertible, x_2 and y_2 are sufficiently close. We can now repeat the same process, and find x_3 and y_3 sufficiently close, so that $x_2 = \Pi(x_3)$ and $y_2 = \Pi(y_3)$. Finally, when we do this $p - 1$ times the first return map contains two sequences $\{x_2, ..., x_p\}$ and $\{y_2, ..., y_p\}$ that satisfy: $x_{j-1} = \Pi(x_j)$ and $y_{j-1} = \Pi(y_j)$ for $j = 2, .., p$, respectively. Therefore, the p^{th} iteration of the map, Π^p, has $p - 1$ discontinuities, each across x_j, y_j, for $j = 2, .., p$. The idea is that the map provides approximate initial conditions x_j, y_j on the same two trajectories that will lead to the discontinuity x_1, y_1 after j iterations, for $j = 2, .., p$. So, we are approximately looking at the same two trajectories when they crossed the section at a "past" time that will eventually lead them to crossing the section again at phases x_1 and y_1 after $j - 1$ more times.

Additionally, Π^p has another discontinuity across x_1 and y_1 leading to p total discontinuities. The discontinuity of the first return map persists in the p^{th} iteration, since it takes at least q circadian days for the trajectories across the discontinuity to entrain, i.e to converge to the stable p^{th}-order cycle of the map. In other words, if one sleeps at a circadian phase corresponding to the infinite slope branch of the map, it will take a few days to converge to the stable sleep pattern. Hence, Π^p is divided into p branches bordered by two pairs from elements of the sequences $\{x_1, ..., x_p\}$ and $\{y_1, ..., y_p\}$. Each branch is increasing and maps a subinterval of $[0, 1]$ to an other

interval in the range of Π^p.

Since we compute the maps numerically, it is important to note that the values we obtain from this process might not agree exactly with the computed data points of the map. However, in any case we can predict where the discontinuities in the p^{th} return map will occur within some error and how many should exist coming from the discontinuity of the first return map.

Recall that discontinuities due to a tangency at the saddle-node curves are characterized by an infinite slope in the left branch of the map curve and a finite slope in the right branch. Hence, in the appropriate regime of the $k - \alpha_{SCN}$ parameter space and with k decreasing, when we first enter the $\left\{\rho = \frac{q}{p}\right\}$-regime, the branches with infinite slope intersect the diagonal $\Phi_{n+p} = \Phi_n$ at a saddle-node bifurcation. As k further decreases, the finite slope part of each branch approaches the diagonal which leads to the loss of stability of the (p, q) periodic solution due to a border collision or a saddle-node bifurcation. For higher values of k we observe border collisions, but for lower values the finite parts start curving downwards introducing more saddle-node bifurcations.

When k is sufficiently small, the map becomes continuous, so only saddle-node bifurcations occur. The homeostatic sleep drive h is fast enough now that it can counteract the wake-promoting effect of f_{SCN}. In this transition the vertical gap shrinks and interestingly the length of the horizontal gap also reduces accordingly. For values of k and α_{SCN} that the map is continuous, we see that the bifurcation diagram of the rotation number, ρ, becomes more dense and continuous as well.

APPENDIX B

Computation of the Bifurcation Diagram of the Rotation Number ρ

The rotation number $\rho = \frac{q}{p}$ describes the number of circadian days over the number of sleep episodes. To compute the rotation number numerically, we have created an algorithm that detects the repeating pattern of sleep episodes from the model trajectory.

The algorithm works as follows: For each value of k we simulate the model for 100 days to ensure that it has converged to its stable solution. Simultaneously, we keep track of the sleep onsets and their corresponding preceding circadian minima, i.e., the local minima of the variable c, using a detection of the event $f_W = 4$ during the decrease of the variable f_W. This allows us to compute the circadian phase of each sleep onset in the simulation.

Starting at the last sleep onset phase recorded, we check the preceding sleep onset phases to detect the previous occurrence of the same phase. Since, all of our results are obtained numerically, we allow for an error of 0.0003 for two phases to be considered "equal". If the length of the subsequence that involves the two "equal" phases and all intermediate sleep onset phases is $p + 1$, then the number of sleep episodes in the pattern is defined to be p (this avoids double counting the first/last phase).

To determine the number of circadian days, q, we count the distinct number of circadian minima that correspond to the sleep onset phases of the pattern.

For some values of k, this algorithm did not detect a stable repeating pattern. In that case, we computed an average ρ as the total number of days divided by the total number of sleep cycles in a simulation lasting 120 days.

APPENDIX C

Circadian Hard Switch (CHS) Model

In the CHS model, model dynamics are smooth in the four subregions ($\Sigma^+ \cup \Gamma^+$, $\Sigma^+ \cup \Gamma^-$, $\Sigma^- \cup \Gamma^+$, $\Sigma^- \cup \Gamma^-$) and dynamics on the boundaries Σ and Γ are defined by Filippov's convex method. Specifically, for $\mathbf{X} = \{f_W, f_S, f_{SCN}, h, c, \theta\}$ we represent the model system as follows:

$$\frac{d\mathbf{X}}{dt} = \begin{cases} F_{11}(\mathbf{X}) & \mathbf{X} \in \Sigma^+ \cap \Gamma^+ \\ \bar{co}\{F_{11}, F_{12}\} & \mathbf{X} \in \Gamma^+ \cap \Sigma \\ F_{12}(\mathbf{X}) & \mathbf{X} \in \Sigma^- \cap \Gamma^+ \\ \bar{co}\{F_{12}, F_{21}\} & \mathbf{X} \in \Sigma^- \cap \Gamma \\ F_{21}(\mathbf{X}) & \mathbf{X} \in \Sigma^- \cap \Gamma^- \\ \bar{co}\{F_{21}, F_{22}\} & \mathbf{X} \in \Gamma^- \cap \Sigma \\ F_{22}(\mathbf{X}) & \mathbf{X} \in \Sigma^+ \cap \Gamma^- \\ \bar{co}\{F_{22}, F_{11}\} & \mathbf{X} \in \Sigma^+ \cap \Gamma \end{cases}$$

where $\bar{co}\{F_{ij}, F_{kl}\} = \{F_{ij,kl} = \alpha F_{ij} + (1-\alpha)F_{kl}, \alpha \in [0,1]\}$ is a convex combination of the flows on either side of a switching boundary. The vector fields $F_{ij}(\mathbf{X})$ in the different subregions are defined as follows:

- The following differential equations regarding the variables f_W, f_S, c, θ are true for all $F_{ij}(\mathbf{X})$ in their corresponding subregions:

$$\frac{df_W}{dt} = \frac{W_{max} \cdot 0.5 \cdot \left(1 + \tanh\left(\frac{g_{scnw} f_{SCN} - g_{sw} f_S - \beta_W}{\alpha_W}\right)\right) - f_W}{\tau_W} \tag{C.1}$$

$$\frac{df_S}{dt} = \frac{S_{max} \cdot 0.5 \cdot \left(1 + \tanh\left(\frac{-g_{scns} f_{SCN} - g_{ws} f_W - (k_2 h + k_1)}{\alpha_S}\right)\right) - f_S}{\tau_S} \tag{C.2}$$

$$\frac{dc}{dt} = -\omega \sin\theta \tag{C.3}$$

$$\frac{d\theta}{dt} = \omega \tag{C.4}$$

- In $F_{11}(\mathbf{X})$ and $F_{22}(\mathbf{X})$ f_{SCN}, where $c > 0$, the differential equation of f_{SCN} is:

$$\frac{df_{SCN}}{dt} = \frac{SCN_{max} \cdot 0.5 \cdot \left(1 + \tanh\left(\frac{1}{0.7}\right)\right) - f_{SCN}}{\tau_{SCN}} \tag{C.5}$$

$$\frac{dh}{dt} = \frac{h_{max} - h}{\tau_{hw}} \tag{C.6}$$

On the other hand, in $F_{12}(\mathbf{X})$ and $F_{21}(\mathbf{X})$ the differential equation for f_{SCN} is:

$$\frac{df_{SCN}}{dt} = \frac{SCN_{max} \cdot 0.5 \cdot \left(1 - \tanh\left(\frac{1}{0.7}\right)\right) - f_{SCN}}{\tau_{SCN}} \tag{C.7}$$

- Similarly, in $F_{11}(\mathbf{X})$ and $F_{12}(\mathbf{X})$, h is increasing and its differential equation is:

$$\frac{dh}{dt} = \frac{h_{max} - h}{\tau_{hw}} \tag{C.8}$$

In $F_{21}(\mathbf{X})$ and $F_{22}(\mathbf{X})$, h is decreasing and its differential equation is:

$$\frac{dh}{dt} = \frac{h_{min} - h}{\tau_{hs}} \tag{C.9}$$

Ruling out sliding motions

To check whether the model flow does not permit the occurrence of sliding motion on the switching boundaries Σ or Γ, we need to determine whether trajectories will always cross Σ or Γ transversally. To this end, let $g(\mathbf{X}) = f_W - \theta_W = 0$ define the boundary Γ and $v(\mathbf{X}) = c - \beta_{SCN} = 0$ define the boundary Σ. Then, $\nabla g =< 1, 0, 0, 0, 0, 0 >$ and $\nabla v =< 0, 0, 0, 0, 1, 0 >$. For each boundary subregion, the conditions verifying that the flow directions on either side of a switching boundary Σ and Γ are in the same direction are as follows:

- On $\Sigma^+ \cap \Gamma$:

$$\Big(\nabla g(\mathbf{X})^T \cdot F_{22}\Big)\Big(\nabla g(\mathbf{X})^T \cdot F_{11}\Big) = \left(\frac{W_{max} \cdot 0.5 \cdot \left(1 + \tanh\left(\frac{g_{scnw} f_{SCN} - g_{sw} f_S - \beta_W}{\alpha_W}\right)\right) - f_W}{\tau_W}\right)^2 \geq 0.$$

- Similarly, on $\Sigma^- \cap \Gamma$:

$$\Big(\nabla g(\mathbf{X})^T \cdot F_{12}\Big)\Big(\nabla g(\mathbf{X})^T \cdot F_{21}\Big) = \left(\frac{W_{max} \cdot 0.5 \cdot \left(1 + \tanh\left(\frac{g_{scnw} f_{SCN} - g_{sw} f_S - \beta_W}{\alpha_W}\right)\right) - f_W}{\tau_W}\right)^2 \geq 0$$

- On $\Sigma \cap \Gamma^+$:
  $\Big(\nabla v(\mathbf{X})^T \cdot F_1\Big)\Big(\nabla v(\mathbf{X})^T \cdot F_2\Big) = (-\omega \sin(\theta))^2 \geq 0.$

- Similarly, on $\Sigma \cap \Gamma^-$:
  $\Big(\nabla v(\mathbf{X})^T \cdot F_3\Big)\Big(\nabla v(\mathbf{X})^T \cdot F_4\Big) = (-\omega \sin(\theta))^2 \geq 0.$

All four of these conditions are satisfied indicating that the boundaries cannot be attracting (or repelling) from both sides. This is sufficient to ensure that trajectories transversely cross each of the switching manifolds Σ and Γ [45]. Thus, the possibility of sliding on Σ and Γ is eliminated, and the representation of the flow on these boundaries as a convex combination of the flow on either side of the boundary is well-defined with an arbitrary choice of α.

APPENDIX D

Stable Solutions for $k = 0.434$ and $k = 0.317$ With $\alpha_{SCN} = 0.7$

The model trajectories in Figure D.1 graze the upper saddle-node curve of the Z-surface. The occurrence of these tangent intersections (or grazing bifurcations of the flow) leads to loss of stability of the $\rho = \frac{2}{3}$ (Figure D.1A) and $\rho = \frac{1}{2}$ (Figure D.1B) solutions. This is predicted in the corresponding third and second return maps (Figure 3.2D, F), respectively, where border collision bifurcations of the stable fixed points are observed.

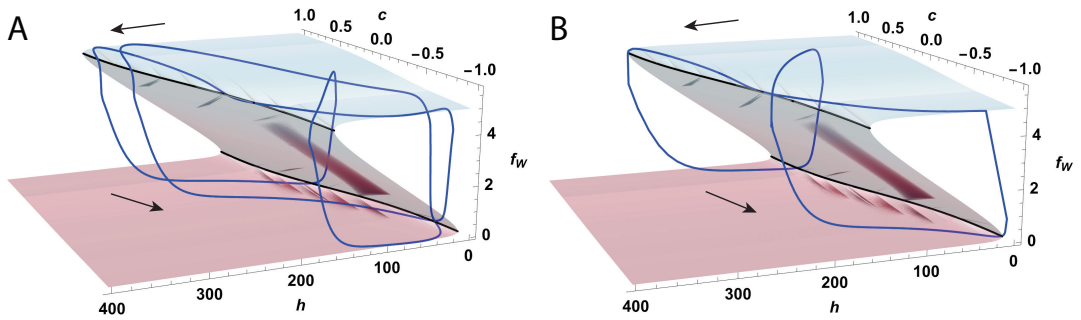

Figure D.1: The stable periodic orbits for $k = 0.434$ and $k = 0.317$ plotted in relation to the $Z-$shaped surface in the $c - h - f_W$ space for the default value of $\alpha_{SCN} = 0.7$. A. The $\rho = \frac{2}{3}$ solution loses stability when the periodic orbit makes a tangent intersection with the upper saddle-node curve of the Z-shaped curve. This periodic orbit corresponds to the three stable fixed points of the third return map in Figure 3.2D in which a border collision is observed. B. The $\rho = \frac{1}{2}$ solution loses stability when the periodic orbit makes a tangent intersection with the upper saddle-node curve of the Z-shaped curve. This periodic orbit corresponds to the two stable fixed points of the second return map in Figure 3.2F in which a border collision is observed.

APPENDIX E

Higher Order Maps of the Three-state Model

E.1 Maps showing the loss of sleep episodes with 6 REM bouts for χ in the $\rho < 1$ regime

Here, we show the deformation of the first return map illustrating how sleep episodes with 6 REM bouts cease to exist for χ in the $\rho = 1$ regime. For $0.721 < \chi < 0.7235$, the six-REM-branch still participates in stable solutions corresponding to sleep patterns associated with $\rho < 1$. At $\chi = 0.7215$ (Figure E.1A), it exists over a very narrow interval of sleep onset phases but is visited in the stable solution, represented by a higher order cycle on the first return map. The neighboring five-REM-branches on either side of it approach each other and finally merge into a single five-REM-branch as shown for $\chi = 0.7165$ (Figure E.1B). Thus, the basin of attraction of the $\rho_{REM} = 6$ solution, and hence the corresponding map branch, is annihilated as χ decreases. This is a consequence of the faster growth and decay rates of the homeostatic sleep drive that affects the total sleep duration and hence the potential total number of REM bouts generated during a sleep cycle.

The first return map continues to show an unstable fixed point on the five-REM-branch for χ values where stable solutions have $\rho < 1$ (and thus the stable fixed points

appear on higher order return maps). This unstable fixed point disappears in a border collision at $\chi = 0.69$.

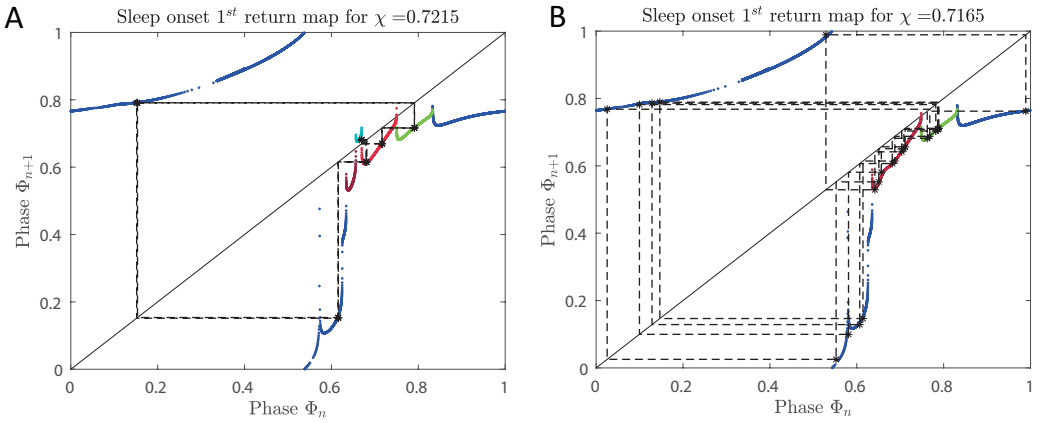

Figure E.1: Loss of the six REM branch in the first return map. A. The first return map for $\chi = 0.7215$ with cobwebbing of the stable solution. The pattern of the stable solution with $\rho < 1$ exhibits a sleep episode involving 6 REM bouts. B. The first return map for $\chi = 0.7165$ with cobwebbing of the stable solution. The solution does not involve sleep episodes with 6 REM bouts and that is predicted by the structure of the map as the 6 REM map branch has vanished.

E.2 Maps showing solutions near the end of the $\rho = \frac{1}{2}$ regime as χ decreases

As χ decreases to the end of the $\rho = \frac{1}{2}$ regime, a period doubling cascade from the $\{2_{(2,3)}, 2_{(2,2)}\}^{\infty}$ pattern occurs for $\chi \in [0.43, 0.431]$ (Figure E.2A). As an example, the stable solution for $\chi = 0.43$ appears on the second return map as a higher order cycle alternating between the $(2, 3)$ (blue) and $(2, 2)$ (green) map branches. As χ decreases further to $\chi = 0.41$, a border collision at the unstable fixed points on each of the $(2, 2)$ (green) map branches designates the loss of stability of the $\rho = \frac{1}{2}$ solution (Figure E.2B).

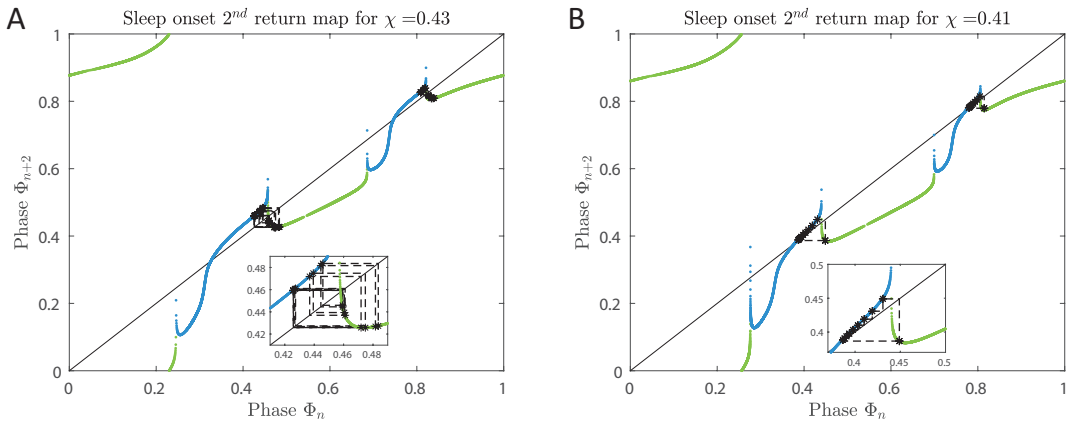

Figure E.2: Second return maps towards the end of the $\rho = \frac{1}{2}$ solution as χ is decreased. A. Second return map for $\chi = 0.43$. B. Second return map for $\chi = 0.41$. Dashed lines show cobwebbing orbit of the stable solution.